THESIS FOR THE DEGREE OF DOCTOR OF PHILOSOPHY

Improved Fuel Conversion in Chemical Looping Combustion using Novel Volatiles Distributors and Effective Manganese-based Oxygen Carriers

XIAOYUN LI

Department of Space, Earth and Environment

CHALMERS UNIVERSITY OF TECHNOLOGY

Gothenburg, Sweden 2024

Improved Fuel Conversion in Chemical Looping Combustion using Novel Volatiles Distributors and Effective Manganese-based Oxygen Carriers

ISBN: 978-91-8103-046-4

Doktorsavhandling vid Chalmers Tekniska Högskola

Series number: 5504

ISSN 0346-718X

Department of Space, Earth and Environment

Division of Energy Technology

Chalmers University of Technology

SE-412 96 Gothenburg

Sweden

Telephone +46 (0)31-772 1000

Cover:

Chemical-looping combustion of renewable biomass for negative CO_2 emission.

Printed by Chalmers Digitaltryck

Gothenburg, Sweden 2024

Improved Fuel Conversion in Chemical Looping Combustion using Novel Volatiles Distributors and Effective Manganese-based Oxygen Carriers

XIAOYUN LI
Division of Energy Technology
Department of Space, Earth and Environment
Chalmers University of Technology

Abstract

Chemical looping combustion (CLC) is a promising carbon capture technology, as CO_2 generated during combustion is inherently obtained in a concentrated form. As the technology moves from pilot-scale to larger-scale operations, factors such as fuel conversion and the development of robust and economically feasible oxygen carriers become increasingly critical. In this thesis, two ways to improve the fuel conversion in the fuel reactor are studied: i) use of a volatile distributor to achieve improved gas-solids contact and ii) use of effective and cheap oxygen carrier materials.

Poor contact between volatiles from solid fuels such as biomass, and oxygen carriers is one reason for insufficient gas conversion in the fuel reactor of CLC systems based on interconnected fluidized beds. Hence, the concept of a volatiles distributor (VD) is proposed for achieving a uniform cross-sectional distribution of volatiles, providing better gas-solids contact and improving the gas conversion in the fuel reactor. In this work, it is clearly demonstrated that the use of the VD results in a more uniform cross-sectional distribution of volatiles under different fluidization regimes. Adjusted designs of the VD were found to improve the uniformity of the horizontal distribution of the simulated volatiles. CFD simulations additionally reveal the improved gas-solids mixing, highlighting the potential of the VD for addressing incomplete conversion of high-volatile fuels in fluidized bed systems. The effectiveness and design flexibility of the VD, together with the most suitable drag model identified in the CFD simulations, are instructive for the large-scale application of the VD.

In chemical looping with oxygen uncoupling (CLOU), the conversion of volatiles and char in the fuel reactor can be notably enhanced compared to regular CLC. This justifies studies of CLOU oxygen carriers with sufficient reactivity, mechanical stability, and reasonable production costs. This thesis covers the investigations of four natural manganese ores and one manufactured calcium manganite as oxygen carriers in a 300 W circulating fluidized-bed system together with detailed characterizations of the fresh and spent oxygen carrier samples. CLC operations with non-calcined manganese ores proceed as smoothly as with calcined ones, indicating that an energy-intensive pre-calcination step for manganese-based oxygen carriers in large-scale applications is not necessary. The content of Fe in manganese ores plays a crucial role in their O_2 release. A sufficiently high content of Ca in manganese ores facilitates the formation of perovskite phase, which enhances both the O_2 release and reactivity. The manufactured calcium manganite demonstrates higher oxygen release capacity and CH_4/syngas conversion compared to the four natural ores, offering another effective way of increasing fuel conversion in the fuel reactor.

In conclusion, the fuel conversion in CLC could be improved using the novel volatiles distributor, as demonstrated in both cold-flow model fluidized bed and CFD simulations, and effective manganese-based oxygen carriers characterized by sufficient mechanical stability and economic feasibility.

Keywords: Chemical looping combustion, CO_2 capture, Volatiles distributor, Gas-solids contact, Chemical looping with oxygen uncoupling, Manganese ores, Calcium manganite

List of Publications

This thesis is based on the following papers, which are referred to in the text according to their Roman numerals:

Paper I
Xiaoyun Li, Anders Lyngfelt, Tobias Mattisson.
An experimental study of a volatiles distributor for solid fuels chemical-looping combustion process (2021)
Fuel Processing Technology, 220, 106898

Paper II
Xiaoyun Li, Anders Lyngfelt, David Pallarès, Carl Linderholm, Tobias Mattisson.
Investigation on the Performance of Volatile Distributors with Different Configurations under Different Fluidization Regimes (2022)
Energy & Fuels, 36, 17, 9571-9587

Paper III
Xiaoyun Li, Anders Lyngfelt, Carl Linderholm, Bo Leckner, Tobias Mattisson.
Performance of a volatiles distributor equipped with internal baffles under different fluidization regimes (2022)
Powder Technology, 409, 117807

Paper IV
Xiaobao Wang, Xiaoyun Li, Lan Yi, Anders Lyngfelt, Tobias Mattisson, Xiaoqin Wu, Hao Luo, Qingang Xiong.
CFD modeling of a fluidized bed with volatiles distributor for biomass chemical looping combustion combustion (2024)
Chemical Engineering Science, 295, 120211

Paper V
Xiaobao Wang, Xiaoyun Li, Lan Yi, Anders Lyngfelt, Tobias Mattisson, Xiaoqin Wu, Qingang Xiong, Hao Luo.
Numerical Evaluation and Optimization of Volatiles Distributors with Different Configurations for Biomass Chemical Looping Combustion
Submitted for publication

Paper VI
Xiaoyun Li, Robin Faust, Anders Lyngfelt, Pavleta Knutsson, Tobias Mattisson.
Non-calcined manganese ores as oxygen carriers for chemical looping combustion with oxygen uncoupling in a circulating fluidized bed reactor system
Submitted for publication

Paper VII
Xiaoyun Li, Robin Faust, Victor Purnomo, Daofeng Mei, Carl Linderholm, Anders Lyngfelt, Tobias Mattisson.
Performance of a perovskite-structured calcium manganite oxygen carrier produced from natural ores in a batch reactor and in operation of a chemical-looping combustion reactor system
Submitted for publication

Contribution report

Paper I	Principal author with main responsibility for all the experimental work, data collection, analysis, and writing.
Paper II	Principal author with main responsibility for all the experimental work, data collection, analysis, and writing.
Paper III	Principal author with main responsibility for all the experimental work, data collection, analysis, and writing.
Paper IV	Shared first authorship with contributions with respect to idea generation, analysis of results, discussions, and writing.
Paper V	Supporting author with responsibility for data provision, visualization, discussion, and editing of the paper.
Paper VI	Principal author with main responsibility for all the experimental work, data collection, analysis, and writing.
Paper VII	Principal author with main responsibility for all the experimental work, data collection, analysis, and writing.

Acknowledgements

My heartfelt gratitude goes to my supervisors Anders Lyngfelt, Tobias Mattisson and Carl Linderholm. Your guidance, support, and insightful discussions have been invaluable throughout this research journey. Anders, thank you for always being there to address my queries with proof, discuss every detail of the problem, and wisely guide me to achieve a deep understanding. Tobias, thank you for constantly bringing in fresh perspectives and posing thought-provoking questions, thereby enriching the discussions. Carl, thank you for your guidance and support in the lab, and efforts in critically reading and commenting my papers.

The Swedish Energy Agency (project number 46626-1) and Åforsk Foundation (Ref. 21-277) are gratefully acknowledged for their financial support. These fundings have enabled me to dedicate myself to the research on the volatiles distributor and manganese-based oxygen carriers, and to attend conferences for knowledge enrichment and professional networking.

I would like to thank Professor David Pallarès and Professor Bo Leckner for making time to answer my questions and providing me with valuable input on my research on volatiles distributors. I would also like to thank my master's classmate, Dr. Hao Luo, for helping me conduct the first simulation work of the volatiles distributor.

The wonderful research journey concerning manganese-based oxygen carriers could not have been as successful, interesting, and fascinating without the help of many individuals. Robin Faust, thank you for bringing me to the magical micro world to look at my oxygen carrier stones with your expert-eyes. Daofeng Mei and Victor Purnomo, thank you for being beside me at the beginning of the project to help unravel the complexities of the experimental systems and provide valuable insights for data analysis.

I am also grateful for the support of the lab angels, Ulf Stenman, Rustan Hvitt, Jessica Malene Bohwalli, and Johannes Öhlin. Thank you all for always being there to help. Thanks Ulf for your dedication in assisting me in my experimental work at the beginning of my PhD study. Rustan, thank you for fabricating these high-tech but simple tools and helping me overcome seemingly impossible obstacles with my reactors.

I'd like to express my gratitude to Marie Iwanow and Katarina Bergkvist, our office angels, for fostering a caring, organized, supportive, and professional environment at Energy Technology.

My heartfelt thanks also go to my colleagues: Amir, Ivan, Ivana, Felicia, Nasrin, Nauman, Fredrik, Mariane, Magnus, Henrik, Pavleta, Carolina, Farha, Azka, Guillermo, Alla, and other members of both the Chemical Looping and Fluidization groups for their collaboration and companionship. Engaging presentations and discussions during group meetings, as well as informal conversations, have sparked further interest in my research and made the work more enjoyable.

I'm also grateful to everyone at Energy Technology for creating an amazing, creative, encouraging, and energetic working environment. Each one of you shines brightly!

Lastly, but most importantly, I extend my heartfelt thanks to my family and dear friends in China. Despite being far away and perhaps not fully understanding my work at Chalmers, your unwavering support means everything to me. I love you all!

Xiaoyun Li

Gothenburg, May 2024

Table of Contents

1 Introduction

1.1 Background

In recent years, with the higher frequency and intensity of weather extremes, climate change attracts more and more attention. The global atmospheric CO_2 concentration increases steadily and reached an annual average 417 ppm in 2022 [1]. In addition, there is still a huge amount of CO_2 emitted every year, corresponding to around 40.7 $GtCO_2$/year in 2022 [1]. The estimated carbon budget for having a 50% chance to limit global warming to 1.5 °C has reduced to 275 $GtCO_2$ from the beginning of 2024 [1]. This budget would be exhausted already within 7 years at the current CO_2 emission rate. Even though considerable efforts have been made to reduce greenhouse gas (GHG) emissions, it will still be difficult or perhaps even impossible to meet the Paris Agreement's temperature goal. Due to the near-linear relationship between cumulative anthropogenic CO_2 emissions and global warming, the temperature will continue to increase until the net zero CO_2 emission target is reached. As the Intergovernmental Panel on Climate Change (IPCC) reports in the Sixth Assessment Report, global warming will exceed both 1.5 °C and 2 °C during the 21st century unless deep reductions in CO_2 and other greenhouse gas emissions occur in the coming decades [2]. Carbon removal technologies are necessary to meet the CO_2 budget in all scenarios considered by IPCC. Bioenergy carbon capture and storage (BECCS), considered to be the carbon removal technology with the highest potential, will play an important role if climate targets are to be achieved [3].

1.2 Chemical looping combustion of biomass

Chemical-looping combustion of renewable biomass (Bio-CLC) with carbon transportation and storage, as a promising BECCS technology, could play an important role for achieving negative emissions since CO_2 from combustion can be provided in pure form without the need of costly and energy-consuming gas separation. As shown in Figure 1, biomass absorbs CO_2 in air through photosynthesis and can be utilized by chemical looping combustion (CLC) to produce heat and power. A net negative flow of CO_2 is achieved by combining photosynthesis, bio-CLC, and storage of captured CO_2 in aquifers or depleted gas and oil fields [4]. In addition to CLC of biomass, CLC can be used with other fuels as well as in combination with steam methane reforming to produce blue hydrogen [5]. CLC employs two interconnected fluidized-bed reactors: the air reactor (AR) and the fuel reactor (FR). In the AR, oxygen carrier particles, typically metal oxides, are oxidized by oxygen in air. Subsequently, the oxidized oxygen carrier is transported to the FR, where it is reduced by fuel. The resulting reduced oxygen carrier then circulates back to the AR to be regenerated for a new redox loop. Ideally, pure CO_2 is obtained after the condensation of steam in the flue gas of the FR and can be compressed and transported for geological storage. One of the key advantages of CLC is its inherent CO_2 capture without the need for costly and energy-consuming gas separation. Additionally, as the AR is devoid of fuel, the absence of fuel contaminants in the AR flue gas allows for higher-temperature heat

extraction, i.e. raised steam data. Conversely, fuel contaminants, such as SO_x, NO_x and aggressive ash contaminants like alkali, are concentrated in the flue gas of FR, which could be an advantage as the gas flow in this reactor is significantly smaller compared to the flow in the air reactor [6].

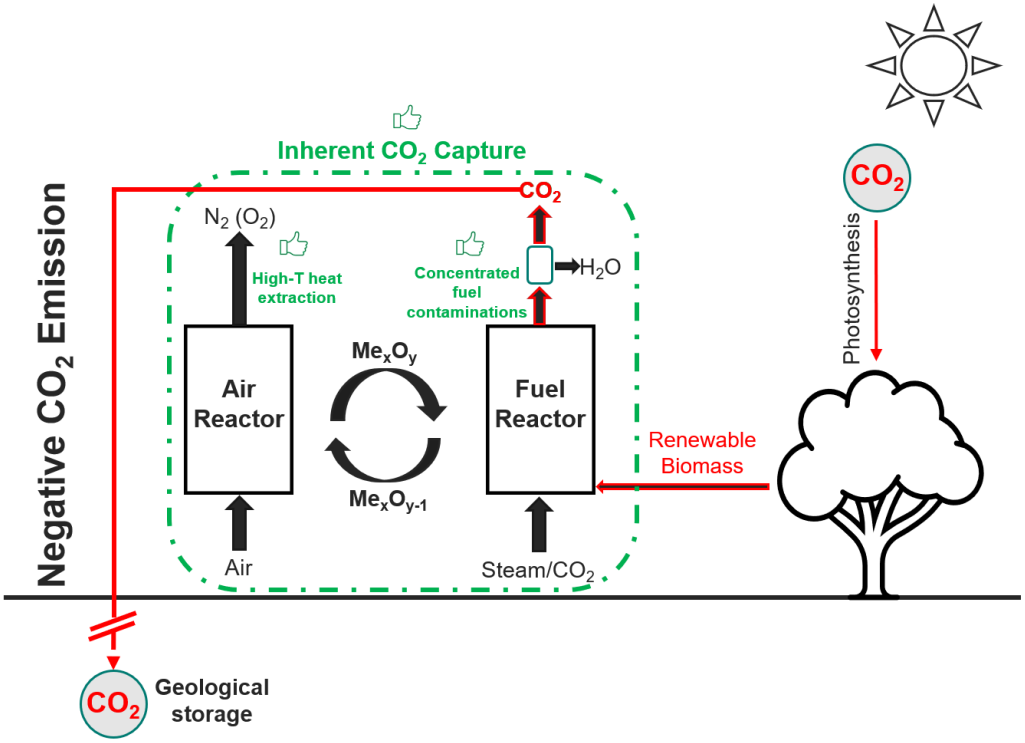

Figure 1. Chemical-looping combustion of renewable biomass as a carbon removal technology.

The process of solid fuel conversion in the FR is illustrated in Figure 2. Once the solid fuel is introduced into the FR at high temperature, it dries rapidly. After this, the devolatilization (R1) of the solid fuel takes place to generate char and volatiles [7]. Subsequently, the volatiles, containing CO, H_2 and hydrocarbons, will react directly with the oxygen carrier in the FR through reaction R4 for normal CLC process. The gasification (R2 and R3) of the char generates H_2 and CO which reacts with oxygen carriers directly (R4) in the normal CLC process. To facilitate gasification, which is slow, fuel particle size can be decreased as compared to normal combustion.

Then the reduced oxygen carriers in the fuel reactor will be transferred to the air reactor and oxidized by the air (R5). After oxidation, the oxygen carriers are looped back to the fuel reactor to react with the fuel again, thus establishing a continuous process. Slightly deviating from normal CLC, CLC employing oxygen carriers capable of releasing molecular oxygen is known as chemical-looping combustion with O_2 uncoupling (CLOU), which has been shown to facilitate the conversion of both volatiles and char derived from solid fuels [8-10]. The main fuel conversion processes of CLC and CLOU are schematically illustrated in Figure 2.

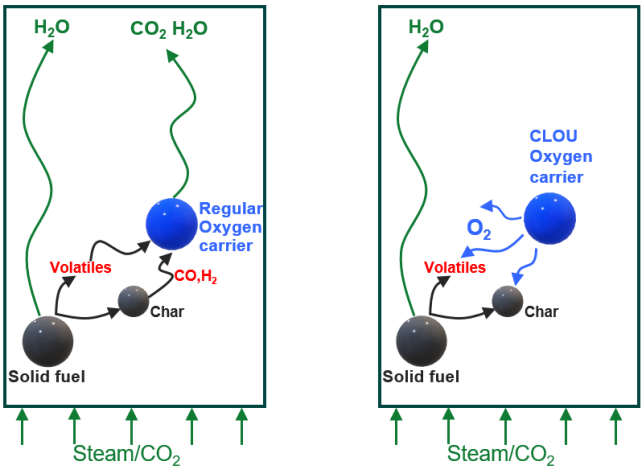

Figure 2. Illustration of solid fuel conversion in fuel reactor for normal CLC and CLOU.

$$\text{Solid fuel} \rightarrow \text{Volatile matters} + \text{Char} \quad \text{(R1)}$$

$$C + H_2O \rightarrow H_2 + CO \quad \text{(R2)}$$

$$C + CO_2 \rightarrow 2CO \quad \text{(R3)}$$

$$C_nH_{2m} + (2n + m)Me_xO_y \rightarrow (2n + m)Me_xO_{y-1} + nCO_2 + mH_2O \quad \text{(R4)}$$

$$Me_xO_{y-1} + \frac{1}{2}O_2 \rightarrow Me_xO_y \quad \text{(R5)}$$

Unconverted combustibles can often be observed at the outlet of the fuel reactor, and they are critical for the performance of CLC especially for high-volatile fuels like biomass [11-15]. There are two sources of these unconverted gases, i.e. char gasification products and volatiles. Char gasification products could be oxidized more or less completely because of the good contact with the oxygen carriers [16]. A huge amount of volatiles is formed after devolatilization in case of biomass. The substantial volatiles release in combination with the upwards flow direction of the fluidization gas may lead to a strong local plume of reducing gas near the biomass injection port. This will yield a limited contact between the volatiles and oxygen carriers in the fuel reactor bed and thereby a large amount of volatiles may leave the reactor unconverted.

Linderholm, et al, [7] investigated the CLC of solid fuels with different volatiles contents in a 10 kW unit, and found a much lower gas conversion rate of solid fuels with higher volatiles content, which indicates that the volatiles released from the solid fuel have insufficient contact with the oxygen carriers in the FR. A comparison of different fuel feeding positions, above-bed and in-bed, showed that the in-bed fuel feeding method can increase the contact between the volatiles and the oxygen carriers which significantly improves gas conversion [7]. Similarly the gas conversion in a 100 kW unit using low-volatile fuel was high [17]. Ströhle et al. [18] investigated the performance of CLC of Calenturitas coal in a 1 MW_{th} unit, and found significant amounts of combustible gases at the fuel reactor exit, which resulted from the incomplete conversion of devolatilization and gasification products due to the limited gas/solid contact in the fluidized bed. Another MW-scale operation of bio-CLC also indicates that the

volatiles conversion is, to a significant extent, limited by the mixing of combustibles and oxygen carrier particles [19]. Petersen and Werther modelled a circulating fluidized-bed gasifier for sewage sludge, which has high volatiles content, and found that plumes with high pyrolysis gas concentrations were formed in the vicinity of the fuel feeding port and lateral mixing of the gas was not complete [20]. A similar type of behavior could be expected in the fuel reactor of a CLC-unit.

Going from small pilots to large-scale will greatly increase the cross-sectional area of fluidized-beds, and the volatiles can be expected to form a stronger local plume over the fuel entry, with the consequence of reduced contact between volatiles and oxygen carriers. Thus, it is motivated to consider solutions that can improve the contact and enhance the reaction between the volatiles and the oxygen carriers in order to reach a higher gas conversion.

1.3 Methods for improving gas conversion in fuel reactor

There are several ways to decrease or remove remaining combustibles in the flue gas of the fuel reactor. Firstly, unconverted gases can be addressed by addition of pure oxygen at the outlet of the fuel reactor, which is often referred to as oxygen polishing [21]. However, important costs of the CLC process stem from oxygen production for conversion of remaining combustible gases and expenses related to oxygen carriers. The latter cost is also related to the degree of fuel conversion in the FR and thus the need for oxygen [22, 23]. Hence, to assure the economic viability of CLC on a large scale, it is imperative to develop solutions to minimize the presence of unconverted gases in the exit of FR and identify cost-effective oxygen carriers, preferably characterized by high reactivity and long lifetimes.

Secondly, different designs and modifications of the fuel reactor have been proposed aiming for higher fuel conversion. A two-stage fuel reactor was proposed and proved to have better combustion performance compared to previous CLC facilities [24]. Internals, i.e. vertical or horizontal tubes, fitted in fluidized-beds reduce bubble size, can increase the emulsion voidage, and thereby increase the overall residence time of reactant gas in the bed [25]. Massimilla and Johnstone found that a fluidized-bed with baffle grids had much higher gas conversion than the non-baffled fluidized-bed [26]. Guío-Pérez et al. [27] investigated the influence of ring-type internals equipped inside the fuel reactor, which showed positive effect on the solids residence time. Pérez-Vega et al. [28] modified the fuel reactor of a 50 kW_{th} unit by the ring-type internals in the upper part of the reactor with the objective of improving the solids distribution and enhancing the gas-solids contact. An improved gas conversion was achieved. However, the effects of such internals would likely be smaller in large-scale units with bigger cross-sections. First proposed in a Swedish patent, the concept of a volatile distributor (VD) could improve the lateral distribution of volatiles in fluidized beds [29]. In principle, the concept includes a downward opened box located in the bottom bed with distribution holes on the sides. The “box” composed of arms allows for a distribution of volatiles over the cross section. The limited open area of the distribution holes on the sides allows for volatiles to spread out across the box and be introduced evenly in the bed, thus avoiding the formation of a local plume. Lyngfelt and Leckner [22] applied this concept into the conceptual design of a 1000 MW_{th} boiler for CLC

of solid fuels. Gogolev et al. [30] implemented a VD in a 10 kW_{th} unit for bio-CLC, which exhibits improved gas conversion efficiency in the fuel reactor. However, detailed investigations into the VD's performance under various conditions were lacking prior to this study.

Thirdly, more reactive oxygen carriers could also improve the fuel conversion in the fuel reactor. More than 70 different oxygen carriers have been tested in actual operation of CLC pilots, of which more than 3000 h are with solid fuels [16]. Oxygen carriers for solid fuels being studied range from low-cost to high-reactivity materials, i.e. ilmenite, iron ores, manganese ores or synthesized oxygen carriers [31-36]. Some ores and waste materials have low cost and show reasonable conversion potential [37-39]. Some synthetic materials have shown higher potential to improve the fuel conversion in the fuel reactor [40-42]. Chemical-looping with oxygen uncoupling (CLOU) is a method proposed for improved or even full gas conversion in fuel reactor, since CLOU oxygen carriers can release gaseous oxygen, which can react with solid, liquid and gaseous fuels [10]. Mattisson et al. [10] and Leion et al. [8] showed that the conversion rate of solid fuels can be improved significantly by CLOU compared to conventional CLC. Three such potential mono-metal oxide systems with thermodynamic properties relevant for CLOU have been investigated, namely CuO/Cu_2O, Co_3O_4/CoO, and Mn_2O_3/Mn_3O_4 [8-10, 43-45]. Copper is effective for CLOU but may have durability issues due to its low melting point and poor physical integrity [43, 45, 46]. Cobalt oxide systems pose health and environmental risks, making them less desirable [46]. Manganese, on the other hand, is abundant and cost-effective. A low temperature is required for the reoxidation to Mn_2O_3 in AR, which also means a slow reaction rate in the AR [46]. However, this drawback can be addressed by doping manganese with other elements. Both binary systems such as $(Mn_yFe_{1-y})O_x$, $(Mn_ySi_{1-y})O_x$, $(Mn_yNi_{1-y})O_x$, $(Mn_yMg_{1-y})O_x$, $(Mn_yCu_{1-y})O_x$ [43, 46-52], and ternary systems such as Mn-Fe-Si, Mn-Fe-Mg, Mn-Fe-Ti [53, 54], have been extensively investigated.

$(Mn_yFe_{1-y})O_x$ combined oxides form the solid solution bixbyite, $(Mn,Fe)_2O_3$, in the temperature range 700-950 °C based on the phase equilibrium of the Mn-Fe oxide system [55, 56]. $(Mn,Fe)_2O_3$ combined oxides are capable of releasing considerable amounts of gas phase O_2 through a phase transition from bixbyite to spinel via reaction R6 [49-52, 57]. The O_2 release of $(Mn,Fe)_2O_3$ is closely related to the mixing ratio of Mn and Fe, the temperature, and the surrounding O_2 partial pressure [46, 56].

$$6(\mathrm{Mn,Fe})_2\mathrm{O}_3 \leftrightarrow 4(\mathrm{Mn,Fe})_3\mathrm{O}_4 + \mathrm{O}_2 \quad \text{(R6)}$$

The combined Mn-Si oxides are particularly interesting owing to the two-step decomposition mechanism among the Mn-Si oxides, i.e. braunite (Mn_7SiO_{12}), rhodonite ($MnSiO_3$), and tephroite (Mn_2SiO_4), as shown in reaction R7 and R8. Braunite can be formed from the reaction between manganese oxide and silica in air [58]. The temperature for O_2 release from braunite through reaction R7 in presence of SiO_2 is approximately 1050 °C at an oxygen partial pressure of 0.05 atm, which is higher than 800 °C for pure Mn_2O_3 [46, 56]. This suggests that braunite should be a suitable oxygen carrier for CLOU.

$$\left(\frac{2}{3}\right)\mathrm{Mn_7SiO_{12}} + 4\mathrm{SiO_2} \leftrightarrow \left(\frac{14}{3}\right)\mathrm{MnSiO_3} + \mathrm{O_2} \quad \text{(R7)}$$

$$\left(\frac{2}{3}\right)\mathrm{Mn_7SiO_{12}} + \left(\frac{10}{3}\right)\mathrm{MnSiO_3} \leftrightarrow 4\mathrm{Mn_2SiO_4} + \mathrm{O_2} \quad \text{(R8)}$$

In addition to the above combined manganese oxide systems, the Mn-Ca system can form calcium manganite ($CaMnO_{3-\delta}$), which has a stable perovskite structure being able to release O_2 through reaction R9 without changes in the phase structure. The δ factor expresses the degree of oxygen deficiency in the structure, which is related to the surrounding conditions. In the AR with oxidizing atmosphere, δ_{ar} will be smaller whereas δ_{fr} will be larger since the FR is in reducing atmosphere. The equilibrium O_2 partial pressure over the $CaMnO_3$ system is a function of the oxygen deficiency factor δ and temperature [59]. It was also found that the O_2 uncoupling rate of calcium manganite oxygen carriers is notably slower compared to CuO [60, 61]. However, the oxidation of gaseous fuels can occur through direct reactions between the fuel and oxygen carriers, as well as reactions between the fuel and molecular oxygen released from the oxygen carriers. Despite the slower O_2 release, small-scale CLC operations utilizing calcium manganite as oxygen carrier have demonstrated high fuel conversions [62, 63]. This suggests that the reactivity of CLOU materials does not solely depend on the amount and rate of oxygen release by the oxygen carriers and even small amount of O_2 released can affect the fuel conversion positively.

$$\mathrm{CaMnO_{3-\delta_{ar}}} \leftrightarrow \mathrm{CaMnO_{3-\delta_{fr}}} + \frac{1}{2}(\delta_{\mathrm{fr}} - \delta_{\mathrm{ar}})\mathrm{O_2} \quad \text{(R9)}$$

As CLC technology moves from pilot-scale to larger operational scales, the significance of developing robust and economically feasible oxygen carriers becomes increasingly pronounced. Natural manganese ores, readily available and commercially abundant, are gaining more attention than combined manganese oxides synthesized from purer compounds. The presence of impurities in these natural ores may positively influence their reactivity towards fuel.

1.4 Aim and scope

Despite the tremendous advances that have been made with respect to chemical-looping, there is nevertheless room for improvement. The overall aim of this thesis is to investigate different solutions to improve gas conversion in the fuel reactor of a chemical-looping combustion system. More specifically two main pathways have been explored in this work: i) improving the gas-solids contact in the fuel reactor through the use of a novel volatiles distributor and ii) development of effective and low-cost oxygen carriers which can realistically be used together with biomass.

1.4.1 Part I: Volatiles distributor

In the fuel reactor, a local plume of volatiles released rapidly from the solid fuel in the fuel reactor may cause poor gas-solids contacting and thus lower the gas conversion in the fuel reactor. Such a plume would be more pronounced going from small-scale to commercial size units with high-volatile fuels, i.e. biomass. The aim of this part of work is to introduce and

investigate a novel concept called volatiles distributor (VD) aiming for a more even distribution of volatiles at the bottom of the fuel reactor and better contact between volatiles and oxygen carrier, and thus improve combustion efficiency.

Part I of this thesis summarizes the investigation of the VD in a cold-flow fluidized-bed model in both experimental and modelling aspects. The VD with different configurations were applied in different fluidization regimes. The performance of the VD with respect to the uniformity of the lateral distribution of volatiles is analyzed and evaluated based on the experimental results presented in **Paper I-III**.

To deeply understand VD's impact on hydrodynamics, pioneering three-dimensional full-loop CFD simulations of the fluidized bed equipped without and with the VD were conducted using a Eulerian multiphase granular model as presented in **Paper IV-V**. Three drag models, i.e., Gidaspow, Filtered, and two-step EMMS/bubbling, were evaluated against experimental data. After identifying the most suitable drag model, the effects of the VD on the physicochemical behavior of the fluidized-bed were fully investigated to obtain further validation against experimental results and support design, optimization, and scale-up of the VD.

1.4.2 Part II: Manganese-based oxygen carriers

As the cornerstone of CLC, the selection of oxygen carrier is both complex and crucial and dependent on the application. In chemical looping with oxygen uncoupling (CLOU), the conversion of volatiles and char in FR can be notably enhanced, attributed to the ability of oxygen carriers in CLOU to release oxygen to the gas phase.

Part II of this thesis summarizes the investigation of the potential for using low-cost raw materials as CLOU oxygen carriers, i.e. non-calcined manganese ores and perovskite-structured calcium manganite produced from commercial and abundant natural ore and manufactured using simplified technologies suitable for large-scale production. The performance of these CLOU oxygen carriers were tested in a continuously operating 300 W circulating fluidized-bed system. The detailed results are presented in **Paper VI** and **VII**.

2 Materials and Methods

2.1 Part I: Volatiles distributor

2.1.1 Concept of volatiles distributor

If a box with an opening downwards is immersed in a fluidized bed, it is known that the inside of the box will be free of bed materials and the bed surface level will be at the bottom edge of the box. However, if holes are made in the sides of the box, the bed level inside the box will increase to the level of the holes and the fluidization gas can pass through the holes as shown in Figure 3. If gases like volatiles are injected into this box above the side holes level, it will pass through the holes creating a pressure drop over the holes. The increased pressure will lower the bed level inside the box.

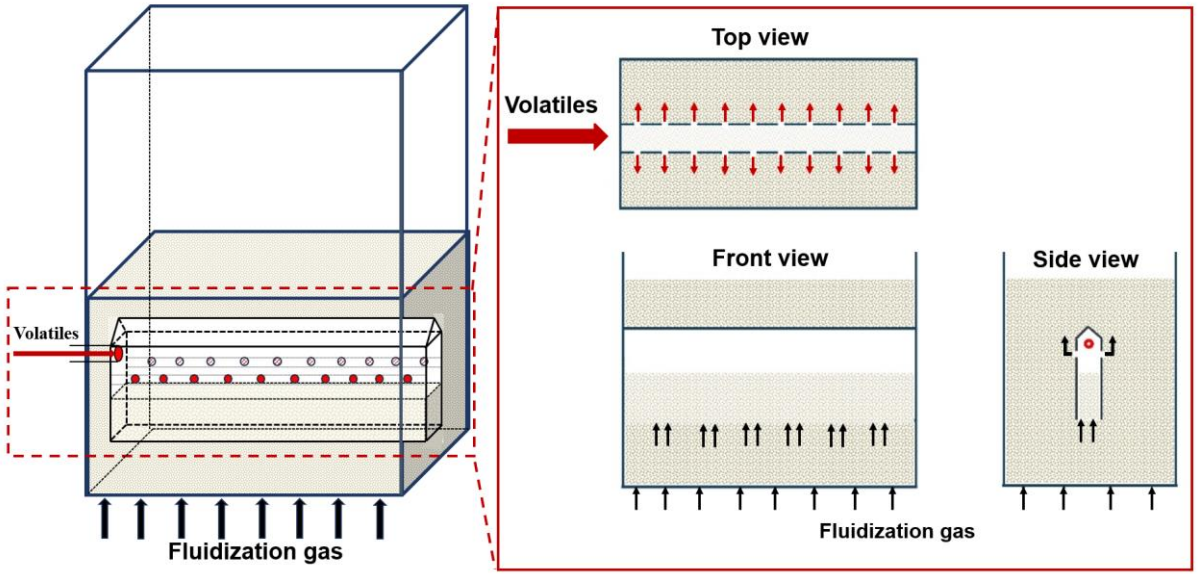

Figure 3. Illustration of a VD with side holes as a downward open box immersed at the bottom of a fluidized bed.

Such a box can be extended to an arm and if a system of such arms is built and extended across the cross-section of a fluidized-bed, gases can be distributed via the holes in the sides across the whole cross-section. Furthermore, this system can also be connected to the location where fuel is introduced in order to distribute the volatiles over the cross-section [22]. Thus, the fuel can be added on the top of the bed in a special fluidized prechamber, for instance above the return of solids from the cyclone. The freeboard of this chamber is connected to the arms of the VD, allowing the bed material to flow freely out of this prechamber at a lower height, beneath the weir separating the freeboard of the prechamber from the main fuel reactor, see Figure 4. In this work, the devolatilization process is excluded, and a simulated volatiles gas is used to mimic the rapidly released volatiles from solid fuels.

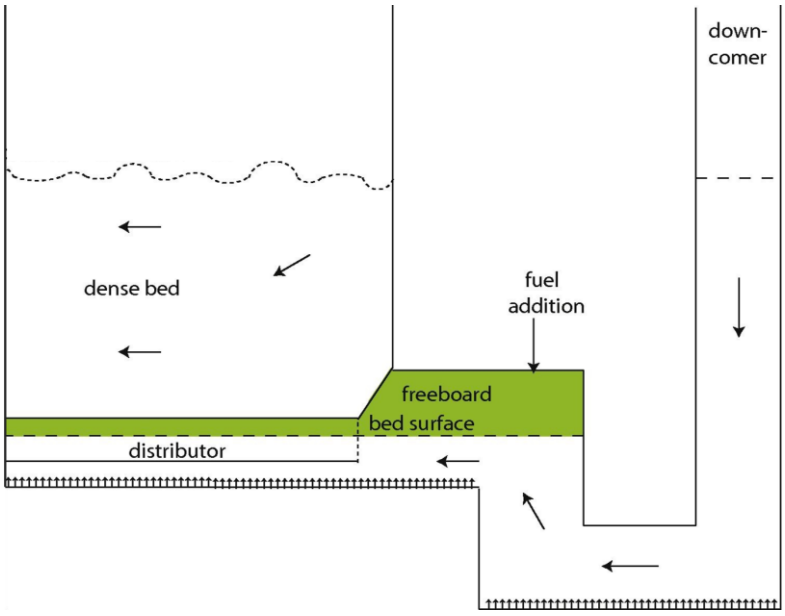

Figure 4. Illustration of a way to connect volatiles release with volatiles distributor, with the green area showing the gas phase above the bed in prechamber and the connected VD [22].

2.1.2 Cold-flow fluidized-bed model fluidized bed

The cold-flow fluidized-bed model includes a wind box, a riser and a cyclone. The riser has a length × width × height of 700 mm × 120 mm × 8500 mm. The front side of the riser is made from Perspex glass which allows visual observation of fluidization inside the VD. The VD is installed at the bottom of the riser at a height of 114 mm, i.e. from the bottom of the VD to the bottom of the riser. In this work, the volatiles are simulated using a mix of air and CO_2 as a tracer gas. There is an injection hole for simulated volatiles at the front plate, which allows the simulated volatiles to flow into the VD, cf. Figure 5.

Along the height of the riser, there are twenty-four taps for pressure measurements. There are two pressure taps to measure the pressure drop between the inside and outside of the VD at the same height as the distribution holes. The pressure measurement inside the VD, is in the right top corner of the front plate, i.e. the pink crossed circle shown in the gas sampling tube position of Figure 5 (b).

There are thirteen gas sampling tubes in the experimental system, where gases are measured, and which show the degree of gas mixing. These are placed at three different levels of the fluidized bed: i) the higher-level ones (HSV1-HSV6), ii) the lower-level ones (LSV1-LSV6) and iii) one for sampling the gas inside the VD, as shown in Figure 5 (b). For each measurement position, the gas flows into the gas analyzer for 210 s in total, the first 90 s is for stabilization and the remaining 120 s is for recording data to calculate the average concentration of CO_2, here used to track simulated volatiles.

Glass beads are used as bed material for this study, having a density of 2600 kg/m^3 and a particle size range from 250 μm to 425 μm, which is similar to the bed materials used in boilers [64]. Further details on the solids are given in Paper I.

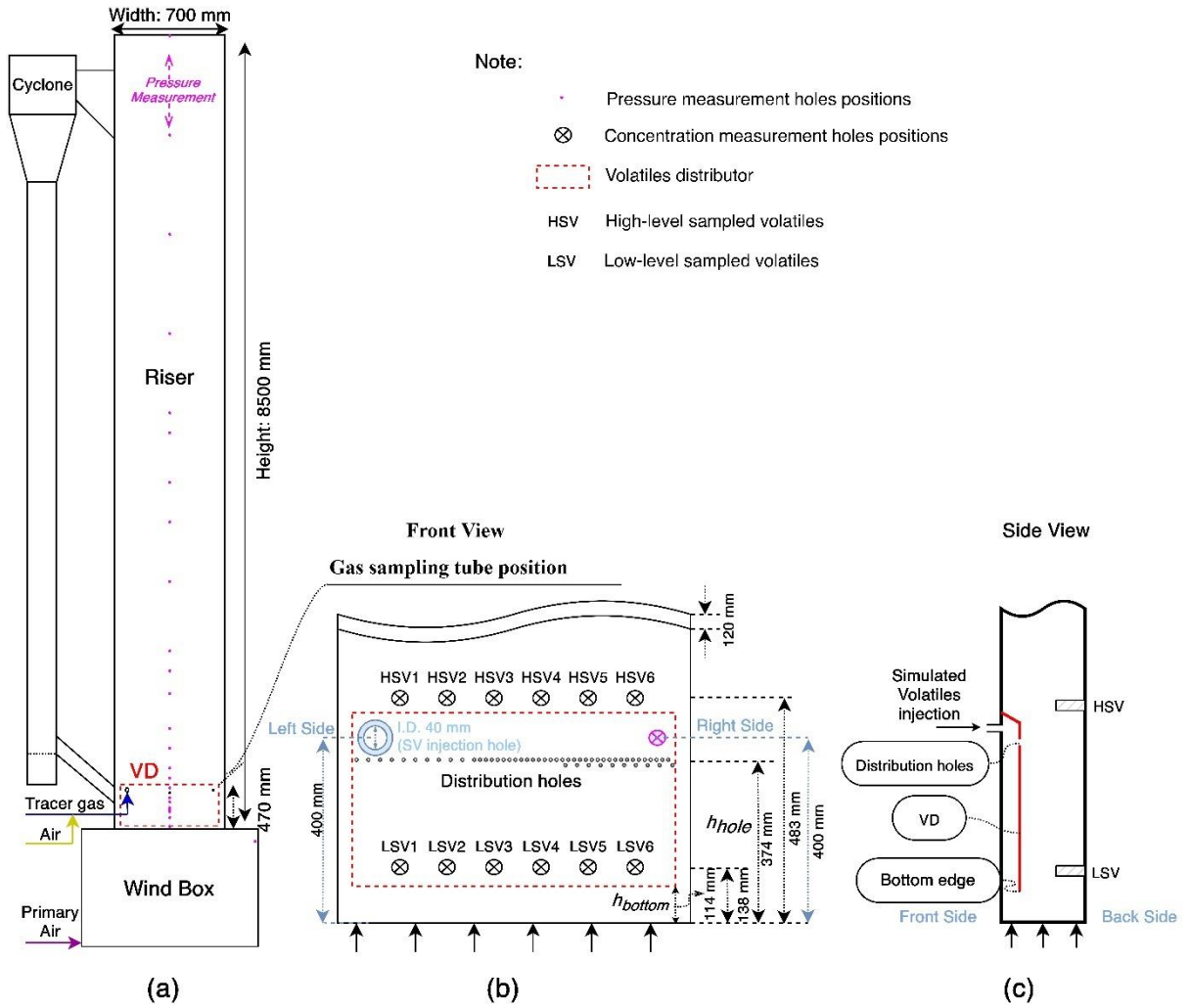

Figure 5. (a) Cold-flow circulating fluidized-bed model equipped with the VD and pressure and CO_2 concentration measurement systems; (b) Front view of the riser bottom, the distribution holes are seen in detail in Figure 6; (c) Side view, the side view with more details is shown in Figure 9.

2.1.3 Different designs of the volatiles distributor

The performance of the VD was investigated in this cold-flow fluidized-bed model. Figure 6 presents the sketch of the VD, which is attached on the bottom front plate of the fluidized bed. The design of the distribution holes, i.e. the arrangement of the holes and the open area of the holes, is vital to the performance of the VD on the horizontal distribution of the volatiles. Hence, different configurations of the distribution holes (Mode A and Mode B) and different open areas of the distribution holes (Mode 1 and Mode 2) were investigated in this work. Mode 1A and Mode 1B have the same open area and number of holes, i.e. 58 holes, but different distribution of the holes. Mode 1A has the evenly distributed open area along the length of the VD. However, Mode 1B has less open area at the left side, i.e. the volatiles injection side but more at the right side, i.e. far away from the volatiles injection side. Mode 2A and Mode 2B have similar arrangements as Mode 1A and Mode 1B except that Mode 2A and Mode 2B have the double open area as well as double number of holes, i.e. 116 holes. The diameter of the distribution holes is 5 mm.

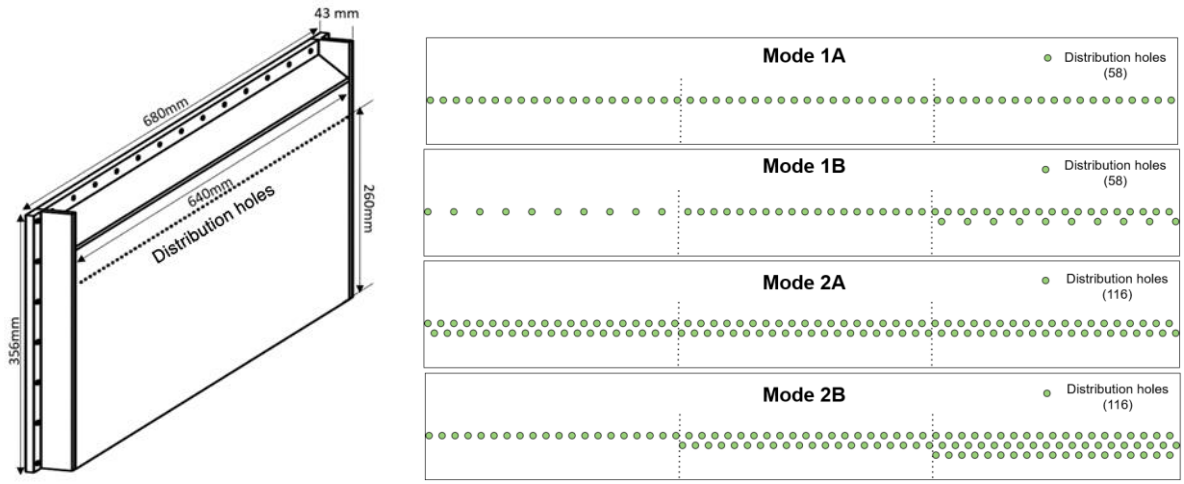

Figure 6. Sketch of the VD and different configurations of the distribution holes.

The internal baffles were designed based on the hourglass concept, and the idea with these was to improve the performance of the VD by reducing the solids movement inside the VD, i.e. to promote a more even volatiles distribution and less risk of volatiles slip below the lower edge of the VD close to the volatiles inlet. As shown in Figure 7, the cross section between the internal baffles is narrowing down going downwards. The ten internal baffles occupy 64.1% of the cross section at the bottom of the VD. Further details are given in Paper III.

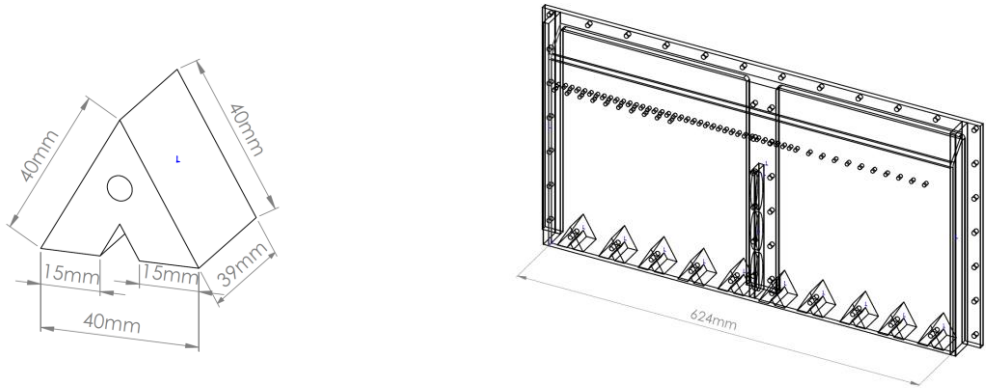

Figure 7. The design of internal baffles and arrangement at the bottom of the VD.

2.1.4 Operational conditions

Fluidization velocity is one of the most important parameters in the field of fluidization. In this case, there are two main incoming flows to consider, the primary air used for main fluidization as well as the flow of the simulated volatiles to the VD box. The latter can represent the fuel injection rate to some extent. Hence, the performance of the VD was investigated under different fluidization velocities and simulated volatiles flows as presented in Table 1. The different flows of simulated volatiles, i.e. volatiles percentage in the total flow including primary air flow and simulated flow, are achieved by changing the air flows for main fluidization and simulated volatiles. The CO_2 flow for simulated volatiles as tracer gas was varied to keep the CO_2 concentration as 1% in the simulated volatiles in order to achieve high measurement accuracy.

The pressure drop over the air distributor plays an important role for the fluidization regime in the riser. Therefore, an investigation of the performance of the VD with different air distributors (AD), i.e. an air distributor with 198 holes (AD198) and an air distributor with 1660 holes (AD1660), was performed. A more detailed discussion about the different types of regimes can be found in Paper II and [65]. An overview of the experimental conditions is presented in Table 1.

Table 1. Overview of the operational conditions.

Air distributor	Volatiles distributor	Internal baffle	Fluidization velocity u_0 [m/s]	Volatiles percentage $\frac{V_{sv}}{V_{sv}+V_{pa}}$	Investigated parameters
AD1660	Without Mode 1A	Without	0.9, 1.8, 2.8, 3.7	10%, 20%, 30%	**Fluidization velocity** **Volatiles percentage** (Paper I [66])
AD1660	Mode 1B Mode 2A Mode 2B	Without	0.9 3.7	10% 30% 10%	**Fluidization regime** **Configuration of distribution holes** (Paper II [67])
AD198	Without Mode 1B Mode 2B	Without	0.9 0.6	30% 30%, 40%	
AD198	Mode 1B	With	0.6	30%, 40%	**Internal baffles** (Paper III [68])
AD1660	Without Mode 1B	Without With	0.6 3.7	30% 40% 10%	

2.1.5 Model description

The Eulerian multi-phase granular model in the ANSYS Fluent version 2023R1 was employed in this work. Three different drag models, i.e., Gidaspow model [69], filtered model [70], and two-step EMMS/bubbling model [71] were chosen and implemented by the user define function (UDF) of Fluent. Details on the models are given in Paper IV.

Governing equations of the Eulerian multi-phase granular model are given in Table S2 in the Supplementary Materials of Paper IV. The kinetic theory of granular flow (KTGF) [72] was used as closures for solids stress and viscosity for the Gidaspow model and two-step EMMS/bubbling model. For the filtered model [70], solids stress and viscosity are described by the filtered model instead of KTGF, as shown in Table S3 in the Supplementary Materials of Paper IV. No-slip and partial-slip boundary conditions were prescribed for the gas phase and solids phase, respectively. The standard k-ε turbulence model was used to describe turbulent flows [73-75], as it requires less computational cost but gives reasonable prediction. Density, viscosity, and mass diffusivity of the gas mixture are determined by the volume-averaged mixing law, mass-weighted mixing law, and kinetic theory, respectively.

Three-dimensional full-loop simulation was adopted, as full-loop simulation can give more reasonable results as compared to single fluidized-bed simulation [76-79]. The total mesh number was up to 4 million to keep 15 grid points on edge of each individual hole. The corresponding average mesh size is about 61 and 55 times of the particle diameter, which is acceptable for the E-E modeling [71]. Further details about the simulation settings are given in Paper IV.

2.2 Part II: Manganese-based oxygen carriers

2.2.1 Oxygen carrier materials

Four types of manganese ores were investigated as oxygen carriers in Paper VI. The elemental composition of these is given in Table 2. The raw materials were crushed and sieved into particles ranging from 90 to 250 µm.

Table 2. Elemental compositions of fresh manganese ores [6].

Mn Ore	LOI* (wt%)	Elemental compositions (wt%)										Total elements§ (wt%)
		Mn	Fe	Si	Al	Ti	Ca	K	Mg	Ba	Na	
Eramet HM	0.9	53.6	7.1	1.7	4.5	0.14	0.07	1.1	0.06	0.37	0	69
Guizhou	0.9	17.7	28.6	7.3	7.4	0.73	0.2	0.24	0.57	0.05	0.04	63
Sibelco Braunite	1.0	55.0	16.2	3.2	0.2	0.01	2.42	0.07	0.38	0.23	0.04	78
UMK	15.1	61.9	3.8	0.9	2.1	0.1	10.72	0.59	0.34	1.78	0.3	83

*LOI=Loss on ignition, i.e., weight reduction of the heat-treated sample upon heating to 1000 °C in air.
§ wt% missing to 100% is oxygen.

A calcium manganite oxygen carrier material manufactured from limestone and Eramet HM manganese ore was investigated in paper VII. The details on the manufacturing procedure are given in Paper VII. The final material was sieved into particles ranging from 90 to 250 µm. The resulting particles were irregular and had a bulk density of 1102 kg/m³ and an average crushing strength of 2.9 N.

2.2.2 300 W CLC reactor system

The oxygen carriers were investigated in a 300 W CLC unit with interconnected fluidized beds, enabling continuous operation with gaseous fuels [6]. The study assessed the CLOU effect of the oxygen carriers, their reactivity towards syngas and CH_4, as well as the integrity of the particles. A schematic illustration of the 300 W CLC reactor and the gas sampling system used in this work are shown in Figure 8. Details on the 300 W reactor system are given in Paper VI and VII.

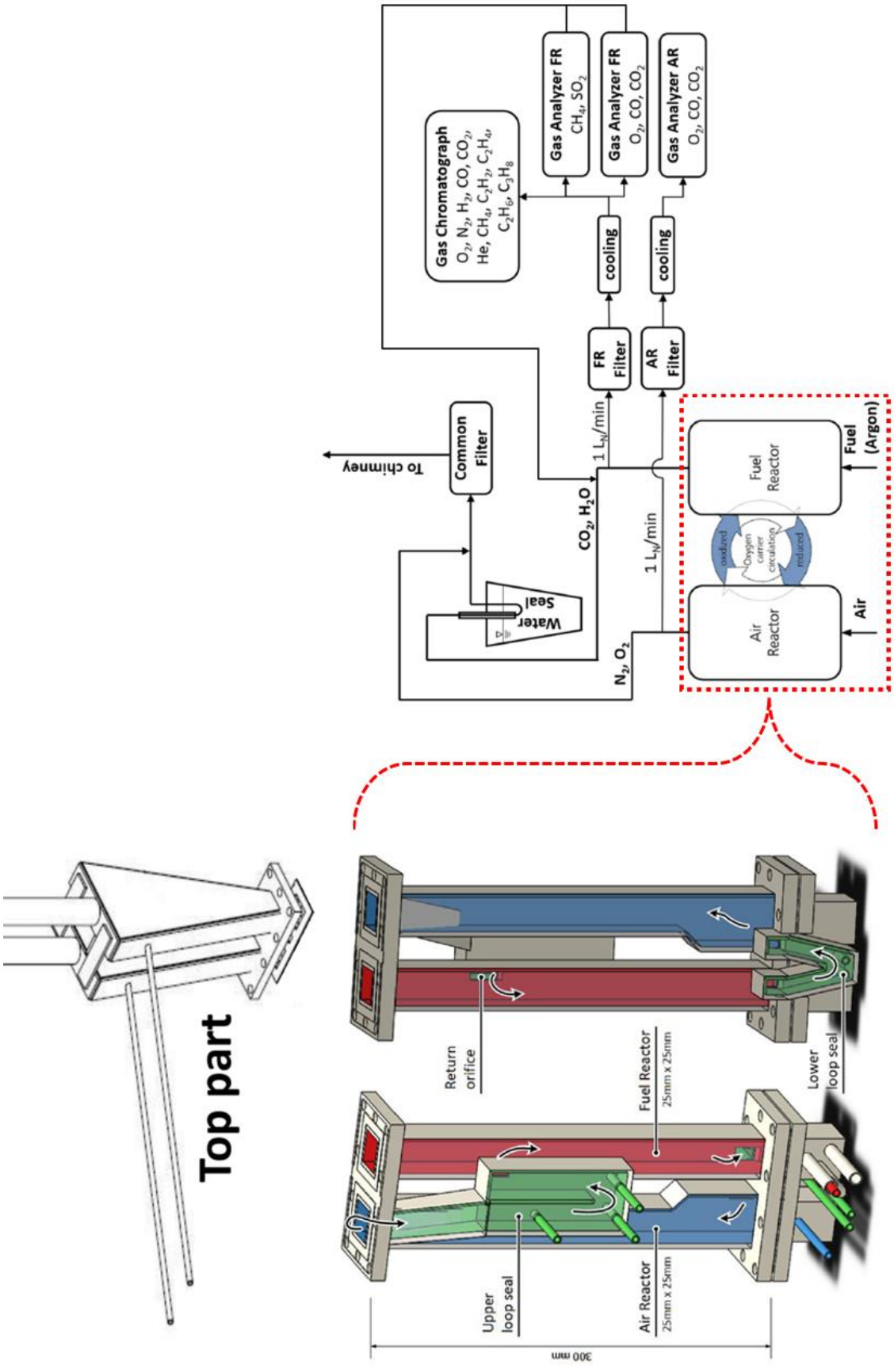

Figure 8. 300 W reactor with the top part (left) and gas sampling system (right).

The basic settings for each campaign in the 300 W reactor system with four manganese ores and calcium manganite are shown in Table 3. Syngas consists of 50 vol% of H_2 in CO, and the methane has a purity of 99.5%.

Table 3. Experimental conditions for four manganese ores and calcium manganite in 300 W CLC reactor system.

Mn ore	Total solids inventory, initial (g)	Campaign	AR air flow (L_n/min)	FR gas	FR flow (L_n/min)	Fuel input (W)	FR temperature (°C)
Eramet HM	350	CLOU	8	Argon	1	0	850 - 950
		CH_4	8	CH_4	1	92 - 160	850 - 950
		Syngas	8	$CO\&H_2$	1	78 - 165	850 - 950
Guizhou	350	CLOU	8	Argon	1	0	850 - 950
		CH_4	8	CH_4	1	186 - 378	850 - 950
		Syngas	8	$CO\&H_2$	1	133 - 365	850 - 950
Sibelco braunite	400	CLOU	8	Argon	1	0	850 - 950
		CH_4	8	CH_4	1	133 - 325	850 - 950
		Syngas	8	$CO\&H_2$	1	125 - 328	900 - 950
UMK	366	CLOU	8	Argon	1	0	850 - 950
		CH_4	8	CH_4	1	167 - 404	850 - 950
		Syngas	8	$CO\&H_2$	1	157 - 477	850 - 950
$CaMnO_3$ Batch 1	300	CLOU	8	Argon	1	0	850 - 950
		Syngas	8	$CO\&H_2$	1	80 - 319	850 - 915
$CaMnO_3$ Batch 2	300	CLOU	8	Argon	1	0	850 - 950
		CH_4	8, 9	CH_4	1	96 - 306	850 - 950

The initial solids inventories of fresh manganese ores and calcium manganite samples are between 300 g and 400 g for both syngas and CH_4 campaigns. The CLOU effect of the oxygen carrier particles is investigated with argon flowing through the FR. Eramet HM, Guizhou, Sibelco braunite, and UMK manganese ores were tested with fuel gas for 8.5 h, 9.0 h, 8.4 h, and 6.3 h, respectively. After CLOU and fuel tests, the reactor system was cooled down in air atmosphere and samples were taken from AR for characterization. After 2 h syngas operation for $CaMnO_3$ batch 1, and after 4.5 h and 29 h of CH_4 operation for $CaMnO_3$ batch 2, calcium manganite samples were taken from AR for characterization and batch-reactor tests.

2.2.3 Batch fluidized-bed reactor system

Both fresh and used calcium manganite samples were tested with respect to their oxygen uncoupling ability and reactivity towards methane and syngas at different temperatures in a batch fluidized-bed reactor system. The used calcium manganite sample was taken from the AR of 300 W unit after 29 h operation with CH_4. The batch fluidized-bed reactor has an inner diameter of 22 mm and is described in details in Paper VII.

During the oxidation period, a flow rate of 900 mL_n/min of 5 vol% O_2 in N_2 was maintained, while 600 mL_n/min of N_2 and 450 mL_n/min of CH_4 or 900 mL_n/min of syngas were employed during the inert and reduction periods.

Tests with silica sand served as blank experiments. 15 g samples were placed in the reactor for CLOU and CH_4 tests. It is not expected that sand would have any CLOU properties but is used in order to characterize the reactor system and establish the degree of back mixing of the gases when switching between different conditions. Further, 2 g samples mixed with 13 g silica sand were used for syngas tests. The CLOU tests measure the oxygen release at different temperatures. The gaseous fuels underwent cycles of oxidation, inert, reduction, and inert

periods, with durations of 600 s, 90 s, 20 s, and 90 s, respectively. Four cycles of syngas tests were conducted for activation before CH_4 tests with the fresh calcium manganite sample. The details can be found in Paper VII.

2.2.4 Material Characterization

Bulk densities of fresh and used particles were measured according to ISO standard 3923-1 by pouring the material into a cylinder of defined volume (25.092 cm^3) through a funnel and weighing the mass of particles in the cylinder. The particle size distribution of the fresh and used particles was obtained by sieving the particles in the ranges of 45, 90, 125, 180, 212 and 250 μm.

The outlet streams of the AR and FR were filtered to trap and collect the fines formed during the operation. Given the total hours of operation, the attrition rate of the oxygen carriers was calculated as the rate of the weight loss in the form of fines per hour of operation with gas fuel, divided by the initial weight of the particles loaded into the reactor [7].

Semiquantitative X-ray Powder diffraction (XRD, Bruker D8 DISCOVER) was used to identify crystalline phases in both fresh and used oxygen carrier samples. Scanning electron microscopy with energy dispersive X-ray spectroscopy (SEM-EDX, FEI ESEM Quanta 20) was used to analyze the morphology and chemical composition.

3 Data Processing and Analysis

3.1 Part I: Volatiles distributor

The results through Paper I to III are mainly based on the recorded data from the pressure and tracer gas concentration measurements. The modelling results through Paper IV and V are based on the recorded data in Paper I - III.

Solids concentration, pressure fluctuations, and height of the dense bed can be obtained from the pressure measurements. The horizontal distribution of the simulated volatiles is obtained by adding tracer gas, i.e. CO_2, to the flow of simulated volatiles, in combination with CO_2 concentration measurements across the horizontal section at the HSV level described in section 2.1.2.

3.1.1 Solids concentration

The average solids concentration, $c_{s,h_{1\to2}}[\mathrm{kg/m^3}]$ between two different heights, h_1 and h_2, can be estimated by the pressure drop as follows with Equation (E1) and (E2) [80].

$$\left|p_{h_1} - p_{h_2}\right| = \left(\rho_s\left(1 - \varepsilon_{g,h_{1\to2}}\right) + \rho_g \varepsilon_{g,h_{1\to2}}\right) g \left|h_1 - h_2\right| \quad \text{(E1)}$$

$$c_{s,h_{1\to2}} = \rho_s\left(1 - \varepsilon_{g,h_{1\to2}}\right) \quad \text{(E2)}$$

3.1.2 Power spectral analysis

Power spectral analysis is often used to determine the dominant frequencies and the frequency distributions of pressure fluctuations in fluidized beds, and it can be used to identify the fluidization regime transitions and validate the hydrodynamic scaling relationships between the pilot-scale and the full-scale units [81, 82]. In this thesis, power spectral analysis of the pressure fluctuations signals using Fast Fourier transform (FFT), being a more objective method compared to the time domain analysis, is used to characterize the fluidization regime. The pressure sampling frequency is 50 Hz in this work, which is sufficient to determine the frequency distribution since the major frequency range of pressure fluctuations is normally below 10 Hz [82]. Details on the equations are given in Paper II.

3.1.3 Standard deviation of pressure

The pressure fluctuations in the fluidized bed may affect the performance of the VD. Hence, the standard deviation of pressure is one method to estimate the fluctuation amplitude, and is calculated as:

$$\sigma = \sqrt{\frac{\sum_{n=1}^{N}(x(n) - \bar{P})^2}{N}} \tag{E3}$$

where N is the total number of data points, $\bar{P}$ is the average value and n = 1, 2, 3, …, N.

3.1.4 CO_2 ratio

In an ideal case, when the injected volatiles are perfectly mixed across the whole cross-section, the CO_2 concentration at different positions of the cross-section will be the same. This ideal average CO_2 concentration is calculated based on the CO_2 flow (MF_{CO_2} $[m_n^3/\mathrm{h}]$), air flow used for simulating volatiles (MF_{SA} $[m_n^3/\mathrm{h}]$) and primary air flow (MF_{PA} $[m_n^3/\mathrm{h}]$) for the main fluidization.

$$c_{cal} = \frac{MF_{CO_2}}{MF_{CO_2} + MF_{SA} + MF_{PA}} \tag{E4}$$

In order to compare the horizontal distribution of simulated volatiles in different cases statistically, a parameter named CO_2 ratio (R) was defined as the ratio between the measured CO_2 concentration (c_m [ppm], with CO_2 in ambient air subtracted) at each measurement position and the ideal average CO_2 concentration in the cross-section of the riser (c_{cal} [ppm]).

$$R = \frac{c_m}{c_{cal}} \tag{E5}$$

A further analysis based on the CO_2 ratios at different positions of the higher level is conducted in order to evaluate the overall performance of the different volatiles distributors under different operational conditions with different air distributors. Here are the parameters used for the evaluations.

The average CO_2 ratio over the six horizontal measurement positions is calculated by:

$$\bar{c}(c_1, c_2, \ldots c_n) = \frac{\sum_{i=1}^{n} c_i}{n} \tag{E6}$$

The standard deviation of the CO_2 ratios is given by:

$$SD = \sqrt{\frac{\sum_{i=1}^{n}(c_i - \bar{c})^2}{n}} \tag{E7}$$

The relative standard deviation of the CO_2 ratios is calculated as:

$$RSD = \frac{SD}{\bar{c}} \times 100\% \tag{E8}$$

The ratio between the highest CO_2 ratio (c_H) to the lowest one (c_L) at the six positions of the higher level is also calculated, which is expressed as c_H/c_L.

3.1.5 Dense bed height estimation inside the VD

The bed material inside the VD is fluidized by a part of the gas introduced in the bottom of the riser. The height of the dense bed inside the VD, h_b (see a sketch of the side view in Figure 9) is estimated from pressure measurements. Geometry gives:

$$h_b = h_{hole} - \Delta h - h_{bottom} \tag{E9}$$

where h_{bottom} is the distance from the air distributor plate to the lower edge of the VD, h_{hole} is the distance from the distributor plate to the level of distribution holes of the VD, and Δh is the distance between the top of the dense bed inside the VD and the level of distribution holes. Δh can be estimated from the pressure difference between the inside VD and the main bed at the height of the hole, and the measured pressure gradient dp/dh on the outside of the VD is assumed to be similar to that of the bed inside the VD.

$$\Delta h = \frac{p_{in} - p_{out}}{\left|\frac{dp}{dh}\right|} \tag{E10}$$

where p_{in} and p_{out} are the pressure above the dense bed inside the VD and the pressure outside the VD in the main riser at the height of the distribution holes of the VD.

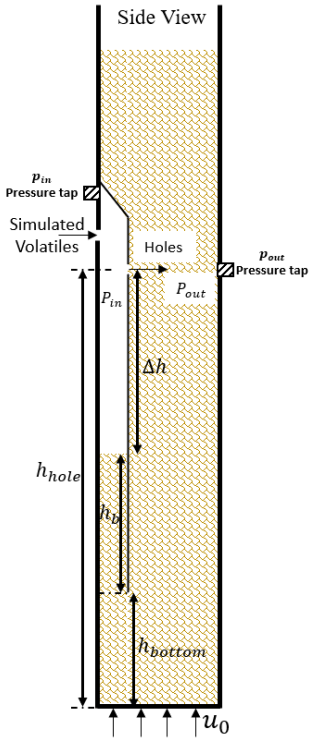

Figure 9. Sketch of the side view of the bottom part of the riser.

3.1.6 Dilution of volatiles inside the VD

The injected simulated volatiles would be diluted by the bottom air from the main fluidization. This dilution affects the horizontal distribution of the simulated volatiles as it will affect the distribution velocity of the gas through the VD. Therefore, the flow of fluidization air from the bottom entering the VD is estimated and the degree of the dilution of the injected simulated

volatiles is also evaluated based on the dilution factors. The method to estimate the gas flow through the distribution holes is introduced in Paper I.

3.2 Part II: Manganese-based oxygen carriers

3.2.1 Fuel conversion in the 300 W reactor

The fuel conversion in the 300 W reactor is assessed with the CO_2 yield γ_{CO_2}, as shown in Equation (E11), which is the ratio of CO_2 volumetric concentration over all the carbon species', i.e. CH_4, CO and CO_2, measured in the outlet gas of FR.

$$\gamma_{CO_2} = \frac{[CO_2]_{FR}}{[CO_2]_{FR} + [CO]_{FR} + [CH_4]_{FR}} \quad \text{(E11)}$$

In the results section, fuel conversions are compared under similar ratios of thermal power of the fuel flow over the bed mass in the fuel reactor under different conditions using various oxygen carriers.

3.2.2 Reactivity in batch reactor

The reactivity of oxygen carriers towards gas fuels in the batch reactor is quantified similarly as in the 300 W reactor by the fuel conversion.

The conversion of the oxygen carrier is defined according to Equation (E12),

$$\omega_i = \frac{m_i}{m_{ox}} \quad \text{(E12)}$$

where m_i is the mass of the oxygen carrier at time i, and m_{ox} is the mass of the fully oxidized oxygen carrier, which is the mass of the oxygen carrier particles added to the reactor, i.e. 15 g for the oxygen release tests and CH_4 tests, 2 g for the syngas tests.

ω_i can also be calculated as a function of time for oxygen uncoupling, methane and syngas tests as shown in Equation (E13), (E14) and (E15) based on mass balances.

$$\omega_{i,\mathrm{CLOU}} = \omega_0 - \int_{t_0}^{t_i} \frac{\dot{n}_{out} M_o}{m_{ox} p_{tot}} \left(2p_{O_2,\mathrm{OC}}\right) dt \quad \text{(E13)}$$

$$\omega_{i,\mathrm{CH_4}} = \omega_0 - \int_{t_0}^{t_i} \frac{\dot{n}_{out} M_o}{m_{ox} p_{tot}} \left(2p_{O_2,OC} + 4p_{\mathrm{CO_2}} + 3p_{\mathrm{CO}} - p_{\mathrm{H_2}}\right) dt \quad \text{(E14)}$$

$$\omega_{i,\mathrm{syngas}} = \omega_0 - \int_{t_0}^{t_i} \frac{\dot{n}_{out} M_o}{m_{ox} p_{tot}} \left(2p_{\mathrm{O_2,OC}} + 2p_{\mathrm{CO_2}} + p_{\mathrm{CO}} - p_{\mathrm{H_2}}\right) dt \quad \text{(E15)}$$

where $\dot{n}_{out}$ is the molar flux of the dry flue gas and M_o is the molar mass of atom oxygen. $p_{\mathrm{O_2,OC}}$ is the outlet partial pressure of oxygen released from the oxygen carrier. $p_{\mathrm{H_2}}$ is the outlet partial pressure of hydrogen.

4 Results and Discussion-Volatiles Distributor

In this section, the results from the included papers are summarized, which highlight the main findings about the performance of the volatiles distributor with different configurations under different fluidization regimes (Part I). The details of the experimental results are presented in Paper I - III. The CFD modelling results are shown in Paper IV - V. Prior to this work, there had been no detailed experimental investigations on the VD-concept. Hence, the results presented here can be seen as proof-of-concept and provide validation of the expected benefits of the concept.

4.1 Experimental study

4.1.1 Vertical profile of the solids concentration

The vertical profile of solids concentration in the riser gives a basic overview of the different fluid-dynamical zones. Figure 10 presents the vertical solids concentration profiles with and without the VD, obtained from the pressure measurements along the height of the riser. At the bottom of the riser, a dense bed region with constant solids concentration along the height is formed, and higher fluidization velocity gives lower solids concentration. Above the dense bed region, a splash zone is formed with an exponential decay in solids concentration, caused by the strong back-mixing by means of ballistic movement of clustered particles. A transport zone with lower exponential decay above the splash zone occupies most of the riser height and has a dispersed solids flow. Higher fluidization velocity transfers more bed materials from the bottom to the transport zone. Hence, higher fluidization velocity gives a lower bottom bed and increases solids concentration in the upper part of the riser compared to lower fluidization velocity.

It was found that the variation in solids concentration from the bottom to the top of the riser in the presence of VD is generally similar to what is seen in absence of VD at low fluidization velocity as shown in Figure 10. But there is one big difference in solids concentration profile at higher fluidization velocity between with and without the VD. With VD, the solids concentration at the bottom when using a fluidization velocity of 3.7 m/s, decreases up to 300 mm height, and then increases up to 470 mm, which is exactly the top end of the VD. The presence of the VD gives a higher velocity locally, which results in approximately half of the solids concentration in this height range compared to when VD is not employed. This rise in velocity is significant because the VD occupies one third of the cross-section. In a real-world application this fraction could be smaller.

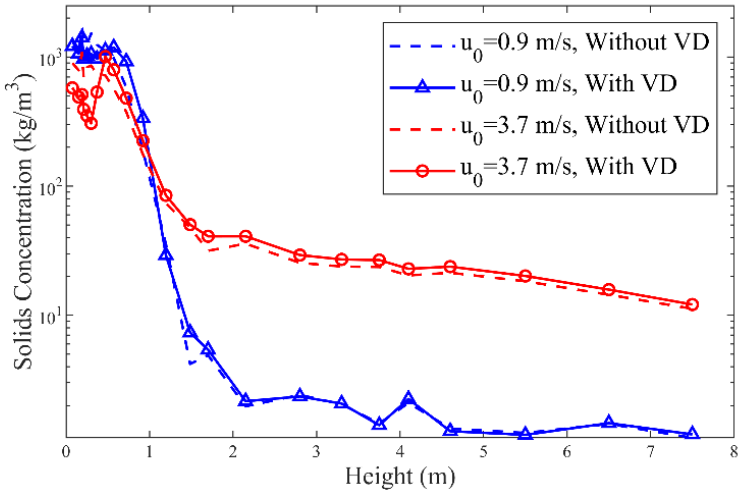

Figure 10. Solids concentration profile under different fluidization velocities in absence and presence of the VD with configuration Mode 1A.

It was also found that the solids concentration profile along the riser height remains similar when the configuration of distribution holes is changed or internal baffles are added at the bottom of the VD as shown in Figure 11. Different fluidization regimes created by different bottom air distributors under otherwise similar operational conditions, e.g. single bubble and multiple bubble regime, do not have significant effects on the solids concentration profile. The details about the fluidization regimes are discussed in the next section.

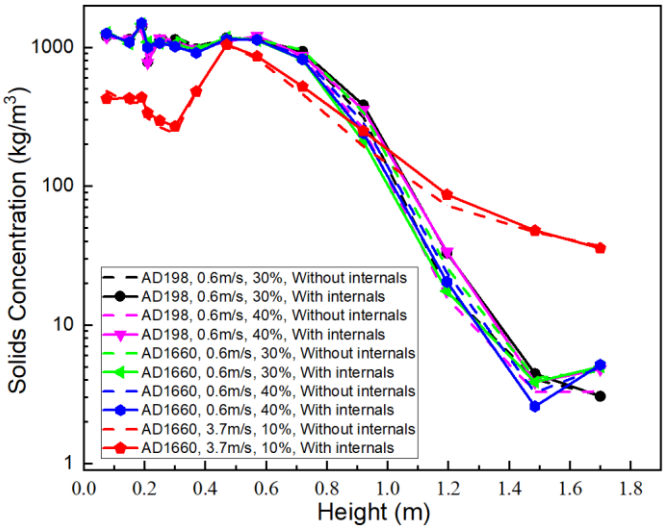

Figure 11. Solids concentration profile at the bottom of the riser with and without internal baffles (VD: Mode 1B).

4.1.2 Fluidization regime characterization

In this section, an analysis of the pressure fluctuations in the bed and in the wind box is conducted to characterize the fluidization regimes in the riser bottom.

Examples of the pressure behavior are presented in Figure 12. The pressure variations (Figure 12 a-b) show an obvious regularity, which may be caused by large single bubbles (similar to the bubble in Figure 14 a). The frequencies and amplitudes of the pressure variations measured

in the wind box and at 0.03 m are similar. This can be illustrated by power spectrum density analysis (Figure 13 a-b). Frequency spectra from the wind box and from the bed both show a sharp peak at somewhat below 1 Hz. The sharp peak in the frequency spectrum means a strong periodicity of the formation and eruption of the bubbles, which was characterized as the single bubble regime. In the single bubble regime, most of the bubbles rise up in the center of the bed and the gas flow is discontinuous because of the periodically formed and erupted bubbles. As the fluidization velocity increases from 0.9 m/s to 3.7 m/s, more irregular bubbles (Figure 12 c-d) are formed, which contain more particles compared to the bubbles at lower velocity. i.e. single bubble regime. These irregular bubbles tend to explode at the surface of the bed and are called exploding bubbles. At the higher velocity, the amplitude of the pressure fluctuation is much lower.

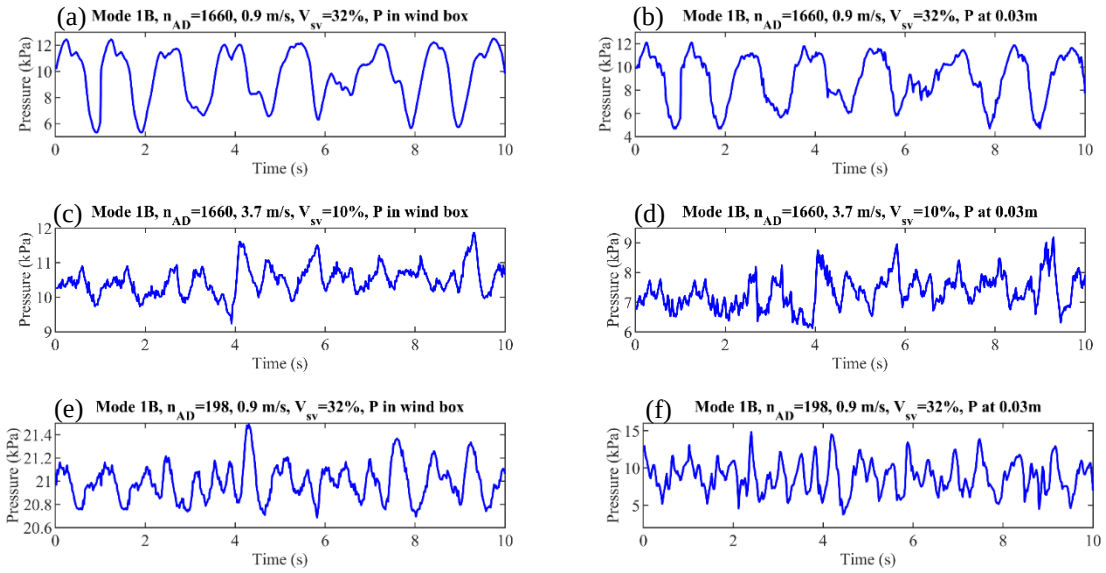

Figure 12. Pressure signal series measured in the wind box and at 0.03 m with VD Mode 1B and different ADs under different operational conditions.

When the air distributor is changed to AD198 from AD1660, the pressure variation periodicity becomes uneven and for AD198 the amplitude differs by a factor higher than 10 between the pressures in the wind box and at 0.03 m (Figure 12 e-f). The pressure vibrates in the range 20.6 ~ 21.5 kPa in the wind box and 4 ~15 kPa at 0.03 m respectively. The multiple and different sizes of bubbles (Figure 14 c) may be the reason for the uneven periodicity. The wide range of frequencies from 1 to 3 Hz in Figure 13 (f) further reflects that there are numerous bubbles with different sizes and formation frequencies in this so-called multiple bubble regime.

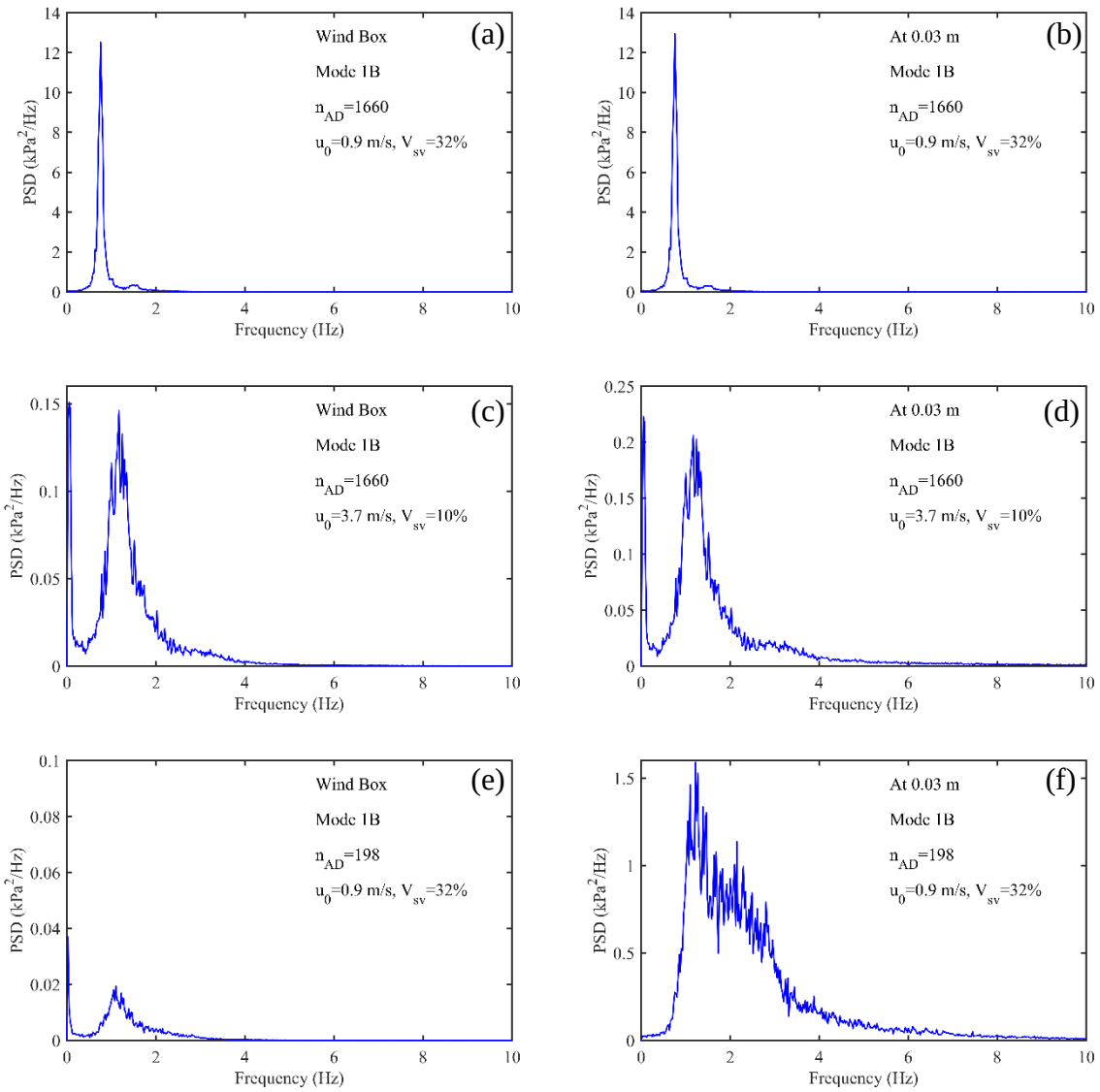

Figure 13. Power spectrum density of the pressure signal in the wind box and in the bed at 0.3 m with different ADs.

The pressure oscillating ranges in the wind box and in the bed are quite similar, i.e. around 7 kPa, under 0.9 m/s fluidization velocity with AD1660. However, they change to around 0.8 kPa and 10 kPa respectively under 0.9 m/s fluidization velocity with AD198. This is caused by the different pressure drops over the air distributor as presented in Table 4, which increases from 0.58 kPa to 11.74 kPa. When the resistance of the air distributor is low, the local fluidization air flowrate is higher where the pressure right above the distributor is low. For the AD1660 case, the air distributor pressure drop is less than 10% of that of the entire bed. The fluidization air tends to flow continuously into the bubble formed above the air distributor and lead to the large single bubbles formed in AD1660 case.

The correlation between the pressures in the wind box and at 0.03 m in the bed was analyzed based on the CORREL function in excel. The correlation coefficient is used to determine how well the pressures between the wind box and the bed are correlated. Due to the lower pressure drop across the air distributor 1660 compared to AD198, the interaction between the bed and

the air supply system is stronger, which can be indicated by the correlation coefficients in Table 4. The correlation coefficients in AD1660 case are close to 1 and those in AD198 case are close to 0, which means the pressures in Figure 12 a and b or c and d are much more correlated than those in Figure 12 e and f. The stronger interaction would be another way to distinguish the exploding bubble regime from the multiple bubble regime, since the multiple bubble regime has lower correlation between the pressure in the wind box and in the bed, and larger difference in frequency spectrum between bed and wind box, as shown in Figure 13.

It is clear that increased pressure drop over the air distributor either by high fluidization velocity or less open area of the air distributor, ensures more uniform distribution of fluidization gas, i.e. wider frequency distribution range.

Table 4. Analysis of pressures over the air distributor and the whole riser.

Parameter		AD1660		AD198	
Fluidization velocity	u_0 [m/s]	0.9	3.7	0.9	0.6
Gauge pressure in the wind box	$p_{windbox}$ [kPa]	9.50	10.43	20.77	14.89
Gauge pressure at the bottom of the riser	p_0 [kPa]	8.92	7.45	9.04	9.34
Gauge pressure at the top of the riser	p_8 [kPa]	0.27	0.89	0.29	0.17
Pressure drop over the air distributor	Δp_{AD} [kPa]	0.58	2.98	11.74	5.55
Pressure drop along the riser	Δp_{riser} [kPa]	8.65	6.56	8.75	9.16
Pressure ratio	$\Delta p_{AD}/\Delta p_{riser}$	7%	45%	134%	61%
Correlation coefficient	-	0.98	0.85	0.21	0.26

4.1.3 Fluidization situation inside the VD

4.1.3.1 Dense bed inside the VD

The transparent front plate of the riser provides the opportunity to visualize the fluidization in the riser bottom. Figure 14 illustrates the bubble flow under different operational conditions with different VDs and ADs. In the case with AD1660 and without internal baffles, there are big bubbles formed at the bottom when the fluidization velocity is low, which push particles upwards to the top of the VD. When the air distributor is changed to AD198, there are multiple and smaller bubbles formed at the bottom and the dense bed oscillates less violently than in the cases with AD1660. The dense bed surface becomes more stable by the installation of the internal baffles with the high pressure drop AD198. For the cases with internal baffles under lower fluidization velocities in Figure 14, the internal baffles break the large bubbles, and the movement of particles is reduced by the internal baffles, which helps in creating a more stable dense bed inside the VD.

When the fluidization velocity is increased to 3.7 m/s, the bed inside the VD becomes more diluted and the bed height becomes lower and more unevenly distributed in the lateral direction compared to the lower fluidization velocity cases, as shown in Figure 14 e-f. Note that the inner wall of the VD is also made in perplex, so in the photos with low bed levels, the fluidization behavior of the bed behind, i.e. outside of the VD, can be also seen. There is very little dense bed observed in the case with internal baffles at high fluidization velocity.

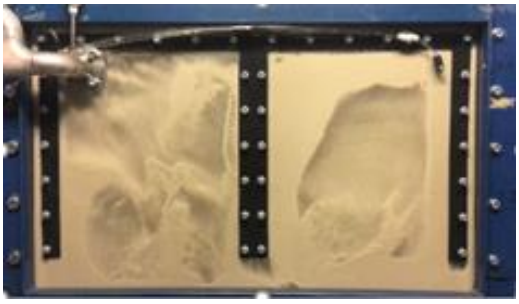

(a) 0.6 m/s, V_{sv}~30%, VD Mode 1B **without** Internal baffles, AD 1660

(b) 0.6 m/s, V_{sv}~30%, VD Mode 1B **with** Internal baffles, AD 1660

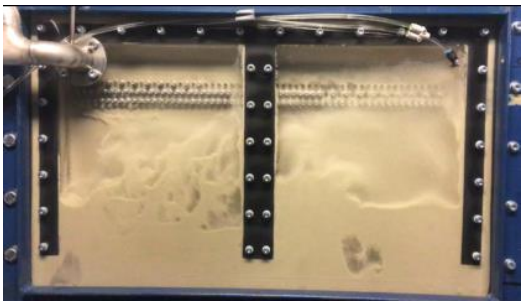

(c) 0.6 m/s, V_{sv}~30%, VD Mode 1B without Internal baffles, AD 198

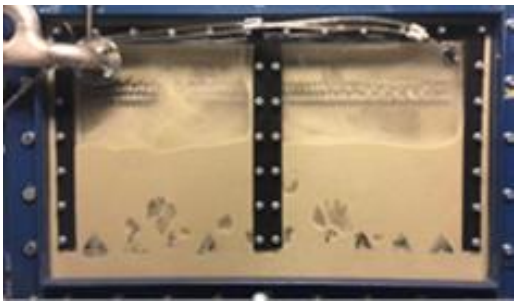

(d) 0.6 m/s, V_{sv}~30%, VD Mode 1B **with** Internal baffles, AD 198

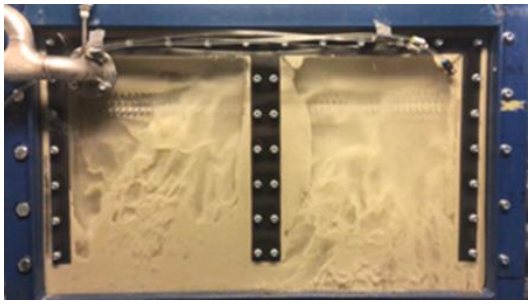

(e) 3.7 m/s, V_{sv}~10%, VD Mode 1B **without** Internal baffles, AD 1660

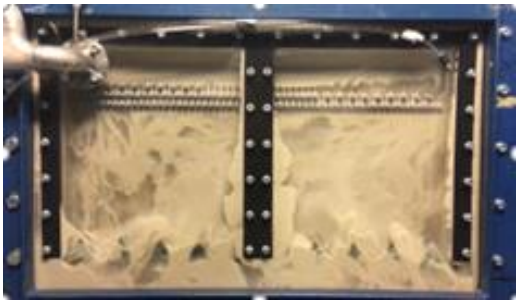

(f) 3.7 m/s, V_{sv}~10%, VD Mode 1B **with** Internal baffles, AD 1660

Figure 14. Captured photos of the bottom riser with different VDs and ADs under different experimental conditions.

4.1.3.2 Pressure drop over the VD

Figure 15 shows the pressures inside and outside the VD under different fluidization regimes. In general, the average pressure outside the VD is always lower than that inside the VD, which means the dense bed surface inside the VD is always below the level of the distribution holes of the VD. The standard deviation of the pressure outside the VD decreases significantly when the fluidization regime goes from single bubble to multiple bubble regime, which might be caused by the much smaller bubbles in multiple bubble regime compared to the single bubble regime. However, the standard deviation of the pressure difference over the holes, i.e. P_{in}-P_{out}, in the single bubble regime is lower than that in the multiple bubble regime, which is associated with more correlated pressure fluctuations between inside and outside the VD in the single bubble regime, compared to the multiple bubble regime.

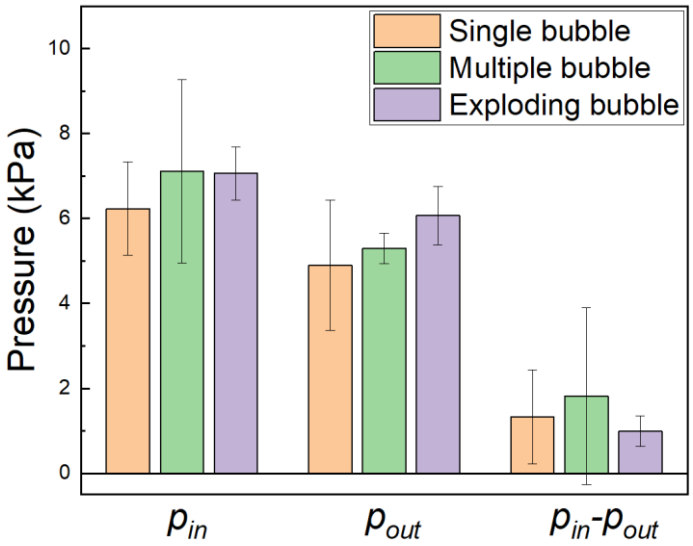

Figure 15. Average pressure and standard deviation of the pressures and pressure drops inside and outside of the VD at the level of the distribution holes under different fluidization regimes.

As Figure 16 shows, the change of the configuration of the holes has no obvious influence on the standard deviations of the pressures. However, as a consequence of doubling the open area of the VD distribution holes, i.e. from Mode 1B to Mode 2B, the pressure difference, i.e. P_{in}-P_{out}, becomes smaller. What's more, the average pressure drop under similar operational conditions with AD1660 doesn't change very much when the VD is changed from Mode 2B to Mode 2A.

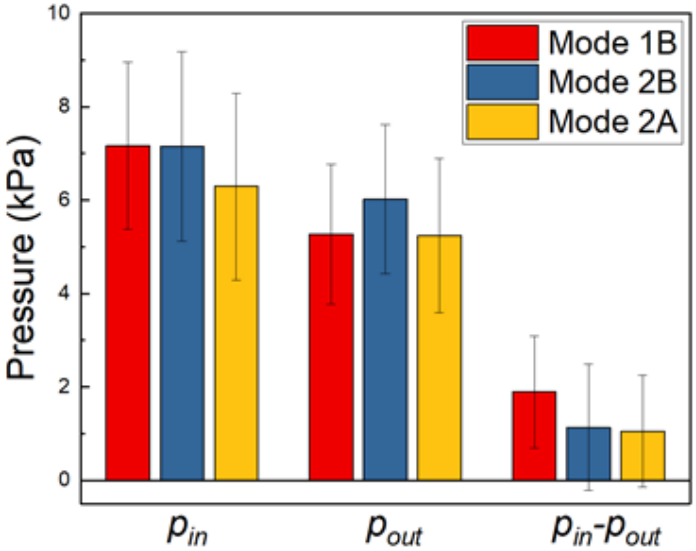

Figure 16. Average pressure and standard deviation of the pressures and pressure drops inside and outside of the VD at the level of the distribution holes with different configurations of distribution holes.

Figure 17 shows the influence of internal baffles on the pressure drops over the distribution holes. Similar decrease of the pressure drop when baffles are added, is found in both the single bubble and multiple bubble regimes, which means less gas passes through the distribution holes with baffles. However, in the exploding bubble regime similar pressure drops over the distribution holes are found with and without internal baffles.

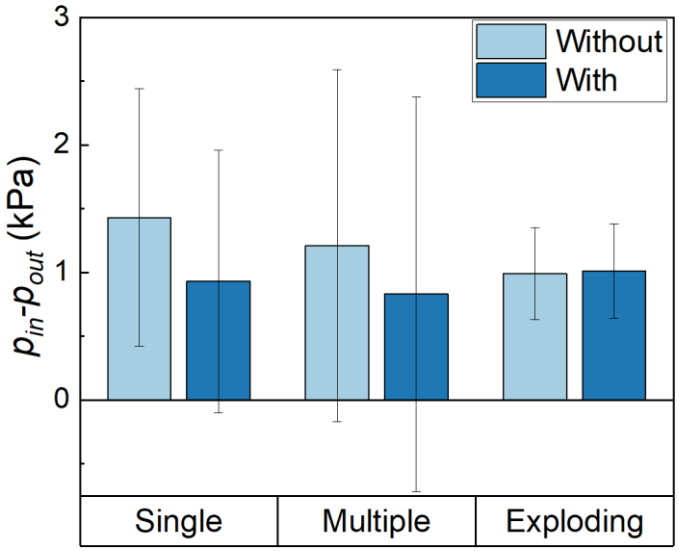

Figure 17. Influence of internal baffles on the average and standard deviation of pressure drop over the distribution holes of the VD under different fluidization regimes. ('Without and with' refer to 'with and without internal baffles')

Less bottom air takes the path through the VD and its distribution holes and more bed material stays inside the VD with the internal baffles present, which gives a higher bed level inside the VD in both multiple and single bubble regimes as shown in Table 5. However, there is no influence of internal baffles on the dense bed height in the exploding bubble regime. Furthermore, an increased volatiles flow causes higher pressure drop over the distribution holes and lower dense bed level inside the VD.

Table 5 Influence on the dense bed height inside the volatiles distributor.

Air distributor			AD198				AD1660					
Fluidization velocity	u_0	m/s	0.6				0.6				3.7	
Volatiles percentage	$\frac{V_{sv}}{V_{pa}+V_{sv}}$		30%		42%		30%-31%		42%		10%	
Fluidization regime			Multiple bubble				Single bubble				Exploding bubble	
Internal baffles			No baffles	Baffles	No baffles	Baffles	No baffles	Baffles	No baffles	Baffles	No baffles	Baffles
Pressure drop over the VD	$p_{in} - p_{out}$	kPa	1.21	0.83	1.73	1.29	1.43	0.93	1.95	1.37	0.99	1.01
Pressure gradient	dp/dh	kPa/m	10.66	10.56	10.39	10.38	10.73	10.30	10.32	10.13	4.24	4.16
Dense bed height inside VD	h_b	m	0.15	0.18	0.09	0.14	0.13	0.17	0.07	0.12	0.03	0.02

4.1.3.3 Dilution of volatiles inside the VD

Table 6 presents the calculation results of the simulated volatiles dilution inside the VD according to the orifice discharge coefficient equation [83]. Dilution of volatiles inside the VD was analyzed based on the dilution factors i.e. V_{ba}/V_{sv} and c_{vd}/c_{sv}.

The volatiles injected into the VD are diluted by the bottom air flowing into the VD. When internal baffles are installed in the VD, as shown in Table 6 there is less bottom air flowing into the VD and the dilution of the injected simulated volatiles is smaller, especially in the single and multiple bubble regime. The lower dilution results in more even distribution of the volatiles. However, there is no big difference in the volatiles dilution inside the VD in the exploding bubble regime, i.e. the degree of bottom air flow coming into the VD before and after the installation of the internal baffles is largely the same.

Table 6. Volatiles dilution inside the VD estimated based on orifice discharge coefficient.

Air distributor	Fluidization velocity	Fluidization regime	Volatiles percentage	Internal Baffle	$p_{in} - p_{out}$	Gas velocity through orifices	Gas flow from the bottom of VD	Fluidization velocity inside VD	CO_2 concentration inside VD	Dilution Factors	
					kPa	$v_{orifice}$ m/s	V_{ba} m_n^3/h	u_{VD} m/s	c_{vd} ppm	$\frac{V_{ba}}{V_{sv}}$	$\frac{c_{vd}}{c_{sv}}$
AD198	0.6 m/s	Multiple bubble	30%	No	1.21	41.52	100	1.17	4934	1.43	0.44
				Yes	0.83	34.44	70	0.82	8267	0.98	0.76
			40%	No	1.73	49.61	81	0.95	10365	0.66	0.70
				Yes	1.29	42.91	53	0.62	10327	0.43	0.92
AD1660	0.6 m/s	Single bubble	30%	No	1.43	45.20	115	1.34	5829	1.62	0.53
				Yes	0.93	36.42	76	0.89	8421	1.03	0.79
			40%	No	1.95	52.73	98	1.15	7558	0.84	0.67
				Yes	1.37	44.13	57	0.67	9213	0.46	0.90
	3.7 m/s	Exploding bubble	10%	No	0.99	37.49	43	0.50	9123	0.39	0.75
				Yes	1.01	37.92	45	0.53	8578	0.41	0.79

4.1.4 Horizontal distribution of simulated volatiles

Figure 18 presents the CO_2 ratios at different horizontal positions with VDs of different configurations in the single bubble regime. Generally, the cases with VD have a more even horizontal distribution compared to the experiments without VD. Mode 1B and Mode 2B give a more uniform horizontal distribution at the higher level compared to Mode 1A and 2A. Since the simulated volatiles are injected from the left side, more simulated volatiles would be distributed through the holes near the injection port when the distribution holes are evenly distributed, i.e. Mode 1A and 2A. This is because the gas going through the holes far from the volatiles inlet is more diluted with bottom air entering the VD from below. When the configuration of the distribution holes is uneven, i.e. Mode 1B and Mode 2B, the injected simulated volatiles are forced to flow to the right-hand side giving a more even distribution. Hence, the modified configurations of the VD are helpful in providing a more uniform distribution of the volatiles. There are mainly two sources of the simulated volatiles at the lower level in the riser, i.e. leakage from the bottom of the VD and back mixing near the walls. As Figure 18 shows, there is a large decrease in the CO_2 ratio at LSV1 from Mode 1B to Mode 2B, even though the CO_2 ratio at HSV1 is similar, which indicates that a larger open area of the distribution holes of Mode 2B reduces the bottom leakage of the VD dramatically.

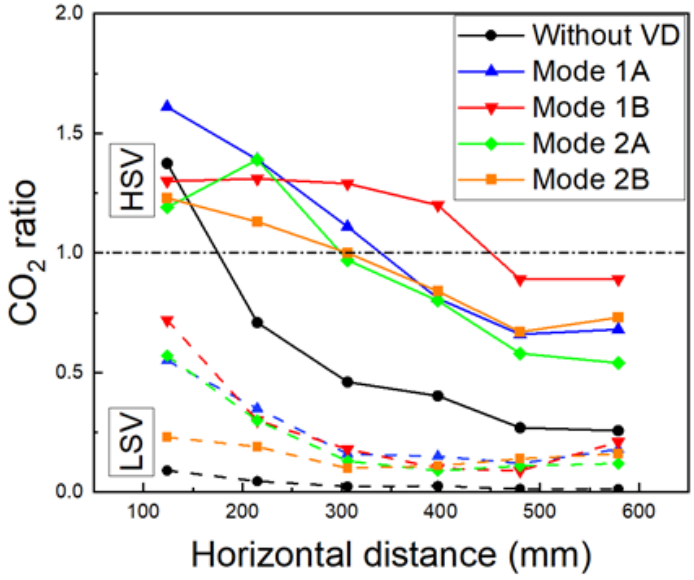

Figure 18. The distribution of volatiles in the horizontal direction from the left to the right side of the riser, with different configurations in single bubble regime. (See Figure 5 for the details of HSV/LSV1-6.)

A comparison between the cases without VD, with VD and with VD equipped with internal baffles in multiple and exploding bubble regime, is shown in Figure 19. It clearly illustrates that the horizontal distribution of volatiles is significantly improved by the VD equipped with internal baffles, especially in multiple bubble regime. The CO_2 ratios keep close to 1 from HSV2 to HSV6 with internal baffles in multiple bubble regime. In the exploding bubble regime, the CO_2 ratio is lowered slightly at the left side and raised at the right side, when using baffles. Thus, the internal baffles fulfil the objective of the uneven holes arrangement, which is to move the volatile gases to the right, i.e. away from the injection port.

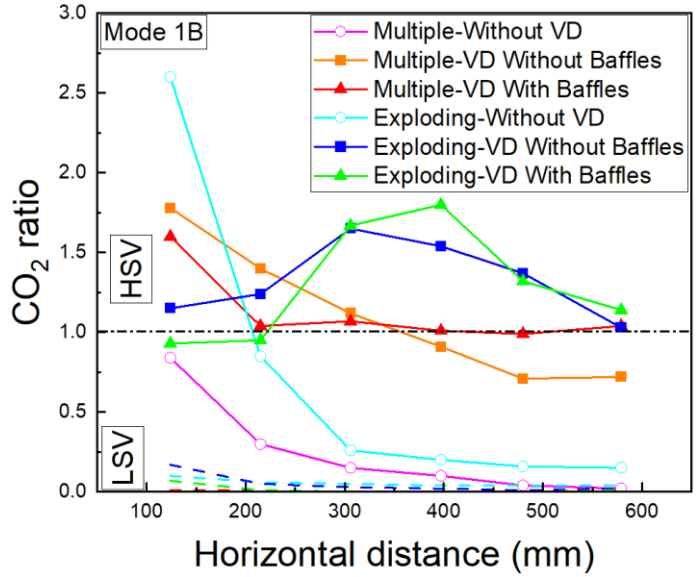

Figure 19. The distribution of volatiles in the horizontal direction from the left to the right side of the riser without VD, with VD and with VD equipped with internal baffles, in multiple and exploding bubble regimes. (See Figure 5 for the details of HSV/LSV1-6.)

4.1.5 Overall performance of the VD

Table 7 summarizes the results of the experiments with different VD configurations. The standard deviation of the CO_2 ratios at different horizontal positions, together with the relative standard deviation and the ratio between the highest and lowest concentration, gives an overall evaluation on the uniformity of the horizontal distribution of the simulated volatiles by different VDs.

From the results, it is evident that the VD in Mode 1B and Mode 2B has better overall performances with respect to the horizontal distribution of gas. Furthermore, the SD, RSD and H/L are smallest for the exploding bubble regime (EB), the largest for the multiple bubble regime (MB) and in the middle for the single bubble regime (SB).

Table 7. Statistical evaluation on the performance of different VDs under different experimental conditions. SD: standard deviation, RSD: relative standard deviation, H/L: highest/lowest concentration.

Air distributor	VD holes arrangement	Fluidization velocity/Regime u_0 $[m/s]$	Simulated volatiles percentage V_{sv}	Open area of the VD A $[m^2]$	Average CO_2 ratio	*SD*	*RSD*	*H/L*
AD1660	Mode 1A	0.9/SB	7%	1.138×10^{-3}	1.21	0.57	47%	3.5
			30%		1.01	0.36	36%	2.51
		3.7/EB	10%		1.07	0.25	23%	1.86
	Mode 1B	0.9/SB	10%		1.44	0.55	38%	2.69
			32%		1.14	0.18	16%	1.48
		3.7/EB	10%		1.31	0.2	16%	1.58
	Mode 2A	0.9/SB	11%	2.276×10^{-3}	1.25	0.73	59%	4.86
			32%		1.01	0.48	48%	3.64
		3.7/EB	10%		1.3	0.59	45%	4.81
	Mode 2B	0.9/SB	11%		0.95	0.28	29%	2.14
			32%		0.92	0.21	22%	1.85
		3.7/EB	10%		1.14	0.31	28%	2.13
AD198	Mode 1B	0.9/MB	32%	1.138×10^{-3}	1.16	0.42	36%	2.56
		0.6/MB	30%		1.12	0.39	35%	2.52
			42%		1.02	0.29	28%	2.2
	Mode 2B	0.9/MB	33%	2.276×10^{-3}	0.95	0.39	42%	2.95
		0.6/MB	30%		0.97	0.53	55%	4.38
			43%		0.94	0.36	38%	2.72

Table 8 shows the overall performance of the VD with and without internal baffles under different operational conditions. In the multiple and single bubble regimes, the standard deviation, and relative standard deviation of the CO_2 ratios, together with the highest/lowest concentration, are much lower in the cases with internal baffles.

In the exploding bubble regime, the standard deviation, the relative standard deviation and the highest/lowest concentration of CO_2 ratios are higher in the case with internal baffles compared to the case without baffles. This can be explained by lower CO_2 ratios at HSV1 and HSV2 and higher ones at HSV4 and HSV5 in the case with internal baffles compared to the case without baffles, which means that the installation of the internal baffles help the VD push more simulated volatiles to be distributed from the side further away from the simulated volatiles injection port. Thus, the internal baffles do not improve the distribution of the simulated

volatiles in the exploding bubble regime, but it does amplify the movement of volatiles away from the injection port, which is the purpose of the uneven hole distribution. This means that the internal baffles facilitate the control over the distribution, which is an important point considering the application in longer VD arms.

Table 8. General performance of the VD with and without internal baffles under different operational conditions.

Air distributor	Fluidization velocity	Fluidization regime	Simulated volatiles percentage	Average CO_2 ratio		*SD*		*RSD*		*H/L*	
	m/s			No baffles	Baffles	No baffles	Baffles	No baffles	Baffles	No baffles	Baffles
AD198	0.6	Multiple bubble	30%	1.11	1.13	0.38	0.21	0.35	0.19	2.52	1.61
			42%	1.00	1.05	0.29	0.12	0.29	0.11	2.20	1.39
AD1660		Single bubble	30-31%	1.20	1.22	0.41	0.19	0.34	0.16	2.30	1.55
			42%	1.06	1.21	0.23	0.18	0.22	0.15	1.80	1.51
	3.7	Exploding bubble	10%	1.33	1.30	0.21	0.34	0.16	0.26	1.60	1.95

It is shown in Table 8 that the standard deviation, relative standard deviation, and the highest/lowest concentration are much lower when the volatiles percentage increases in the single and multiple bubble regime for the reference cases without internal baffles. However, these values remain similar in the cases with internal baffles, especially in the single bubble regime, which means that once the internal baffles are installed, the flowrate of simulated volatiles would not have a big impact on the horizontal distribution by the VD.

Generally, the VDs with less open area or internal baffles at bottom give a better horizontal tracer distribution across the cross section by comparing the values of SD, RSD and c_H/c_Lin Table 7 and Table 8.

4.2 CFD modelling

In the first part of this section, the CFD modelling results of the fluidized bed without the VD using three drag models were compared with experimental data to select the most suitable model. The selected model was then employed when studying the implementation of the VD using configuration Mode 1A, which was subsequently compared to corresponding experimental data for further validation. The second part of this section examines the impact of the VD configured as Mode 1A on the hydrodynamics of the fluidized bed. Finally, the third part presents the predicted performance of the VD with different configurations, including Mode 1A, Mode 1B, Mode 2A, and Mode 2B.

4.2.1 Model validation and selection

4.2.1.1 Fluidized bed without VD

The comparison between experimental pressure data and predicted ones along riser height by the three drag models under different operating conditions is shown in Figure 20. At low U_g, i.e., 0.94 m/s and 2.04 m/s, pressure profiles predicted by the three drag models, i.e. Gidaspow model, filtered model, and two-step EMMS/bubbling model, are all in good agreement with the experimental data. With the increase of U_g, i.e., 3.09 m/s and 4.13 m/s, the two-step EMMS/bubbling model shows the best predictions.

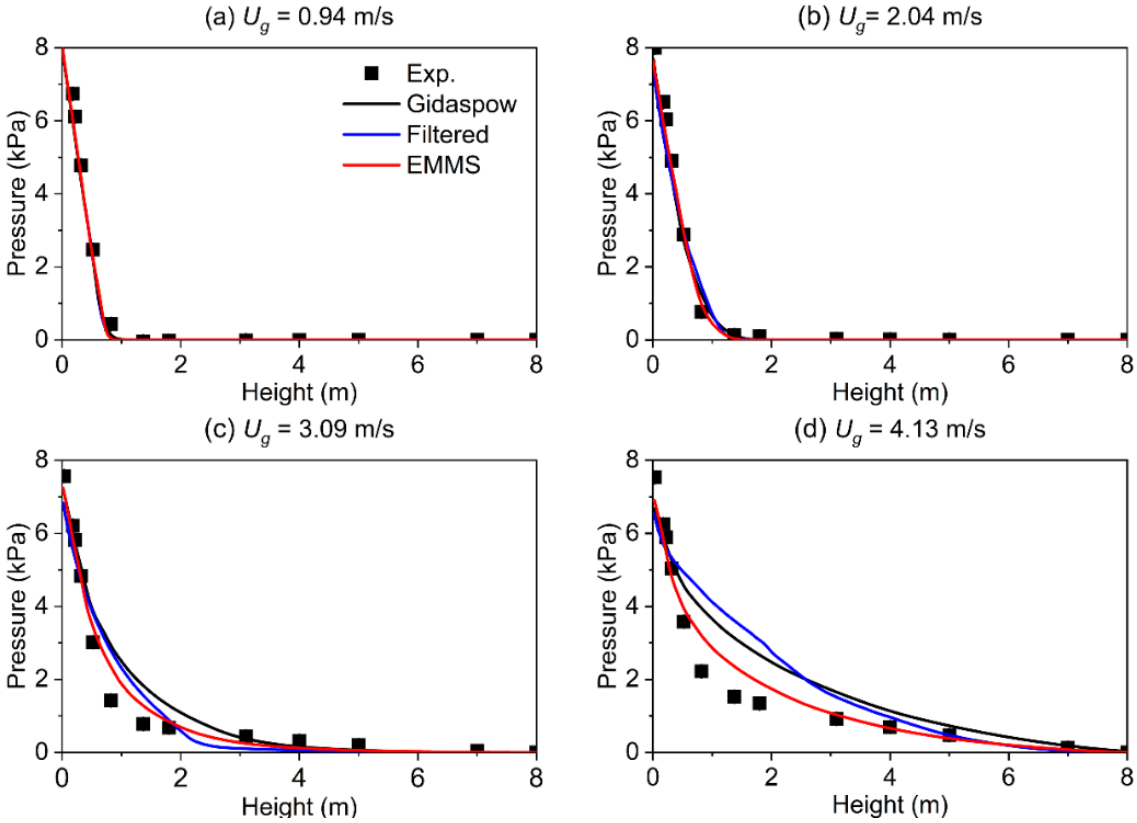

Figure 20. Comparison of predicted axial pressure profiles without VD by using the three drag models with experimental data under different U_g ((a) U_g = 0.94 m/s, (b) U_g = 2.04 m/s, (c) U_g = 3.09 m/s, (d) U_g = 4.13 m/s).

Lateral profiles of CO_2 concentration ratios at two different heights (HSV and LSV) predicted by the three drag models with experimental results under various operating conditions are shown in Figure 21. All drag models give the same tendency of experiments, i.e., higher concentration ratio at left side for both LSV and HSV. At the LSV level, lateral profiles of CO_2 concentration ratio predicted by all drag models are generally in good agreement with the experimental data.

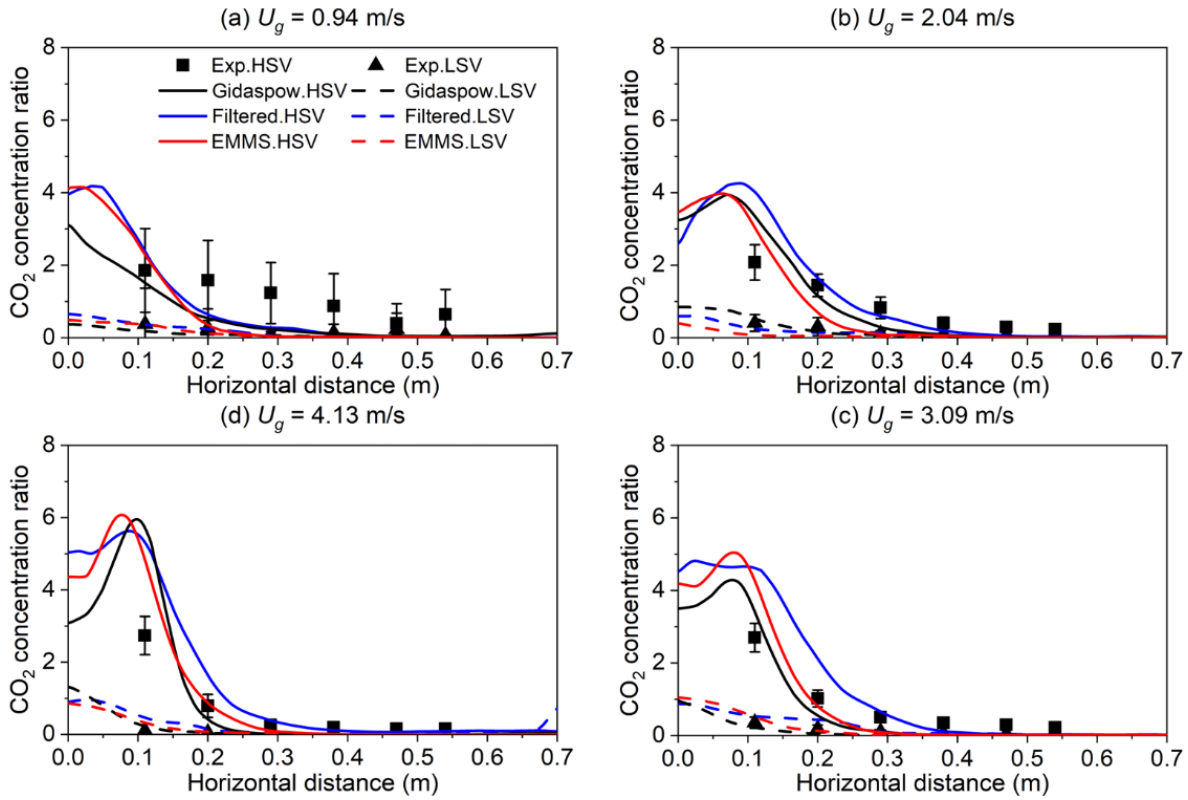

Figure 21. Comparison of predicted lateral profiles of CO_2 concentration ratio at two different heights of the riser bottom (HSV: 0.483 m, LSV: 0.138 m) using the three drag models with experimental data under different U_g ((a) U_g = 0.94 m/s, (b) U_g = 2.04 m/s, (c) U_g = 3.09 m/s, (d) U_g = 4.13 m/s) without VD.

Overall, all the three drag models have similar performance in the simulation of fluidized bed with lower U_g, i.e., bubbling fluidization regime, while the two-step EMMS/bubbling model gives the most reasonable results at U_g = 3.09 m/s, i.e., the transition regime from bubbling to turbulent, and U_g = 4.13 m/s, i.e., the turbulent regime. Therefore, the two-step EMMS/bubbling model is further used to evaluate its performance in CFD modeling of the fluidized bed with VD.

4.2.1.2 Fluidized bed with VD

Figure 22 shows both predicted and measured lateral profiles of CO_2 concentration ratio at two different heights, HSV and LSV, with the VD inserted in the fluidized bed using various operating conditions. For lower superficial gas velocities, lateral profiles of the CO_2 concentration ratio predicted by the two-step EMMS/bubbling drag model are in good agreement with the experimental data. At higher superficial gas velocity, predicted CO_2 concentration ratios are higher than the experimental ones at the left-hand side. With increased distance from the injection point, CO_2 concentration ratios predicted by CFD decrease more rapidly than the experimental ones and then show an increase in the right wall region. A possible cause for this discrepancy is that the standard k-ε turbulence model can give a good prediction at low turbulent intensity, while a more detailed turbulent model is required for high superficial gas velocity. Another more likely explanation to the discrepancy between CFD

simulations and experiments at higher superficial gas velocities is that the measured gas concentrations represent the average concentration at a given position, rather than the average concentration of the entire flow. At higher superficial gas velocities, the fluidization gas from the bottom containing no CO_2 could bypass the bed at a higher velocity. As a result, the suction tube for the gas analyzer will sample less from these bypass flows, leading to higher measured CO_2 concentrations. But both CFD simulations and experiments show that the simulated volatiles can be distributed from the left-hand side to the right side, i.e., the side with injection port, with the help of VD, as compared to the case without VD as shown in Figure 21.

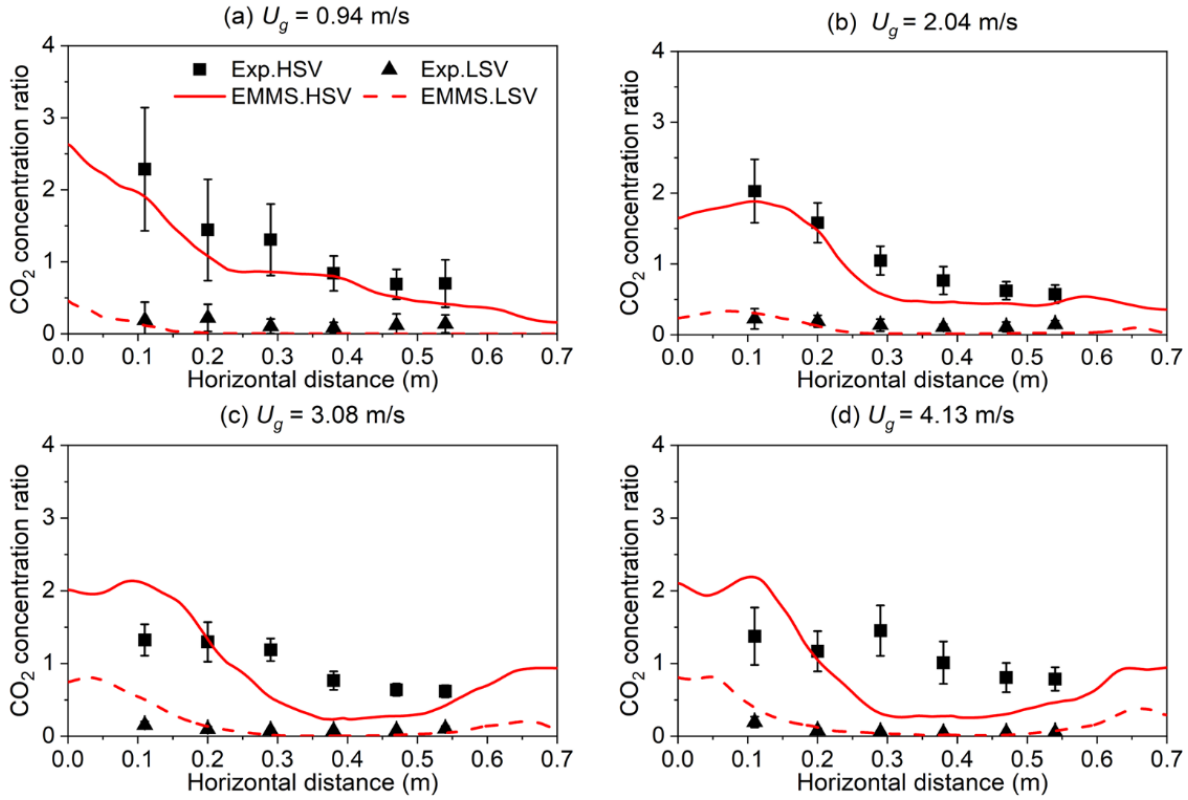

Figure 22. Comparison of predicted lateral profiles of CO_2 concentration ratio at two different heights of the fluidized bed bottom (HSV: 0.483 m, LSV: 0.138 m) using the two-step EMMS/bubbling model with experimental data under different superficial gas velocity ((a) V_{sv}= 19 Nm^3/h, (b) V_{sv}= 65 Nm^3/h, (c) V_{sv}= 92 Nm^3/h, (d) V_{sv}= 112 Nm^3/h, while flow rate of simulated volatiles were kept as around 10% of the primary air) with VD.

Figure 23 compares predicted profiles of vertical pressure and horizontal CO_2 concentration with experimental data under varying flow rate of simulated volatiles (V_{sv} is 19, 61, 102 Nm^3/h). The velocity of the primary air is kept constant at 0.94 m/s. The results show that CFD predictions are quantitatively in good agreement with experimental data. This suggests that the two-step EMMS/bubbling mode could give reasonable predictions of hydrodynamics and mass transfer of the experimental setup equipped with VD operated under various conditions, in particular at low superficial gas velocity.

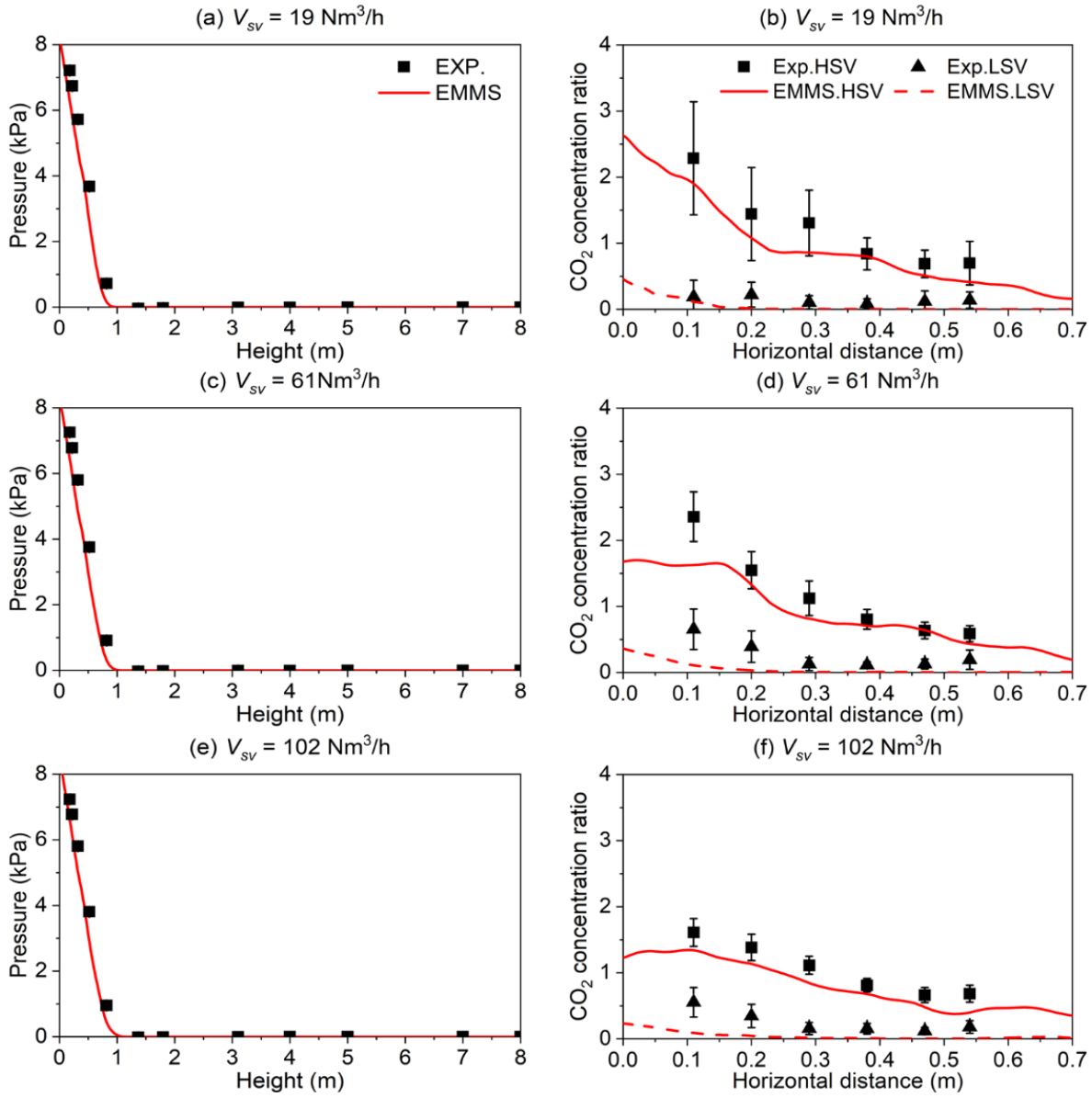

Figure 23. Comparison of predicted axial pressure profiles ((a), (c), and (e)) and lateral profiles of CO_2 concentration ratio ((b), (d), and (f)) at two different heights (HSV: 0.483 m, LSV: 0.138 m) using the two-step EMMS/bubbling drag model and the experimental data with varying flow rate of the simulated volatile (V_{sv} = 19, 61, 102 Nm^3/h).

Overall, CFD simulations with the two-step EMMS/bubbling model of the fluidized bed with and without VD are validated with experimental data from two aspects, i.e., profiles of axial pressure and lateral CO_2 concentration ratio. It means the two-step EMMS/bubbling model is suitable to simulate the experimental setup and could give reasonable predictions of hydrodynamics and mass transfer under various operating conditions with or without VD. The results predicted by the two-step EMMS/bubbling model will be further used to evaluate the effects of VD on hydrodynamic behavior of the fluidized bed.

4.2.2 Effects of the VD on hydrodynamic behaviors

4.2.2.1 Solids volume fraction

Figure 24 compares instantaneous (a) and time-averaged (b) solids volume fraction of the fluidized bed without (left) and with (right) the VD from the front view under various operating conditions. For the case of U_g = 0.94 m/s, bed expansions without and with the VD are almost the same. A dilute region with low solid concentration near injection port of the simulated volatiles is observed for the case without the VD. When simulated volatiles are injected into the VD, the top region of the VD is free from solid particles due to pressure drop over distribution holes of the VD. When increasing the superficial gas velocity to 2.04 m/s and at the same time increasing flow rate of simulated volatiles proportionally, bed material inside the VD is squeezed outside due to higher pressure drop over the distribution holes, and consequently, bed expansion with the VD is slightly higher than the case without the VD. The upper region of the VD is free from particles, when superficial gas velocities are 3.09 m/s and 4.13 m/s, similar to the case at U_g = 2.04 m/s. Those findings are also consistent with axial pressure profiles of the VD region shown in Fig. S10 in the Supplementary Materials of Paper IV.

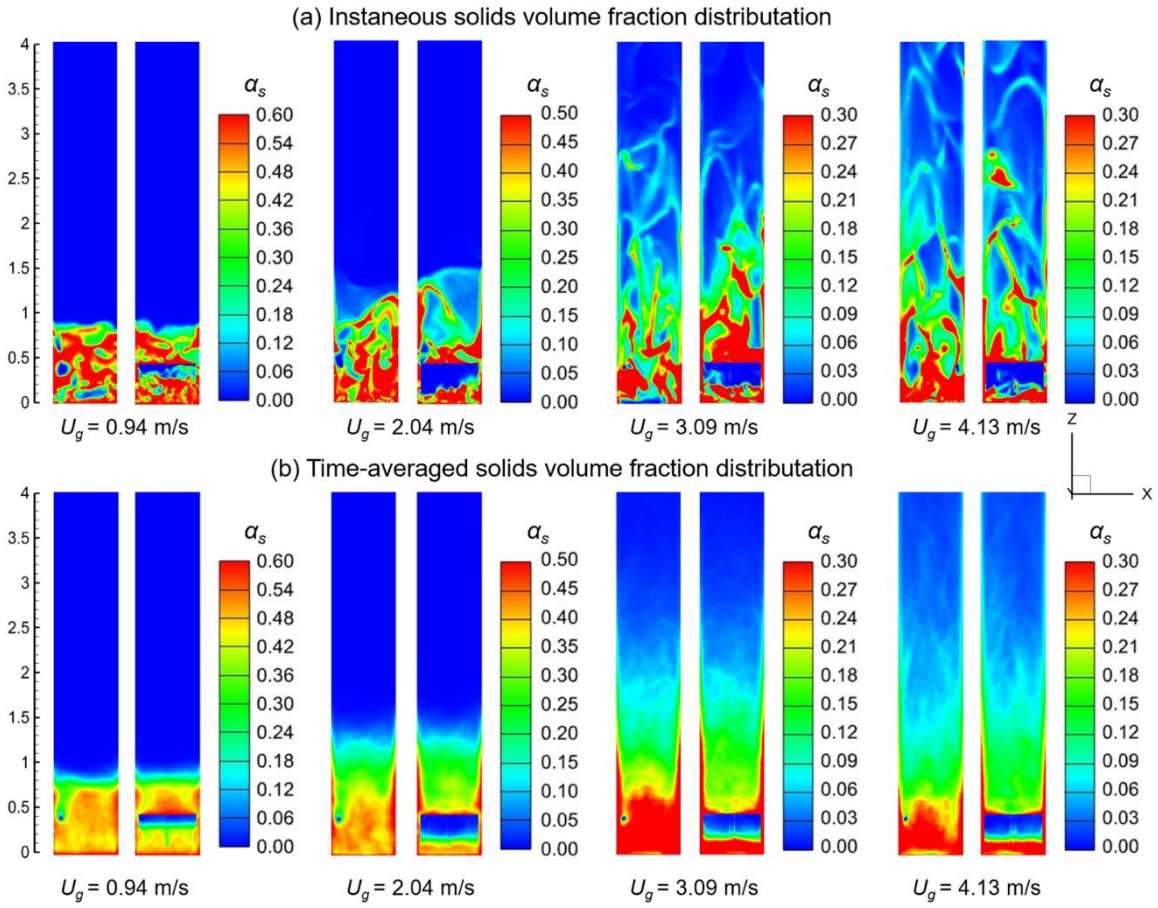

Figure 24. Instantaneous (a) and time-averaged (b) solids volume fraction of the fluidized bed without (left) and with (right) the VD from the front view under various operating conditions ((a) U_g = 0.94 m/s, (b) U_g = 2.04 m/s, (c) U_g = 3.09 m/s, (d) U_g = 4.13 m/s).

To provide more details of the effects of the VD on distribution of solids at the bottom of the fluidized bed, Figure 25 displays time-averaged solids volume fraction in the YZ plane at X=0.08 m, 0.35 m, and 0.55 m for the cases without and with the VD. Contour plots of the YZ plane show the bottom section of the fluidized bed, i.e., from 0 to 0.6 m high, where the VD has significant effects on primary air flow. For the fluidized bed without the VD, solids volume fraction is relatively constant along the height at bottom section for all operating conditions. However, the solids volume fraction decreases from 0.4 to 0.2 when the superficial gas velocity increases from 0.94 m/s to 4.13 m/s. For the fluidized bed with VD, the solids volume fraction outside the VD is slightly lower than that of the fluidized bed without VD at heights smaller than 0.4 m, because of local increase of gas velocity. When the height is more than 0.4 m, the solids volume fraction increases slightly and then decreases to be similar to that of the fluidized bed without the VD, as cross-sectional area outside VD gets back to normal cross-section of the fluidized bed. The solids volume fraction inside the VD decreases with height under all investigated operating conditions. The height of the dense phase inside the VD differs among the four different cases, especially when U_g = 0.94 m/s. The contour plots also show that injection of simulated volatiles only has limited effects on distribution of solids volume fraction near the injection port, i.e., X = 0.08 m, in the cases without the VD, while other positions, e.g., 0.35 m and 0.55 m, still maintain the typical ‘core-annulus’ flow structure in the fluidized bed. With the VD, part of solids is also recycled back at around 0.4 m to 0.5 m height as cross-sectional area is enlarged, thereby higher solids volume fraction is observed in this region, which is good for mixing between simulated volatiles and solid particles.

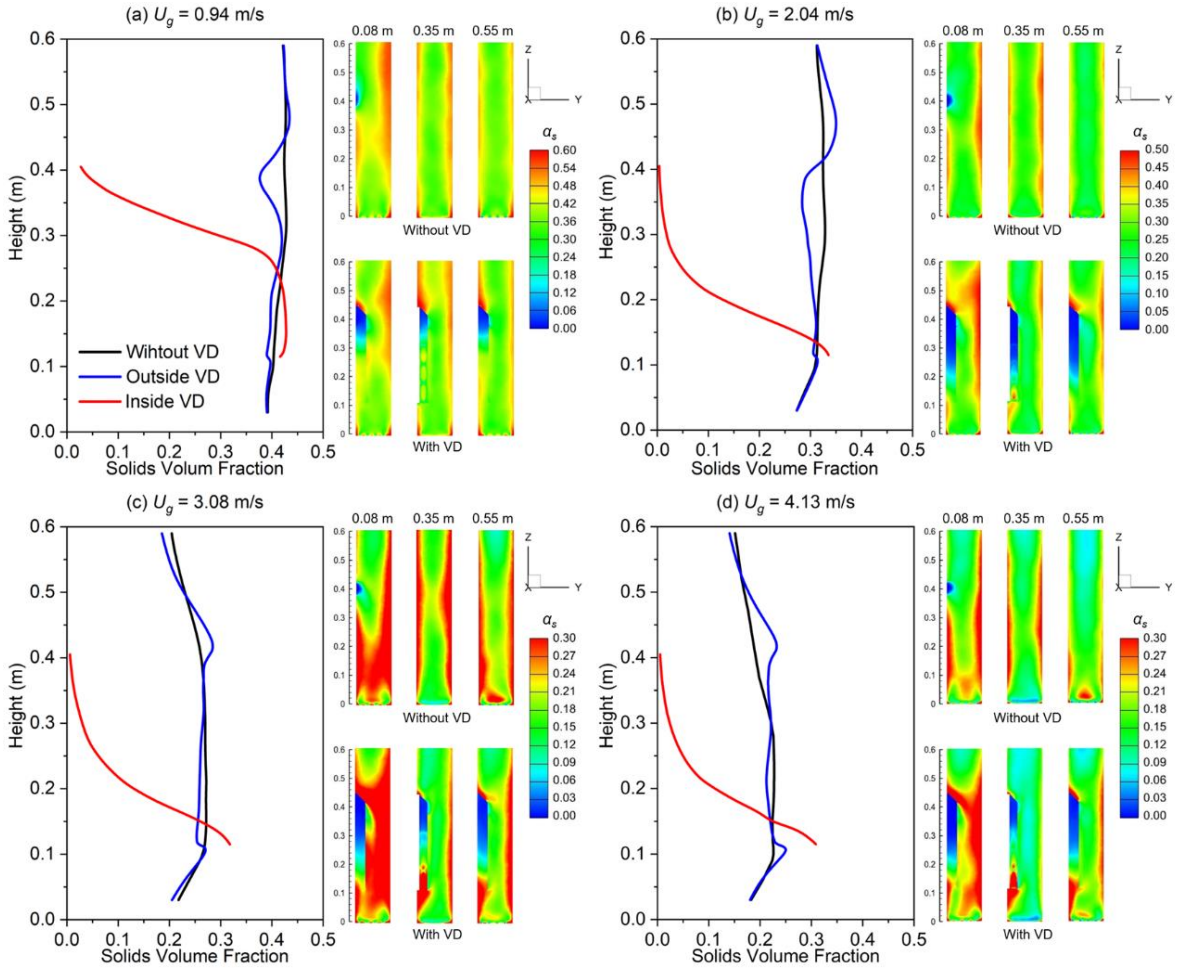

Figure 25. Axial profiles of time-averaged solids volume fraction along with their contour plots of YZ plane at X=0.08 m, 0.35 m, and 0.55 m for the cases without and with the VD under various operating conditions ((a) U_g = 0.94 m/s, (b) U_g = 2.04 m/s, (c) U_g = 3.09 m/s, (d) U_g = 4.13 m/s).

4.2.2.2 Distribution of CO_2 concentration

As CO_2 is used as tracer gas in the experiments, its distribution can reflect mixing of simulated volatiles with primary air and solid particles. Figure 26 shows time-averaged CO_2 concentration in the XZ plane (left) and XY plane (right) at four heights (right) without and with the VD at different fluidization velocities. For the fluidized bed without VD, simulated volatiles are not well mixed with primary air at the bottom section when U_g = 0.94 m/s. With increased superficial gas velocity, mixing between simulated volatiles and primary air becomes poorer. But with the VD, simulated volatiles are reasonably well mixed with primary air after distribution of the VD.

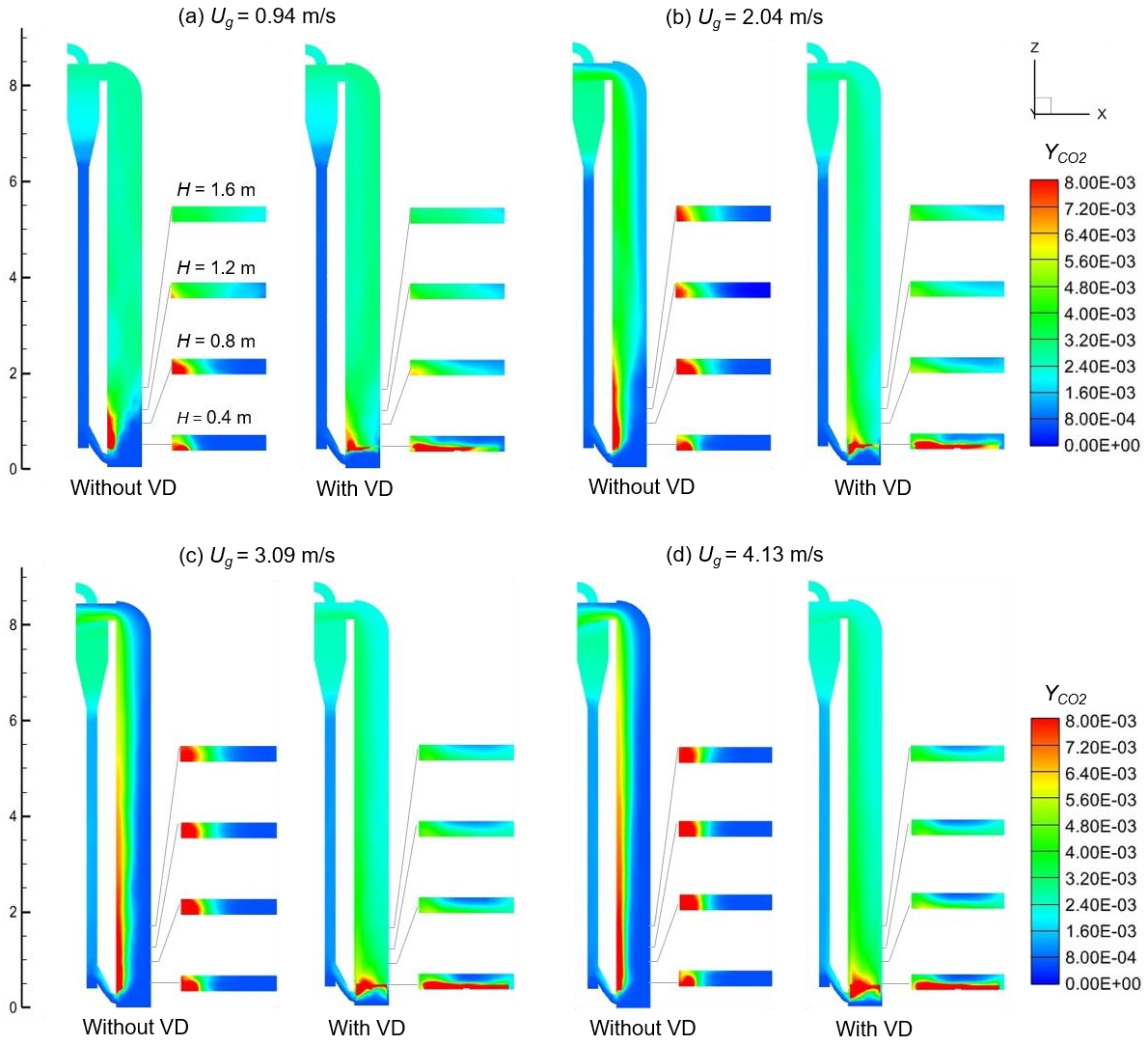

Figure 26. Comparison of contour plots of time-averaged CO_2 concentration in the fluidized bed without and with the VD under various operating conditions ((a) U_g = 0.94 m/s, (b) U_g = 2.04 m/s, (c) U_g = 3.09 m/s, (d) U_g = 4.13 m/s).

To further evaluate the effects of the VD on the mixing between simulated volatiles and primary air at different heights, Figure 27 shows comparison of lateral profiles of CO_2 concentration ratio at two selected heights, i.e., 0.4 m and 0.8 m, for the fluidized bed without and with the VD under various operating condition. A height of 0.4 m is selected because it is the same as the injection port of simulated volatiles. Height of 0.8 m is selected because this height better reflects the effects of the VD on the horizontal distribution. It is evident that the local plume of simulated volatiles near the injection port is distributed more evenly over the cross-section by the VD. At 0.8 m, CO_2 ratio varies around 1, indicating that simulated volatiles are reasonably well mixed with primary air as well as solid particles. Therefore, the VD is indeed expected to improve combustion efficiency of volatiles in the fluidized-bed system.

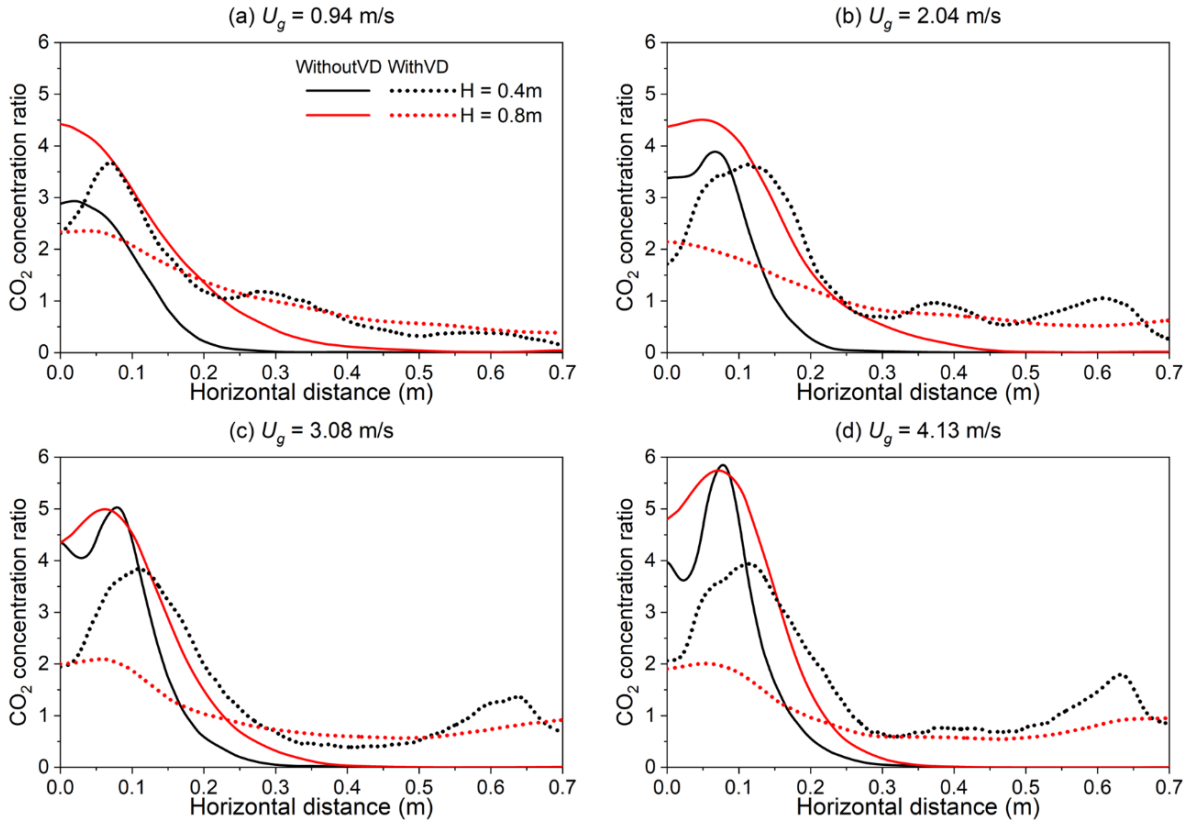

Figure 27. Comparison of lateral profiles of CO_2 concentration ratio at two selected heights (0.4 m and 0.8 m) for the fluidized bed without and with the VD under various operating conditions ((a) U_g = 0.94 m/s, (b) U_g = 2.04 m/s, (c) U_g = 3.09 m/s, (d) U_g = 4.13 m/s).

4.2.3 Performance of VDs with different configurations

Based on the experimental investigations, the configurations of the VD have significant effects on the performance of the VD. The impact of different configurations of the VD have been investigated with respect to the mixing behaviors and the pathways of volatiles in this section using CFD modelling with an Eulerian/Eulerian two fluid model coupled with a two-step EMMS/bubbling drag model.

Figure 28 shows the time-averaged distribution of CO_2 concentration in the XZ plane (left) and XY plane (right) at different heights, i.e. 0.4, 0.8, 1.2, and 1.6 m, without VD and with different VD configurations, under low and high superficial gas velocities. Without VD, the simulated volatiles do not diffuse to the right side, i.e. far away from the injection port, but flow upwards with primary air flow from the bottom. This phenomenon is much more pronounced in the case with higher superficial gas velocity. In the fluidized bed equipped with different VDs, Modes 1A and 2A show significantly higher CO_2 concentration near the injection port compared to the region far away from the injection port when the fluidized bed is operated under bubbling fluidization regime. Mode 1B and 2B show better mixing between the simulated volatiles and the primary air and exhibit superior performance in mixing simulated volatiles with the primary air in the upper part of the fluidized bed.

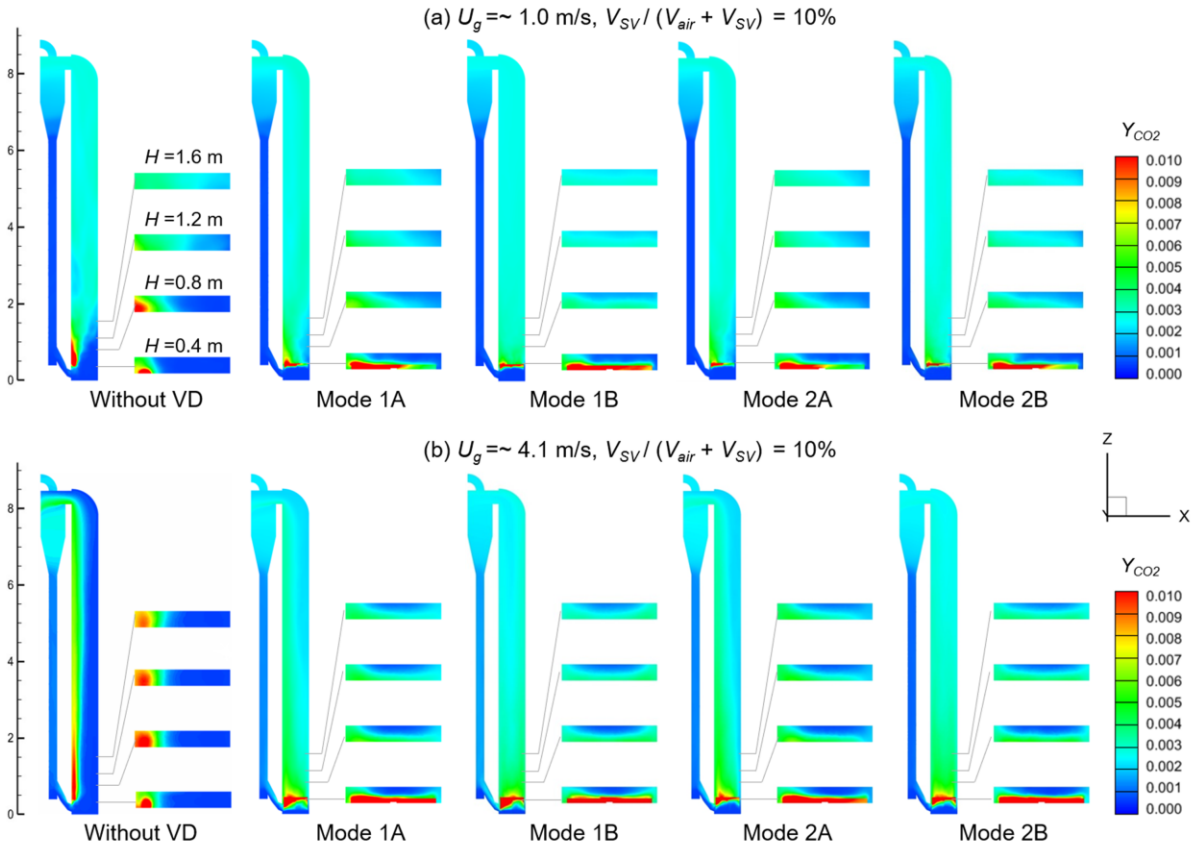

Figure 28. Contour plots of time-averaged CO_2 concentration of the fluidized bed without VD and with different VDs, i.e. Modes 1A, 1B, 2A, 2B, under low and high superficial gas velocities: (a) U_g = ~1.0 m/s, V_{SV} / (V_{air} + V_{SV}) = ~10%. (b) U_g = 4.1m/s, V_{SV} / (V_{air} + V_{SV}) = ~10%. The primary air distributor is AD1660.

To further evaluate the effects of different configurations of the VD on the mixing at different heights, Figure 29 (a) and (b) show the lateral profiles of CO_2 concentration ratio at the heights of 0.4 m and 0.8 m. The fluidized bed is in the bubbling fluidization regime and the primary air distributor is AD1660. As compared to Modes 1A and 2A, Modes 1B and 2B improve the horizontal distribution of simulated volatiles. Mode 1B with 58 distribution holes shows better performance than Mode 2B with 116 distribution holes due to the higher pressure drop over Mode 1B with less opening area of distribution holes. The profiles of CO_2 concentration with higher superficial gas velocity are given in Figure 29 (c) and (d). Also these results indicate that Modes 1B and 2B have better performance than Modes 1A and 2A. It is also worth noting that the mixing between the simulated volatiles and primary air is significantly improved by the VD under both bubbling fluidization and turbulent fluidization.

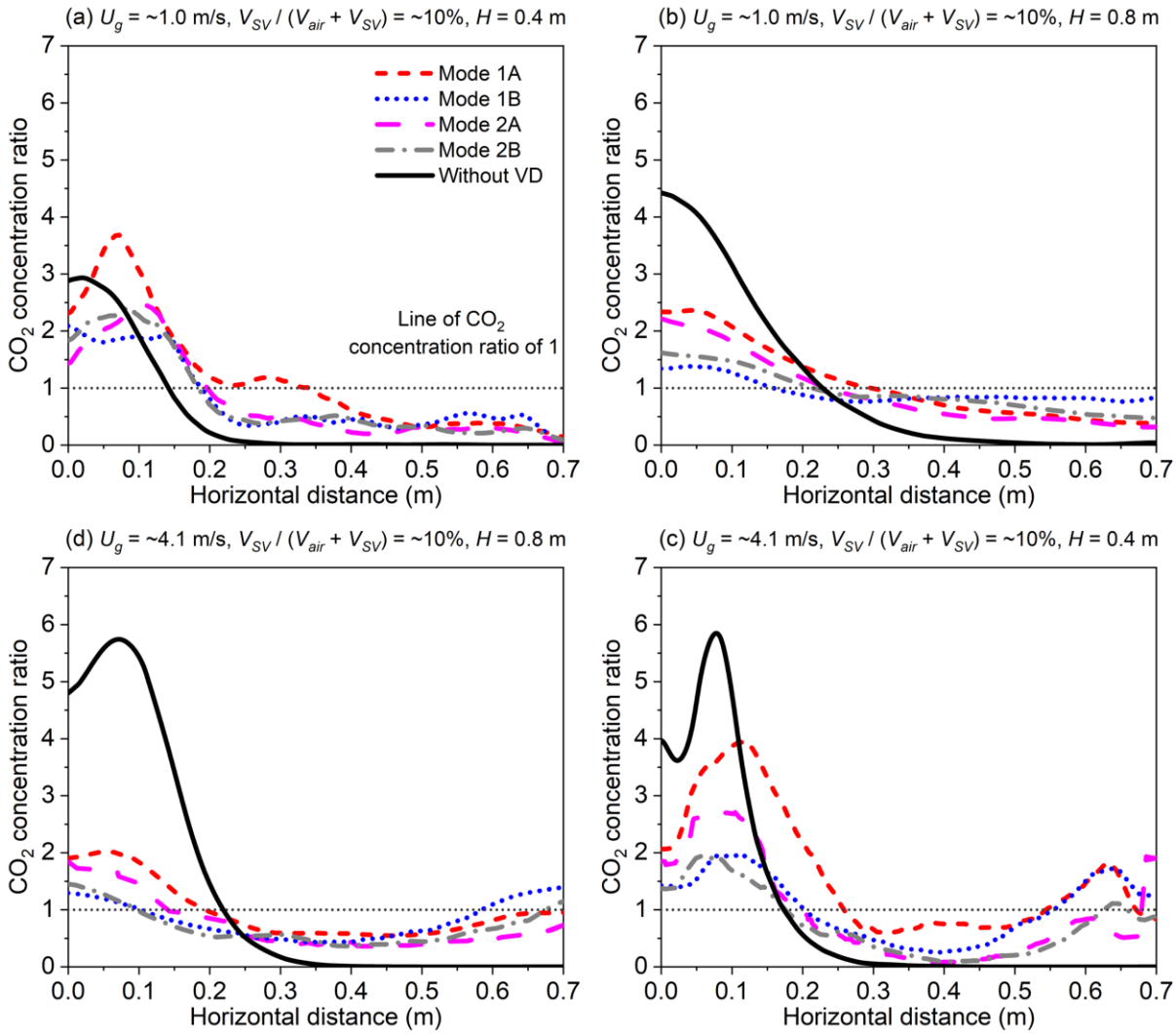

Figure 29. Comparison of the lateral profiles of CO_2 concentration ratio at two heights, i.e. H = 0.4 m and 0.8 m, for the fluidized bed without VD and with VDs of different configurations under low (~1.0 m/s) and high (~4.1 m/s) superficial gas velocities.

4.3 Implications for large-scale application of the VD

The investigation of the VD has been made in a cold-flow fluidized-bed model under varying fluidization regimes. The performance of the VD in the cold-flow model gives some hints for the performance of the VD in a real-world application with the same fluidization regime. But, what would be the expected operational conditions in a future fuel reactor using solid fuels? There are some differences between the operational conditions in current investigations in the cold-flow model and the ones expected in large-scale fuel reactors.

Firstly, the bottom fluidization gas flow would be low in a real-world fuel reactor. The bottom gas, either steam or a combination of steam and recycled CO_2, comes with a significant cost, and its major purpose is to keep the bed fluidized. Thus, the optimal bottom gas flow is likely the minimum flow needed to safely achieve adequate fluidizing conditions. Apart from the bottom fluidization gas flow, there are two major gas flows in the fuel reactor originating from the char and the volatiles. The char will mainly be part of the dense phase. Thus, the syngas

produced through gasification will also appear in the dense phase. This will make the dense phase “self-fluidizing”, which is likely helpful for improving the gas-solids contacting. It also means that the gas flow in the dense phase outside the VD will increase with bed height. Such a “self-fluidizing” regime is obviously difficult to accomplish in a cold-flow model. Therefore, it is relevant to consider different fluidization velocities in the evaluation, i.e. from the low velocities, typical of the fluidization flow, to the higher flows which are more relevant higher up in the bed. A second difference is that the flow of volatiles in a fuel reactor which uses a highly volatile biomass fuel, would be significantly higher than that used in these tests, because of practical limitations to the flow of simulated volatiles that could be added. A higher flow would obviously have implications for the dimensioning of the arms and the open area of the holes.

Despite these differences, it can nevertheless be concluded that the concept has been proven and can be expected to be useful in real-world applications. Moreover, the different configurations and conditions examined in this work should be helpful in the designing of large-scale applications.

5 Results and Discussion-Mn-based oxygen carriers

In this section, the results from the included Paper VI and Paper VII are summarized, which highlight the main findings about the performance of non-calcined manganese ores and manufactured calcium manganite as oxygen carriers in a batch reactor and a continuously circulating fluidized bed reactor, and a comprehensive examination of the distribution of primary elements and principal active phases for CLOU in both fresh and spent samples (Part II).

5.1 Performance in 300 W unit

5.1.1 CLOU effect

During warming up, both AR and FR were operated as bubbling fluidized beds, with 1 L_n/min N_2 flowing into both reactors for non-calcined Eramet HM, Guizhou and Sibelco braunite ores, with 1 L_n/min air flowing into both reactors for non-calcined UMK. A significant amount of O_2 released from non-calcined Eramet HM particles was observed during the warming up, which is due to the decomposition of MnO_2 to Mn_2O_3 and Mn_3O_4. During the warming-up of UMK ore, a release of CO_2 was observed, explained by the presence of calcite ($CaCO_3$).

These four natural manganese ores share similar primary elements such as Mn, Fe, Si, Ca, and Al, albeit with varying concentrations. Eramet HM and Sibelco braunite exhibit similarly high levels of Mn and lower levels of Fe. Guizhou is characterized by a higher Fe content compared to Mn. UMK displays a similar Mn content to Eramet HM and Sibelco braunite, but a much higher Ca content. Their elemental compositions vary widely, making these four ores particularly interesting as they provide a diverse range of elements commonly found in manganese ores from different geological regions. The comparison of CLOU, i.e. the O_2 released into inert atmosphere of the FR, among these four manganese ores is shown in Figure 30. UMK has the highest O_2 largely attributed to its higher Ca content and the resulting presence of the perovskite phase as indicated in Table 2 and section 5.3.2. Perovskite calcium manganite-based oxygen carriers are known for their strong ability to release oxygen [84, 85]. Among the other three manganese ores, Guizhou ranks the highest, followed by Sibelco braunite, with Eramet HM having the lowest O_2 release. This correlates with the Fe content as shown in Table 2, giving more Mn-Fe oxides, i.e. bixbyite via reaction (R6).

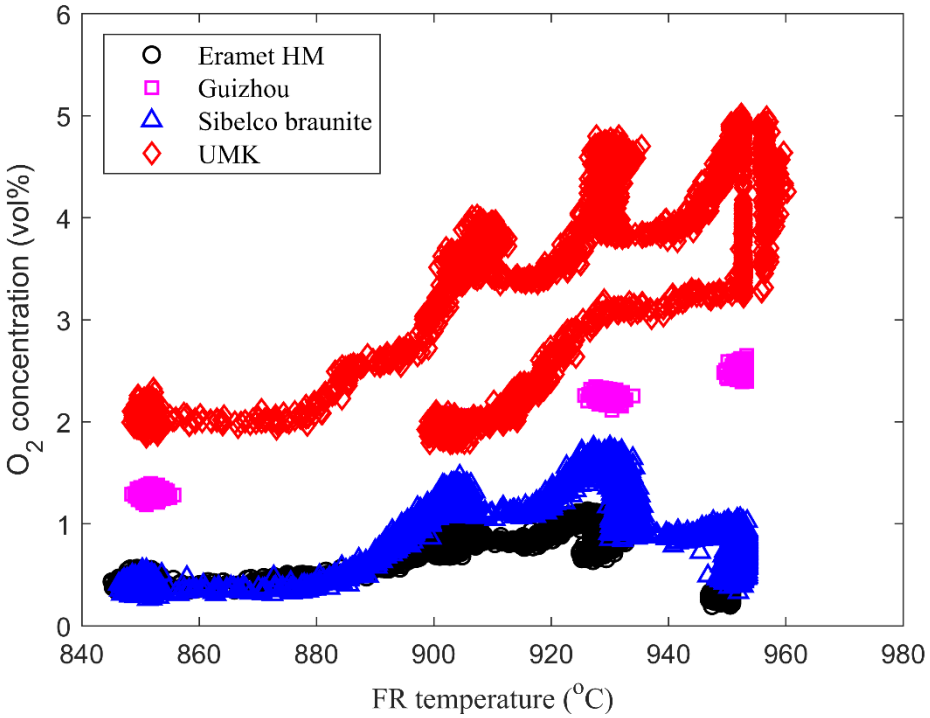

Figure 30. Comparison of CLOU effect of Eramet HM, Guizhou, Sibelco braunite, and UMK ores.

As presented in Figure 31, the O_2 concentration in FR for calcium manganite ranges from 4 to 8 vol% before CLC operations and is notably higher than those after operation with fuel. The oxygen deficiency, i.e., δ in $CaMnO_{3-\delta}$, of fresh calcium manganite sample is low, leading to a higher O_2 concentration in the FR. Temperature may influence solids circulation rates, the oxidation and O_2 release rates of the oxygen carriers, but more importantly the equilibrium amount of oxygen in the particle for a given O_2 partial pressure over the particles. When the temperature rises, the steady-state of $CaMnO_{3-\delta}$, is characterized by an increased δ [86, 87], and thus the excess oxygen will be released from calcium manganite. Hence, a temperature increase will first cause a release of O_2, and as the steady state δ value is approached, O_2 will fall.

As shown in Figure 31, the O_2 concentration for non-calcined UMK ore before CLC increases from 3.5 vol% to 5 vol% as the FR temperature is raised from 900 to 950 °C, notably higher than when FR temperature decreases from 950 to 900 °C, ranging from 3.2 vol% to 2 vol%. After CLC operation with CH_4, the CLOU effect of UMK also increases with temperature, ranging from 2.4 vol% to 3.0 vol% at temperatures of 900-950 °C. The concentration and release pattern of O_2 resembles that of the calcium manganite oxygen carriers in Paper VII.

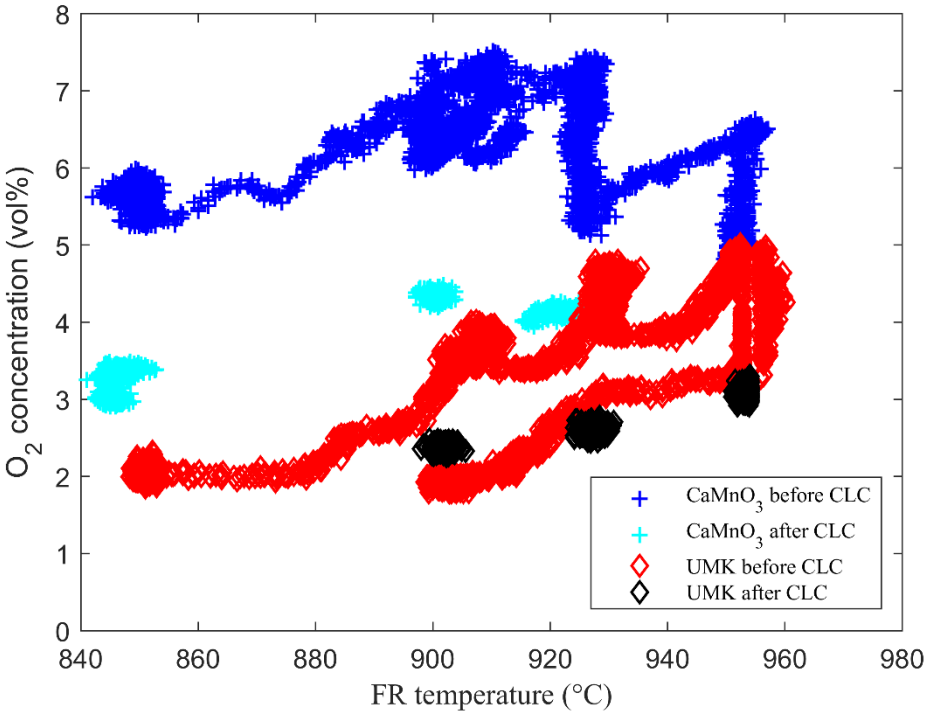

Figure 31. CLOU effect of calcium manganite and UMK ore before and after CLC operations.

5.1.2 Reactivity

Consistent with the CLOU effect of these four manganese ores and calcium manganite outlined in section 5.1.1, calcium manganite manufactured from Eramet HM ore demonstrates the highest CH_4 conversion, followed by UMK in the second place, Guizhou in the third place, while Sibelco braunite and Eramet HM exhibit the lowest CH_4 conversion at 950 °C, as illustrated in Figure 32 (a). Full CH_4 conversion can be achieved using calcium manganite with relatively low fuel flows at 950 °C.

Calcium manganite and UMK also exhibit the highest syngas conversion, with Sibelco braunite and Eramet HM following in the second and third places, while Guizhou has the lowest syngas conversion, as illustrated in Figure 32 (b). Full syngas conversion can be achieved using calcium manganite and UMK even with high fuel flows at 850 and 900 °C.

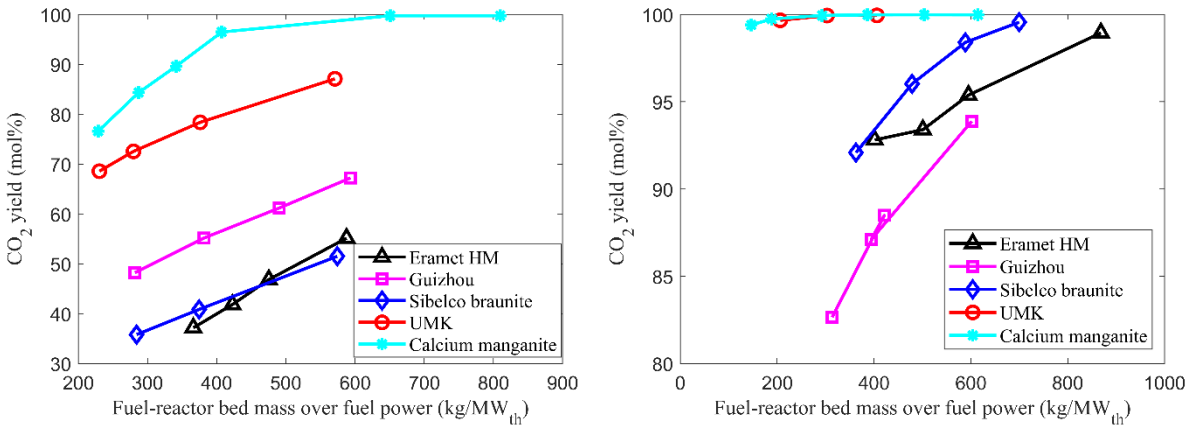

Figure 32. Comparison of reactivity of Eramet HM, Guizhou, Sibelco braunite, UMK, and calcium manganite towards CH4 at 950 °C and syngas at 900 °C (ores) and 850 °C (calcium manganite).

5.1.3 Attrition rate

The estimated attrition rates of the manganese ores in the 300 W unit presented in Table 9 are similar to those of calcined manganese ores [6]. Among these four manganese ores, Eramet HM, Guizhou, and Sibelco braunite show low attrition rate. While UMK has a bit higher attrition rate. Calcium manganite experiences average attrition rates ranging from 0.15 to 1.03 wt%/h with CH_4 and syngas. The higher initial attrition rate with syngas could be attributed to a rounding effect, as the fresh particles showed irregular shapes, see section 5.3.1, and some fragmentation of protruding parts may be expected.

Table 9. Estimated average attrition rate during 300 W tests with four manganese ores and calcium manganite.

Oxygen carrier	Initial weight (g)	Common filter (g)	AR filter (g)	FR filter (g)	FR water seal (g)	Total loss (g)	Fuel operation time (h)	Average attrition (wt%/h)
Eramet HM	350	1.4	0.3	0.2	0.1	2.0	8.5	0.07
Guizhou	350	1.6	1.0	0.1	0.3	3.0	9.0	0.10
Sibelco braunite	400	3.0	1.3	0.1	0.9	5.3	8.4	0.16
UMK	366	5.9	2.3	0.3	1.2	9.7	6.3	0.42
Calcium manganite batch 1	300	4.8	1.3	0.1	-	6.2	2.0 (Syngas)	1.03
Calcium manganite batch 2	300	2.1	1.3	0.4	7.0	10.8	23.6 (CH_4)	0.15

5.1.4 Further comparison

Figure 33 shows the normalized conversion of methane and syngas versus attrition, along with a comparison to calcined manganese ores. Here, 'normalized' refers to the gas conversion at 900 °C and 350 kg/MW_{th}. The changes in attrition are moderate, and except for Eramet HM, the attrition is slightly higher. A somewhat higher attrition is not unexpected, as the test series for the non-calcined materials are shorter, i.e. 6-9 h in fuel operation compared to 17-32 h for calcined materials, and attrition is normally higher during the first hours [6].

With respect to gas conversion, the changes are more pronounced. Eramet HM shows increased gas conversion, whereas Sibelco Braunite shows reduced gas conversion. Guizhou shows a large decrease in syngas conversion, but little change in methane conversion. UMK shows a slight increase in methane conversion, whereas the full conversion of syngas remains unchanged.

Despite the changes it can be said that UMK, Eramet HM and Sibelco braunite, are still among the best oxygen carriers considering both attrition and syngas conversion. Considering methane conversion and attrition, UMK, Eramet HM and Guizhou are still the best.

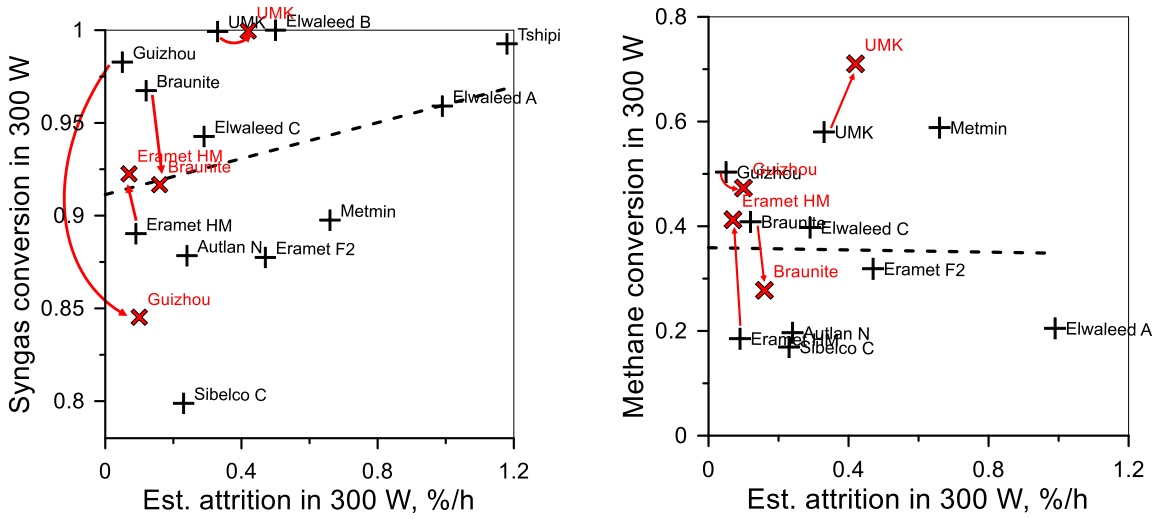

Figure 33. Syngas and methane conversion at 900 °C and 350 kg/MW$_{th}$. Red crosses show results for non-calcined ores. Adapted from [6].

5.2 Performance of calcium manganite in batch reactor

5.2.1 O_2 release

The oxygen release of 15 g fresh and used calcium manganite samples was further examined at varying temperatures in a batch fluidized-bed reactor. Figure 34 illustrates the O_2 concentrations in an N_2 atmosphere, with the ones from blank tests subtracted, versus the conversion at different temperatures. The amount of O_2 released is higher, and the speed of release is faster at higher temperatures. Furthermore, it is seen from Figure 34 that the oxygen release of the used sample is a bit lower than that of the fresh sample.

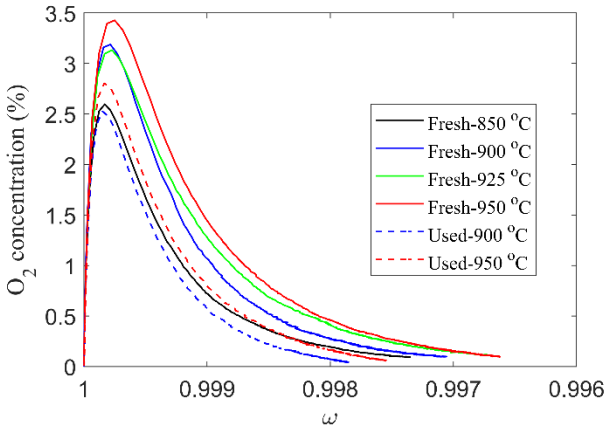

Figure 34. Oxygen release in an inert atmosphere of the batch reactor as a function of conversion of 15 g calcium manganite oxygen carrier under various temperatures. (Fresh: averaged data based on 5 cycles; Used: averaged data based on 3 cycles, sampled after 29 h operation with CH_4 in 300 W unit.)

5.2.2 Reactivity towards CH_4 and syngas

Figure 35 (a) depicts the CH_4 conversion versus the mass-based conversion of both fresh and used calcium manganite samples at various temperatures. In these tests, the bed mass over fuel power is 56.6 kg/MW_{th}. Elevated temperatures significantly enhance CH_4 conversion. Notably, there is little difference in reactivity between the fresh and used samples, despite the higher O_2 release of the fresh samples under inert conditions.

Figure 35 (b) presents the syngas conversion versus the conversion of both fresh and used calcium manganite samples at different temperatures. In these tests, the bed mass over fuel power is 11.4 kg/MW_{th}. With the exception of the tests at 850 °C, all calcium manganite samples achieve full syngas conversion for ω ranging from 1 to 0.99. Notably, the reactivity of the fresh and used calcium manganite samples towards syngas is almost identical. Thus, it can be concluded that 25 h of CLC operation did not affect reactivity in a significant way.

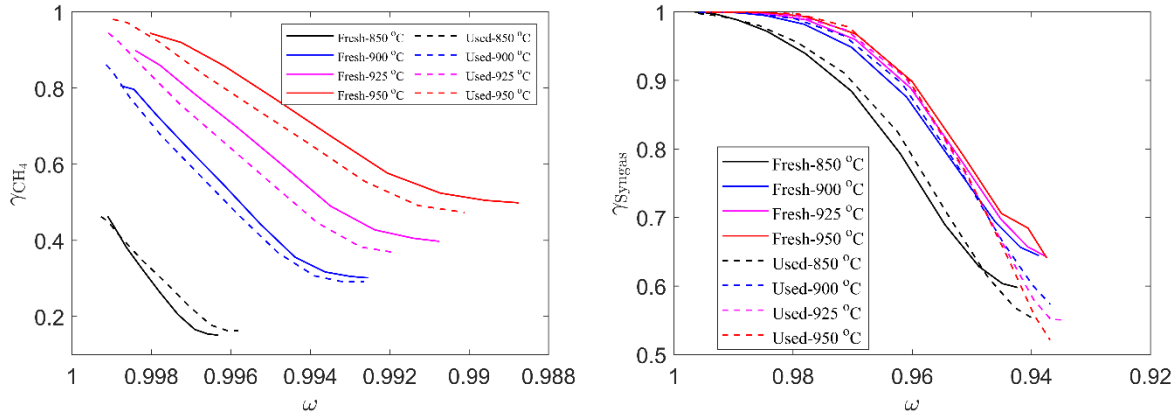

(a) Methane conversion (b) Syngas conversion

Figure 35. Methane and syngas conversion over the corrected conversion of fresh and used calcium manganite samples at varying temperatures in the batch reactor.

5.3 Characterizations

5.3.1 Physical properties

The appearance of the fresh and used four manganese ores and calcium manganite is shown in the light microscope images in Figure 36. Fresh Eramet HM particles appear black and quite round with smooth surfaces, while the used ones exhibit a slightly browner hue and sharper edges. Fresh Guizhou particles appear black-brown and have sharp edges and rugged morphology, while the used Guizhou particles exhibit two types of particles, i.e. black-brown ones similar to the fresh Guizhou particles and silvery white ones which could be hematite. Fresh Sibelco braunite particles show similar appearance and morphology as Guizhou ore, while the used particles are brown. Fresh UMK particles have quite irregular shapes and colors of grey and brown, while the used ones are browner and have a more rugged appearance. Some fragments were observed in the used UMK sample. Some yellow-transparent particles were observed in fresh UMK sample, suggesting the presence of Si-containing components. The fresh manufactured calcium manganite particles have quite irregular shapes, while the particles used in the 300 W CLC reactor became more rounded and smaller.

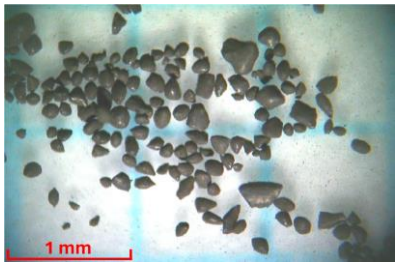

(a) Fresh Eramet HM Ore

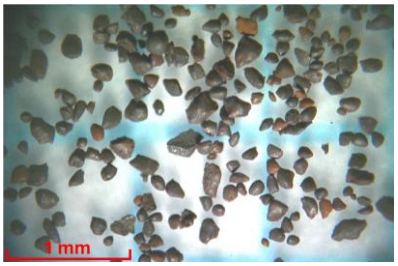

(b) Used Eramet HM Ore

(c) Fresh Guizhou ore

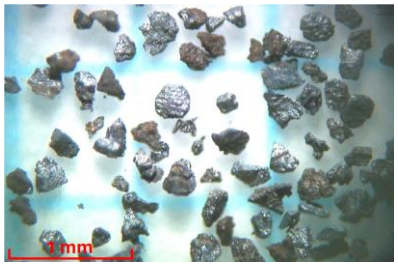

(d) Used Guizhou ore

(e) Fresh Sibelco braunite ore

(f) Used Sibelco braunite ore

(g) Fresh UMK ore

(h) Used UMK ore

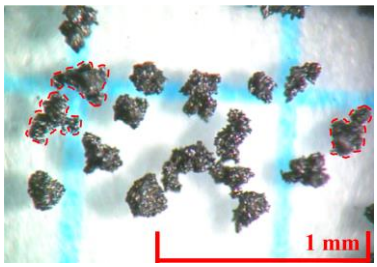

(i) Fresh Calcium manganite

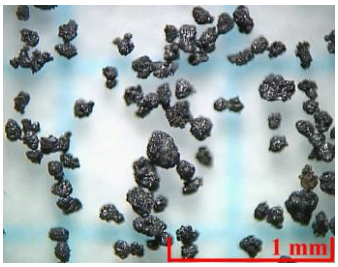

(j) Used Calcium manganite

Figure 36. Light microscope photos of fresh and used Eramet HM, Guizhou, Sibelco braunite, UMK ores, and calcium manganite. Note that the used particles are from 300 W unit after 8.5 h, 9 h, 8.4 h, 6.3 h and 29 h of fuel operations, respectively.

The estimated bulk density and particle size distribution of the fresh and used four manganese ores and calcium manganite are presented in Table 10. The bulk density of the used Eramet HM and Guizhou samples is slightly higher than that of the fresh ones. The bulk density of the used Sibelco braunite and UMK samples is lower than that of the fresh ones. This difference

agrees with the larger size of the used Sibelco braunite and UMK particles, as shown in Table 10.

Table 10. Physical properties of fresh and used Eramet HM, Guizhou, Sibelco braunite, UMK ores, and calcium manganite.

Oxygen carrier	Poured bulk density determined based on standard ISO 3923-1 (kg/m^3)	Particle size distribution D10, D50, D90 (μm)
Eramet HM Fresh	1755	53,104,195
Eramet HM Used	1844	43,92,188
Guizhou Fresh	1400	76,121,177
Guizhou Used	1528	75,124,176
Sibelco braunite Fresh	2138	113,168,219
Sibelco braunite Used	1623	107,180,226
UMK Fresh	1428	86,185,223
UMK Used	1043	85,217,257
Calcium manganite Fresh	1102	112, 157, 244
Calcium manganite Used	1304	84, 129, 202

5.3.2 Crystalline phase analysis

The main crystalline phases in fresh and used Eramet HM, Guizhou, Sibelco braunite, UMK ores, and calcium manganite have been identified, see Table 11. The primary phases in fresh Eramet HM are MnO_2 and KMn_8O_{16}, where manganese is in the Mn^{4+} state. After the warming up and CLC operations, the main phases become hausmannite and bixbyite, indicating Fe is incorporated within the manganese oxides structure. Guizhou contains more Fe than Mn, and higher contents of Al and Si than Eramet HM, see Table 2, and the main crystalline phases identified in fresh Guizhou are hematite and braunite. The main phases identified in Sibelco braunite ore are braunite, hausmannite, and hematite. UMK has the highest Ca content of the four ores. The main phases identified in fresh UMK are braunite, calcite, and hematite. After the operation of UMK in 300 W unit, braunite is no longer present in used UMK and there are more Mn-Fe-containing phases, i.e. hausmannite, bixbyite, and jacobsite, and Mn-Ca phases, i.e. perovskite.

Two main crystalline phases, i.e. $CaMnO_3$ and $CaMn_2O_4$, have been identified in both fresh and used calcium manganite samples. The relative molar ratio of $CaMnO_3$ to $CaMn_2O_4$ in fresh sample is 3.5 based on the relative weight contents of the two phases indicated in Table 11, corresponding to a molar ratio of Ca/Mn in fresh sample of 0.82. The actual molar ratio of Ca/Mn is 0.83 based on the amounts of Ca and Mn in the raw materials used in this manufactured calcium manganite sample.

Table 11. Relative weight percentages of phases in fresh and used Eramet HM, Guizhou, Sibelco braunite, UMK ores and calcium manganite samples, derived with semi-quantitative analysis of the XRD data.

Phase	Eramet HM		Guizhou		Sibelco braunite		UMK		Calcium manganite	
	Fresh	Used	Fresh	Used	Fresh	Used	Fresh	Used	Fresh	Used
Pyrolusite MnO_2	42									
Cryptomelane KMn_8O_{16}	58									
Braunite Mn_7SiO_{12}			40	17	38	22	59			
Hausmannite $(Mn,Fe)_3O_4$		85			22	48		46		
Bixbyite $(Mn,Fe)_2O_3$		5			32	18		10		
Calcite $CaCO_3$							20	9		
Marokite $CaMn_2O_4$									30	50
Perovskite $CaMnO_3$								6	70	50
Hematite Fe_2O_3			60	52			11			
Lime CaO							5			
Spinel $(Mn,Fe)_3O_4$		9		21	8			10		
Spessartine $Mn_3Al_2(SiO_4)_3$				10						
Quartz SiO_2							6	21		

5.3.3 Morphology and chemical distribution

The SEM images and EDX elemental mapping of Eramet HM particles, as shown in section Appendix, reveal a surface layer containing Mn and rich in Fe, Al, and Si compared to the core. SEM-EDX analysis, see Figure 37 (a) and (b), indicates the compositions in the surface layer and core of these particles. The higher contents of Fe, Al, and Si indicate a Fe-Al-Si-rich surface layer on fresh and used Eramet HM particles, whereas the higher contents of Mn and K indicate that the core of the particles is richer in Mn and K. It appears that K migrates from the core to the surface layer during operation, as shown in Figure 37.

SEM images of used Eramet HM particles in section Appendix indicate that CLC operation introduces increased porosity to the particles. From the fresh to the used sample, Fe becomes more evenly distributed throughout the particle, while Al and Si remain concentrated in the surface layer. This suggests that Fe is more readily dissolved into the Mn oxide structure compared to Al and Si. The phases identified using XRD of the used samples, such as hausmannite and bixbyite, also support this observation.

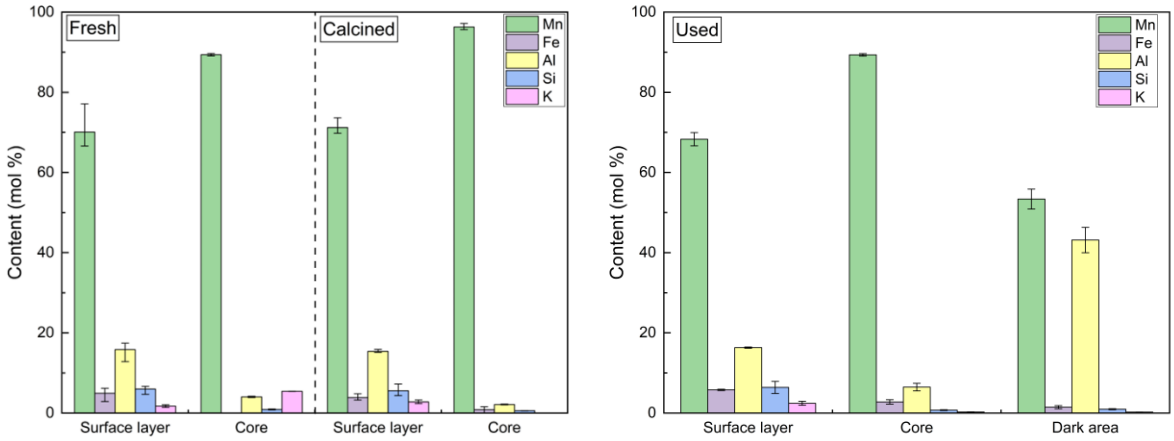

Figure 37. Relative contents of Mn, Fe, Al, Si, K in the fresh, calcined (a), and Used (b) Eramet HM ore samples obtained by SEM-EDX analysis.

The SEM images and EDX elemental mapping of fresh and used Guizhou, as shown in section Appendix, reveal two distinct types of particles, namely Type A, bright particles, and Type B, somewhat darker particles. The elemental distribution of Fe, Mn, Al, and Si within these different particles, as illustrated in Figure 38, indicates that Type A particles are rich in Mn, suggesting the presence of braunite, while Type B particles are rich in Fe-Al-Si, with hematite being the likely phase, containing higher levels of Al and Si compared to the braunite phase.

Upon comparing the fresh and used Guizhou particles in section Appendix, it is evident that a surface layer has formed around the Type B Fe-Al-Si-rich particles. This layer is likely the silvery white particles observed in the light microscope photo in Figure 36 (d). The analysis of elemental distributions of used Guizhou illustrated in Figure 38 and section Appendix indicates that Fe concentrates in the surface layer of Type B particles whereas the core of Type B particles in used Guizhou sample is still rich in Fe-Al-Si. It is obvious that Type A particles in the used Guizhou contain more Fe than fresh Guizhou according to Figure 38, which further highlights the incorporation of Fe into the braunite phase.

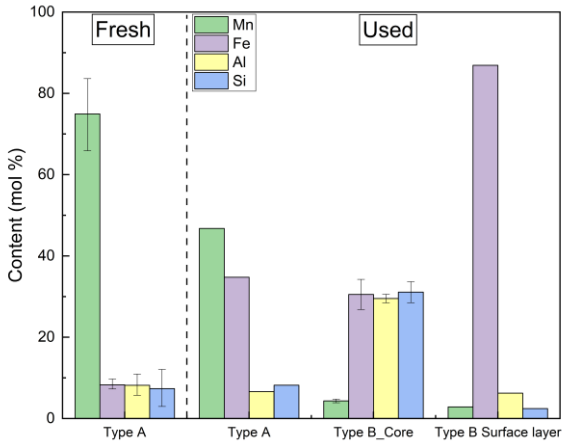

Figure 38. Relative contents of Mn, Fe, Al, and Si in the different types of fresh and used Guizhou ore samples.

The SEM image of fresh Sibelco braunite particles in section Appendix reveals two types of particles: bright, less porous particles, and dark, porous particles. The elemental distribution of

Mn, Fe, Si, and Ca within these different particles, as illustrated in section Appendix, indicates that Mn, Fe, Si, and Ca are generally evenly distributed throughout these particles.

Upon comparing the fresh and used Sibelco braunite particles in section Appendix, it is evident that CLC operation results in more porosity. The SEM image and elemental distribution analysis of used Sibelco braunite exhibits two types of particles: Mn-rich particles and Fe-rich particles. The relative contents of Mn, Fe, Si, and Ca in these Mn-rich and Fe-rich particles are presented in Figure 39. It indicates that these Mn-rich and Fe-rich particles mainly contain Mn and Fe, with Mn-Fe oxides like hausmannite, bixbyite for the Mn-rich particles, and hematite for Fe-rich particles. There is a certain area inside the Mn-rich particles appearing darker. This dark area inside these Mn-rich particles is rich in Si-Ca according to the point analysis at position 5 and 6 in Figure 39.

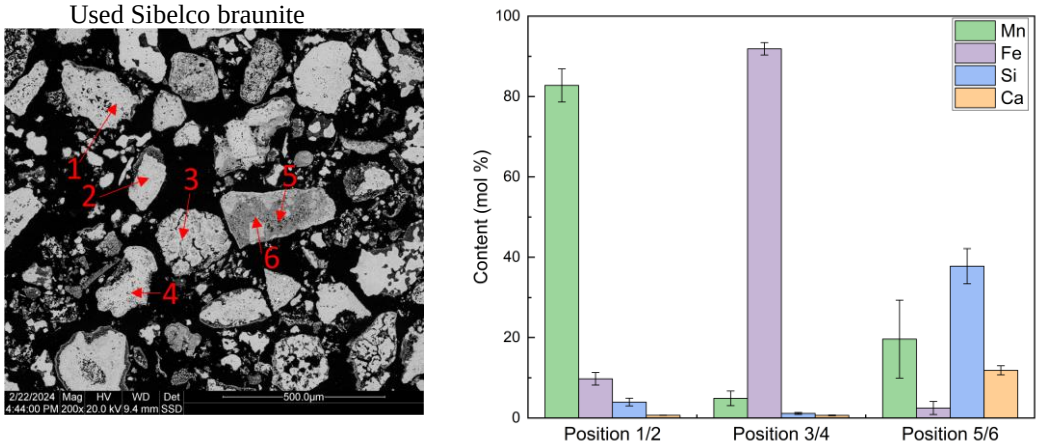

Figure 39. SEM image and Relative contents of Mn, Fe, Si, and Ca of used Sibelco braunite ore.

The SEM image and the elemental distribution analysis of fresh UMK particles in section Appendix reveal two types of particles: bright, Mn-rich particles containing more Fe and Si, and dark, Ca-rich particles, suggesting the presence of braunite and calcite.

When comparing the SEM images of fresh and used UMK particles in section Appendix, it is evident that CLC operation introduces more porosity to these particles. The SEM image and elemental distribution analysis of the used UMK particles in section Appendix exhibit three types of particles: Mn-rich particles, Ca-rich particles, and Si-rich particles. The relative contents of Mn, Fe, Si, and Ca in these particles are presented in Figure 40. It indicates that these Mn-rich particles contain certain amounts of Ca, Si, and Fe. However, these elements in Mn-rich particles are not evenly distributed based on the error bars shown in Figure 40. An obvious Ca-Si-rich surface layer was found for these Mn-rich particles. Inside these particles, there are some areas appearing darker. The dark area contains less Mn and more Ca and Si compared to the bright area inside these Mn-rich particles. The Ca-rich particles also incorporate some Mn, Si and Fe elements. The Si-rich particles could be SiO_2 surrounded by a Ca-Si-rich surface layer.

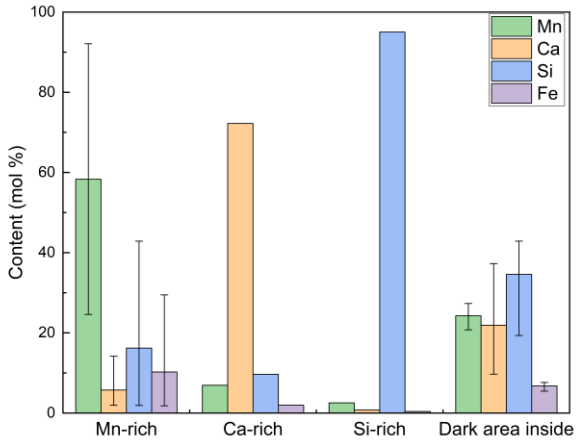

Figure 40. Relative contents of Mn, Ca, Si, and Fe in different types of particles in used UMK ore. Note: Dark area inside Mn-rich particles.

The calcium manganite particles exhibit a porous structure, as shown in section Appendix. The SEM image and elemental distribution of fresh calcium manganite particles reveals two distinct zones within the particles, namely a bright zone and a somewhat darker zone. SEM-EDX analysis indicates the relative contents of Ca, Mn, Fe, and Al in the dark and bright zones, as shown in Figure 41 (a). The dark zone has a Ca/Mn molar ratio of about 1, indicating $CaMnO_3$. Conversely, the bright zone displays a Ca/Mn molar ratio of approximately 2, corresponding to $CaMn_2O_4$. Furthermore, there are no zones where Ca is missing indicating good penetration despite the relatively large particle size of the raw materials used for producing calcium manganite.

Fe substitution of Mn in the perovskite structure of calcium manganite can improve the stability of the microstructure of the particles, the oxygen uncoupling ability, and the reactivity [23, 31, 45]. Al and Si are mostly seen in inert phases, i.e. with no oxygen transfer capability and calcium silicates and aluminates can be formed when 50% mixing ratio Ca/(Mn+Fe) is employed for the production of calcium manganite from CaO and Mn ore containing Si and Al [32]. The latter appears to slow down the redox reaction kinetics. Interestingly, XRD analysis of the calcium manganite studied in this work did not reveal any presence of phases containing Fe, Al and Si. However, SEM-EDX analysis demonstrates that the dark zone, $CaMnO_3$, contains higher concentrations of Fe, Al and Si, Figure 41 (a). This suggests that the perovskite structure can incorporate Fe, Al and Si into its structure.

The average contents of various elements in fresh and used samples are illustrated in Figure 41 (b). In comparison to the fresh sample, the used sample exhibits higher Mn content and lower Ca content, suggesting that $CaMn_2O_4$ persists in the reactor instead of being elutriated as fines. However, the small loss of fines with somewhat higher Ca/Mn ratio cannot explain the change in Ca/Mn ratio between fresh and used particles.

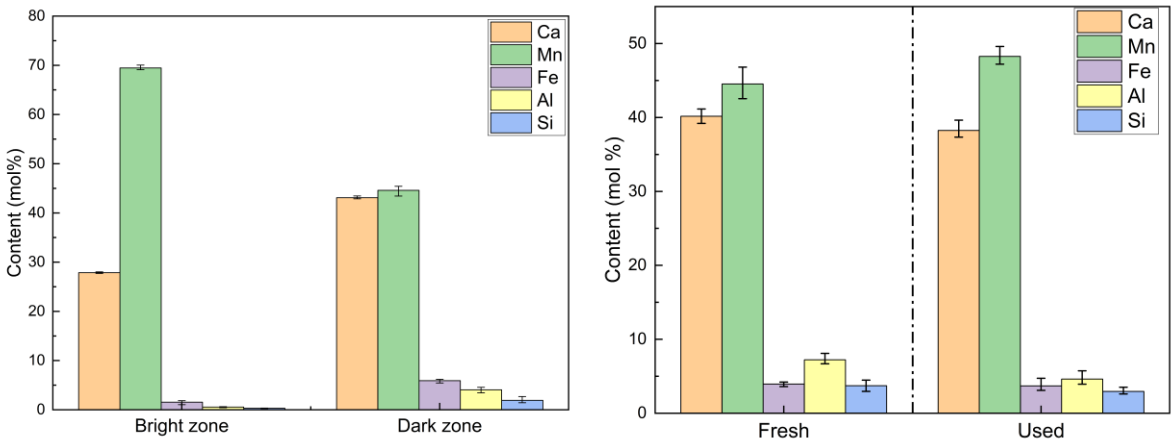

(a) (b)

Figure 41. (a) Relative contents of Ca, Mn, Fe, Al, Si in the different zones of the fresh calcium manganite particles and (b) average contents in fresh, used calcium manganite samples.

5.3.4 Pathways of primary elements

The primary elements of the four manganese ores are Mn, Fe, Al, Si and Ca, as indicated in Table 12. However, the crystalline phases identified and elemental distributions in these four manganese ores are quite different.

The main phases in Eramet HM are manganese oxides with manganese as Mn^{4+}. With respect to the elemental distribution in Eramet HM, the particles have visible surface layers. Fe, Al, and Si are concentrated in the surface layer and the core is rich in Mn and K. After the calcination of Eramet HM, i.e., in air at 950 °C for 24 h, the difference between the particle core and surface layer is still visible, and K migrates from the particle core to the surface layer. Fe becomes more evenly distributed over the cross-section of the particles. The presence of hausmannite and bixbyite phases indicates that Fe is more dissolved into Mn structure. Compared to the calcined Eramet HM, the used one has similar elemental distributions and crystalline phases. The difference is that there are certain areas in the core, rich in Mn and Al.

Guizhou contains mainly Mn, Fe, Al, and Si like Eramet HM, but has more Fe than Mn. The main crystalline phases in fresh Guizhou are hematite and braunite. The four primary elements are found in two different types of particles in fresh Guizhou sample: Mn-rich particles and Fe-Al-Si-rich particles, corresponding to braunite and hematite. Calcined Guizhou has the same phases, hematite and braunite. After the CLC operation of fresh Guizhou, Mn-rich particles incorporate more Fe, giving more Mn-Fe phase ($(Mn,Fe)_3O_4$) and less Mn-Si (Mn_7SiO_{12}). For the Fe-Al-Si-rich particles, Fe concentrates in the surface to form an obvious surface layer with Fe-Al-Si still rich in the core.

Sibelco braunite mainly contains Mn, Fe, Si, and Ca, less of Al and more of Ca compared to Eramet HM and Guizhou. The Mn content of Sibelco braunite is close to that of Eramet HM, with a bit higher content of Fe. These four elements are generally evenly distributed throughout all particles of the fresh Sibelco braunite, with braunite, hausmannite, and bixbyite identified. After the CLC operation of fresh Sibelco braunite, these fresh particles with elements evenly distributed become two different types: Mn-rich particles containing small amounts of Fe and Si, and Fe-rich particles containing small amount of Mn. Similar to Used Eramet HM, there

are also some darker areas observed in Mn-rich particles, containing mostly Si, Mn, and Ca. Similar to Guizhou, more Mn-Fe phases and less Mn-Si phase are identified in used Sibelco braunite, as shown in Table 11, indicating that Fe can be more easily incorporated into the Mn structure, as compared to Si.

UMK contains Mn, Fe, Ca, and Si. The key difference is UMK contains more Ca than the other three ores. Fresh UMK mainly has two types of particles, Mn-rich particle containing Fe and Si, corresponding to braunite, and Ca-rich particles with calcite. After the CLC operation of fresh UMK, the Mn-rich particles dissolved more Ca with an obvious surface layer rich in Ca and Si. The Ca-rich particles also incorporate more Si, Mn, and Fe compared to the fresh samples. More Mn-Fe oxides phases are identified in the used UMK sample, and braunite is no longer detected, suggesting that Fe can replace Si in Mn structures. The formation of perovskite $CaMnO_3$ in used UMK sample is associated with the higher content of Ca in UMK. Comparing the distribution of Ca and Mn in fresh and used particles implies that Ca is transferred from particles with no or little Mn into and unto Mn-rich particles. This migration is also associated with the formation of calcium manganite and marokite.

The calcium manganite manufactured from Eramet HM and limestone mainly contains Mn, Ca, Fe, Al, and Si. Both fresh and used calcium manganite particles show two zones: dark zones appearing as $CaMnO_3$ and bright zones appearing as $CaMn_2O_4$. Higher concentrations of Fe, Al, and Si in the $CaMnO_3$ zone, indicate that the perovskite structure can incorporate Fe, Al, and Si into its structure.

As discussed in section 5.1.4, it seems that the calcination did affect the performance of the oxygen carriers, but normally the effect on reactivity is moderate and the effect on attrition is small. The effect on reactivity could be associated with surprisingly large differences in the phases identified by XRD in Table 12. The detailed information about the phases in fresh, used, calcined, and calcined&used samples can be found in Paper VII. When examining the differences in phase composition, pre-calcination is not necessarily the only explanation. Another factor to consider is that the duration of fuel operation with the calcined materials was three to five times longer.

A more interesting observation is the migration of elements seen in the characterization, contributing to the formation of various combined manganese oxides with CLOU properties. It also seems like elements are transferred between particles, e.g. from calcite particles to Mn-rich particles in the case of UMK, resulting in the formation of calcium manganite and marokite. This migration is all the more interesting as it happened in only 6 h of operation with fuels. This suggests that significant amount of perovskite could form under longer operation of manganese ores together with lime. Could this be a route for low-cost ‘production’ of highly reactive calcium manganite?

Table 12. Primary elements, active phases, and elemental distribution in Fresh, Calcined, and Used Mn ores.

Mn ore	Primary element	Active crystalline phase			Elemental distribution
		Fresh	Calcined	Used	
Eramet HM	Mn, Fe, Al, Si, K	MnO_2 KMn_8O_{16}	$(Mn,Fe)_3O_4$ $(Mn,Fe)_2O_3$	$(Mn,Fe)_3O_4$ $(Mn,Fe)_2O_3$ Fe_3O_4	• Fresh Surface layer: Mn-Al-Fe-Si Core: Mn-K (Al) • Calcined Surface layer: Mn-Al-Si-K (Fe) Core: Mn (Al, Fe) • Used Surface layer: Mn-Al-Si-K (Fe) Core: Mn (Al, Fe) Dark area in core: Mn-Al
Guizhou	Fe, Mn, Al, Si	Fe_2O_3 Mn_7SiO_{12}	Fe_2O_3 Mn_7SiO_{12}	Fe_2O_3 $(Mn,Fe)_3O_4$ Mn_7SiO_{12} $Mn_3Al_2(SiO_4)_3$	• Fresh Type A: Mn (Fe, Al, Si) Type B: Fe-Al-Si (Mn) • Used Type A: Mn-Fe (Al, Si) Type B (Core): Fe-Al-Si (Mn) Type B (Surface): Fe (Al, Mn, Si)
Sibelco braunite	Mn, Fe, Si, Ca	Mn_7SiO_{12} $(Mn,Fe)_2O_3$ $(Mn,Fe)_3O_4$	Mn_7SiO_{12} $(Mn,Fe)_3O_4$ Fe_2O_3	$(Mn,Fe)_3O_4$ Mn_7SiO_{12} $(Mn,Fe)_2O_3$	• Fresh Mn-Fe-Si-Ca evenly distributed • Used Mn-rich: Mn (Fe, Si) Fe-rich: Fe (Mn) Dark area in Mn-rich: Si-Mn-Ca (Fe)
UMK	Mn, Ca, Fe, Si	Mn_7SiO_{12} $CaCO_3$ Fe_2O_3	N/A	$(Mn,Fe)_3O_4$ $(Mn,Fe)_2O_3$ $CaMn_2O_4$ $CaMnO_3$	• Fresh Mn-rich: Mn-Fe-Si Ca-rich: Ca • Used Mn-rich with surface layer: Mn-Fe (Si, Ca) Ca-rich: Ca (Si, Mn, Fe) Si-rich: SiO_2 Dark area in Mn-rich: Ca-Si (Mn)
Calcium manganite	Mn, Ca, Fe, Al, Si,	$CaMnO_3$ $CaMn_2O_4$	N/A	$CaMnO_3$ $CaMn_2O_4$	• Fresh Dark zone: $CaMnO_3$ (Fe, Al, Si) Bright zone: $CaMn_2O_4$ • Used Dark zone: $CaMnO_3$ (Fe, Al, Si) Bright zone: $CaMn_2O_4$

6 Conclusion

Chemical-looping combustion (CLC) of renewable biomass provides a promising pathway towards negative CO_2 emissions with high efficiency power/heat production. As CLC technology moves from pilot-scale investigations to larger scales, it is important to secure the potential of low cost for CLC. One key aspect is the fuel conversion and the costs associated with subsequent oxygen polishing steps and oxygen carriers. The work presented in this thesis was focused on investigating different economically feasible methods to improve the fuel conversion in the fuel reactor. This improvement can be approached from two perspectives: gas-solids contact, specifically focusing on volatiles, and the reactivity of the solids, i.e. the oxygen carrier.

Part I of this thesis focuses on a concept known as the volatiles distributor (VD), which was investigated in a cold-flow fluidized-bed model and with computational fluid dynamics (CFD) modeling. The objective is to attain a more uniform cross-sectional distribution of volatiles, enhance gas-solids contact, and improve gas conversion in the fuel reactor. The current work provides the first detailed experimental proof-of concept of such device. The results presented in Papers I-V include the following key conclusions:

- The horizontal distribution of simulated volatiles could be improved significantly by the VD, especially in the exploding bubble regime, i.e. irregular bubbles containing more particles under relatively high fluidization velocities.
- Higher flowrate of simulated volatiles increases the pressure drop over the distribution holes, lowers the bed level inside the VD and thus improves the uniformity of horizontal distribution of volatiles to some extent.
- Configurations of the VD with unevenly arranged and less open area of the distribution holes where volatiles are introduced can improve the uniformity of the horizontal distribution of volatiles.
- Internal baffles at the bottom of the VD give more particles inside the VD and lower the upward flow of bottom air to the inside of the VD in both single and multiple bubble regimes, which improves the uniformity of the horizontal distribution of the volatiles and prevents volatiles from slipping below the VD edge near the inlet.
- CFD simulations with the two-step EMMS/bubbling model reveal improved mixing between simulated volatiles and bed materials with the VD installed, highlighting its efficiency in addressing incomplete conversion of high-volatile fuels like biomass in fluidized bed systems.

In general, the effectiveness of the VD has been proven in both cold-flow model and CFD simulations and the flexibility of the VD design has also been demonstrated, with different configurations, i.e. different open area of the distribution holes and different arrangements of holes, and internal baffles at the bottom of the VD. These flexibilities of the design should be important and instructive for the large-scale application of the VD.

Part II of this thesis investigates manganese-based oxygen carriers capable of releasing oxygen in the gas phase to enhance fuel conversion in the fuel reactor. The performance of four natural manganese ores and one calcium manganite produced from natural ore and limestone was examined. The key conclusions drawn from this investigation are outlined in Papers VI-VII:

- CLC operations with non-calcined manganese ores proceed as smoothly as with calcined ones, indicating that energy-intensive and costly pre-calcination of manganese ores is not necessary.
- Mn-Fe, Mn-Si, and Mn-Ca oxides such as bixbyite, braunite and perovskite phases are the main phases for the oxygen release of these natural manganese ores as CLOU oxygen carriers.
- Si in the Mn oxide phase (braunite) of these natural manganese ores can be displaced and replaced by Fe during CLC operation, forming Mn-Fe oxide phases such as bixbyite and hausmannite.
- The content of Fe in manganese ores seems to play an important role in their ability to release oxygen.
- A sufficiently high content of Ca in manganese ores facilitates the formation of perovskite calcium manganite, which enhances both the O_2 release and reactivity.
- The manufactured calcium manganite exhibits higher oxygen release capacity and CH_4/syngas conversion compared to the four natural ores.
- The main phase $CaMnO_3$ in the calcium manganite produced absorbs more Fe, Al, and Si as impurities, compared to the byproduct phase $CaMn_2O_4$.

In conclusion, the successful operation of these non-calcined manganese ores provides added evidence for the high relevance of manganese ores as oxygen carriers in a future commercialization of CLC. Furthermore, use of a perovskite-structured oxygen carrier, calcium manganite, synthesized from manganese ore and limestone through a straightforward process in CLC could be another effective and affordable way of increasing fuel conversion in the fuel reactor.

7 Nomenclature

$A_{orifice}$	Open area of the orifices [m^2]
c_{cal}	Ideal average CO_2 concentration in the cross-section of the riser [ppm]
c_m	Measured CO_2 concentration [ppm]
$c_{s,h_{1\to2}}$	Solids concentration in the middle of h_1 and h_2 [kg/m^3]
$c_{VD,mea}$	CO_2 concentration measured inside VD [ppm]
$c_{VD,avg}$	Average CO_2 concentration inside VD [ppm]
$\bar{c}$	Average CO_2 ratio [$-$]
c_H/c_L	Ratio between the highest and the lowest CO_2 concentration at HSV [$-$]
C_d	Orifice discharge coefficient [–]
$D1, D2$	Dilution factors of the concentration inside the VD [–]
dp/dh	Pressure drop gradient [kPa/m]
f_s	Pressure sampling frequency [Hz]
Δf	Frequency resolution [Hz]
$F(f)$	Fourier transform of the autocorrelation sequence of the time series of pressure signals [kPa]
g	Acceleration of gravity [m/s^2]
h_1, h_2	Different heights of the pressure measurement positions [m]
h_b	Dense bed height inside volatiles distributor [m]
h_{bottom}	Height of the bottom of the volatiles distributor [m]
h_{hole}	Height of the distribution holes [m]
Δh	Distance between the dense bed height inside the VD and the distribution holes level [m]
L	Number of pressure signals segments [$-$]
MF_{CO_2}	CO_2 flow [m_n^3/h]
MF_{SA}	Air flow used for simulating volatiles [m_n^3/h]
MF_{PA}	Primary air flow for the main fluidization [m_n^3/h]
m_i	Mass of the oxygen carrier at time i
m_{ox}	Mass of the fully oxidized oxygen carrier
N_s	Length of segments of the pressure signals [$-$]
$P_{xx}(f)$	Power spectrum density [kPa^2/Hz]
$p_{windbox}$	Pressure inside the wind box [kPa]
p_0	Pressure at the bottom of the riser [kPa]
p_8	Pressure at the top of the riser [kPa]
Δp_{AD}	Pressure drop over the air distributor [kPa]
Δp_{riser}	Pressure drop along the riser [kPa]
p_{h_1}, p_{h_2}	Pressures measured at height h_1 and h_2 [kPa]
p_{in}	Pressure inside the VD measured at the top right corner [kPa]
p_{out}	Pressure outside the VD measured at the back side of the riser at the distribution holes level [kPa]
$\bar{p}$	Average pressure [kPa]
T	Plate thickness [mm]
L_h	Hole pitch [mm]
u_0	Fluidization velocity [m/s]
U_g	Superficial gas velocity used in modelling [m/s]
u_{VD}, u'_{VD}	Fluidization velocity inside the VD based on two calculation methods [m/s]
v	Orifice velocity [m/s]
V_{ba}	Bottom air flow from the main riser to the VD [m_n^3/h]
V_{CO_2}	CO_2 flowrate [m_n^3/h]
V_{pa}, V_{air}	Primary air flowrate [m_n^3/h]
V_{sv}	Simulated volatiles flowrate [m_n^3/h]
$V_{orifice}$	Orifice gas flow [m_n^3/h]
$x_i(n)$	Time series of pressure signals [kPa]
ρ_{gas}	Density of gas (air) [kg/m^3]

AD	Air distributor
AD198	Air distributor with 198 holes
AD1660	Air distributor with 1660 holes
AR	Air reactor
BECCS	Bioenergy carbon capture and storage
Bio-CLC	Chemical looping combustion of biomass
CFD	Computational fluid dynamics
CLC	Chemical looping combustion
CLOU	Chemical looping with oxygen uncoupling
EB	Exploding bubble regime
FFT	Fast Fourier transform
FR	Fuel reactor
GHG	Greenhouse gas
HSV	High-level sampled volatiles
IPCC	Intergovernmental Panel on Climate Change
KTGF	Kinetic theory of granular flow
LSV	Low-level sampled volatiles
MB	Multiple bubble regime
PSD	Power spectral density
RSD	Relative standard deviation
SB	Single bubble regime
SD	Standard deviation
VD	Volatiles distributor

ρ_s	Density of bed materials $[\mathrm{kg/m^3}]$
σ	Standard deviation of pressure $[kPa]$
$\gamma_{\mathrm{CO_2}}$	CO_2 yield
ω_i	Conversion of the oxygen carrier at time i

8 Appendix

SEM micrographs and corresponding EDX elemental intensity maps of the cross-sections are presented below for the oxygen carrier samples: fresh, calcined, and used Eramet HM; fresh and used Guizhou; fresh and used Sibelco braunite; fresh and used UMK; and fresh and used calcium manganite.

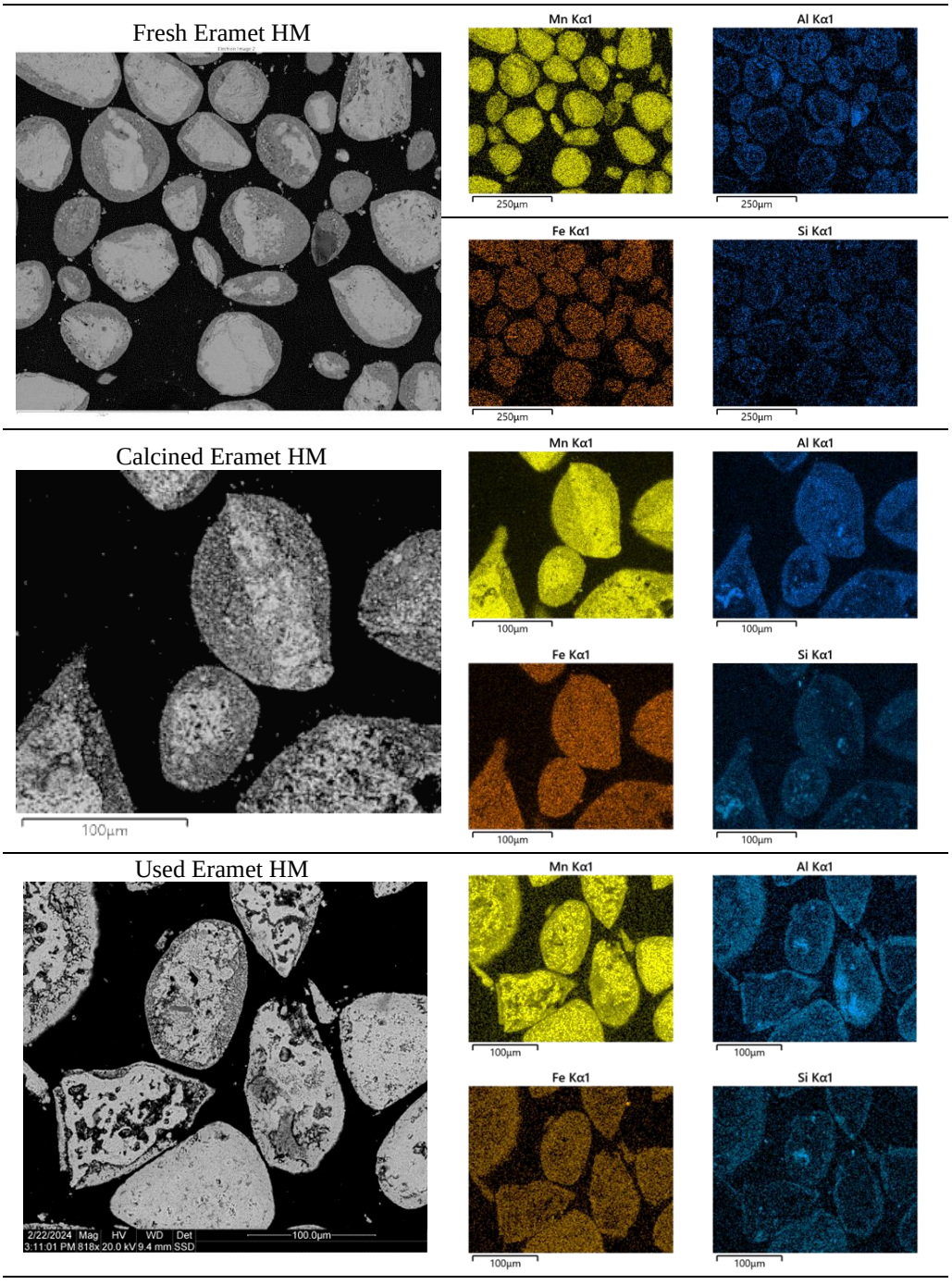

Fresh Guizhou

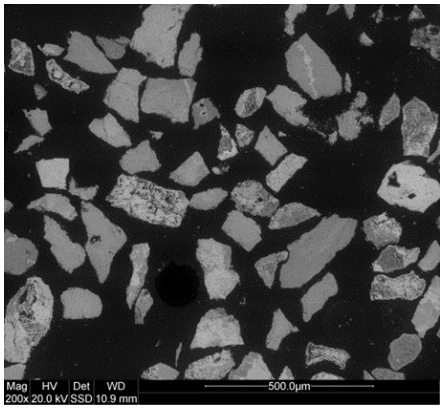

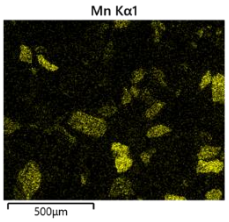

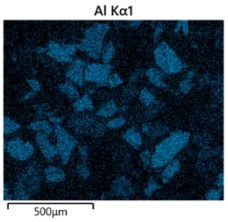

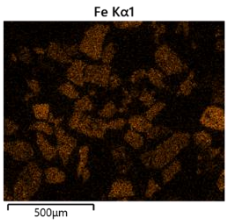

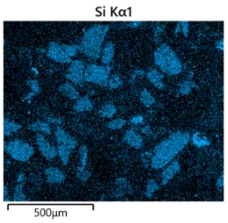

Used Guizhou

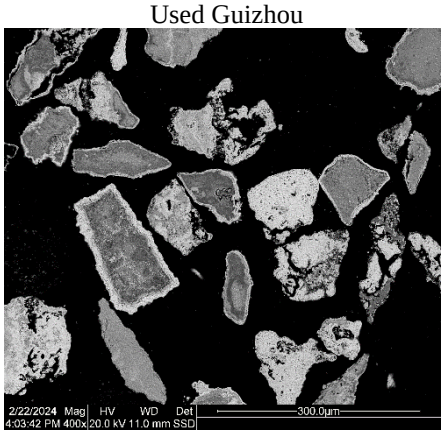

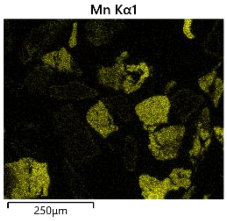

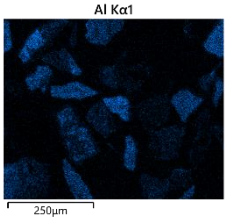

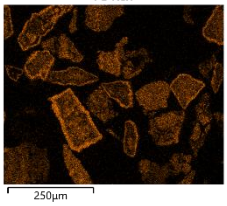

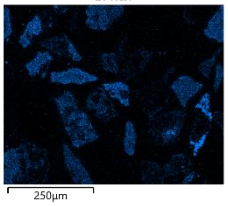

Fresh Sibelco braunite

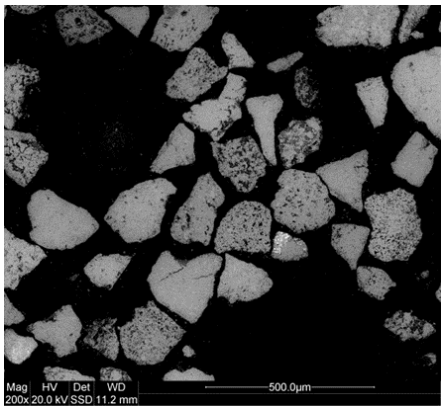

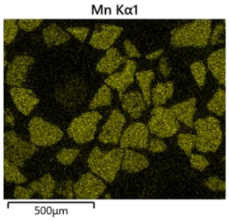

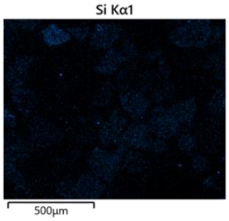

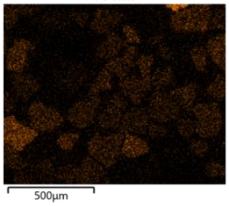

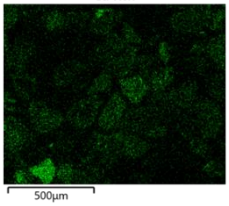

Used Sibelco braunite

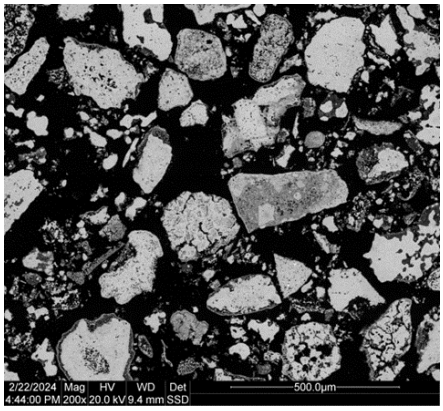

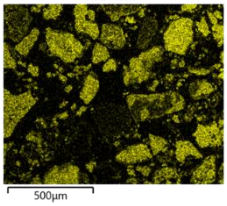

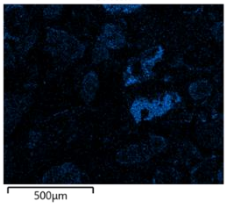

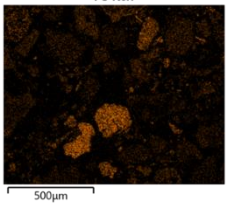

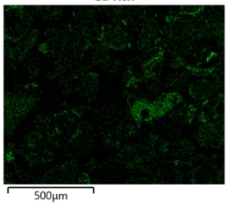

Fresh UMK

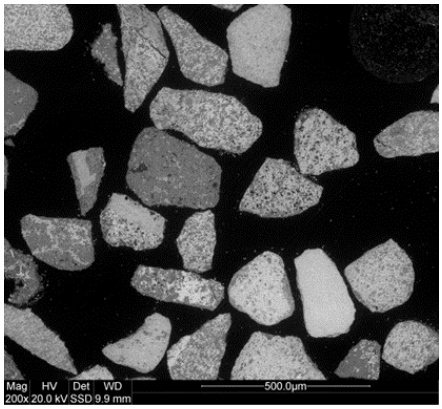

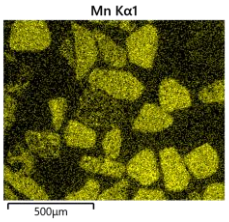

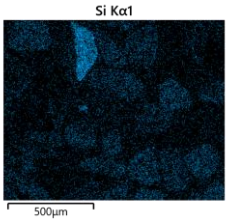

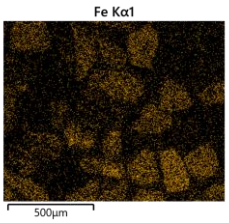

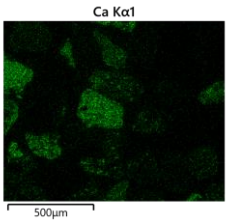

Used UMK

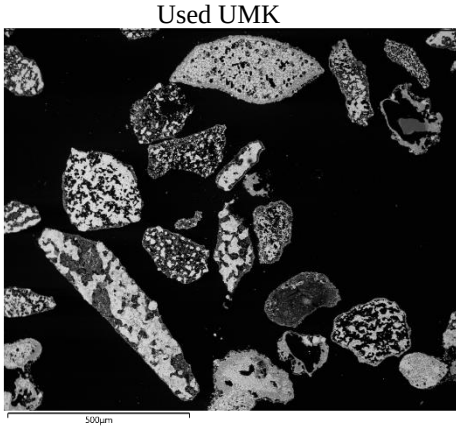

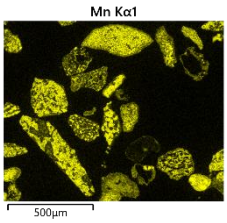

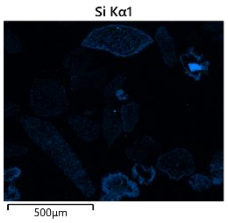

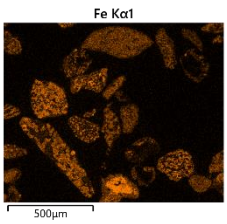

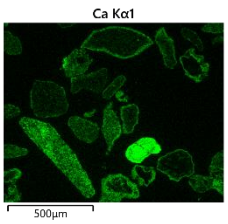

Fresh calcium manganite

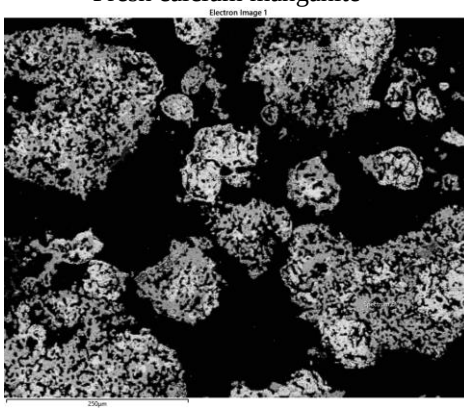

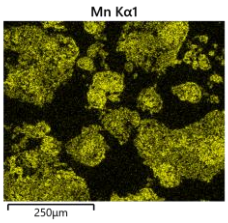

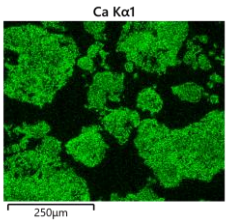

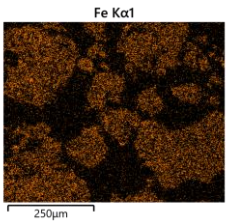

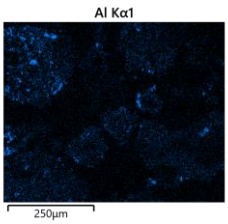

Used calcium manganite

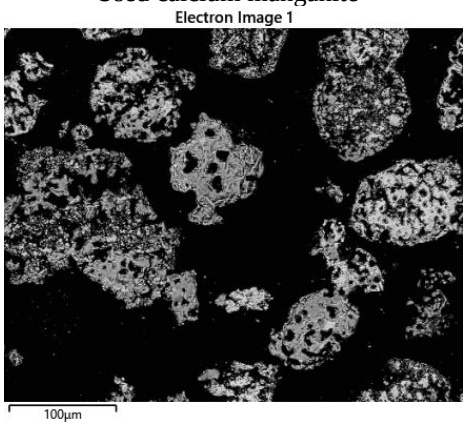

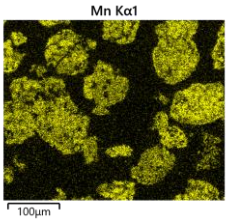

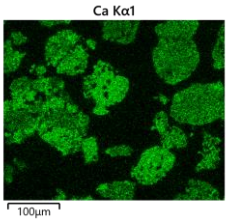

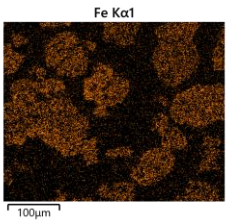

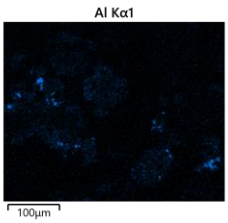

9 Reference

[1] P. Friedlingstein, M. O'Sullivan, M. W. Jones, R. M. Andrew, D. C. E. Bakker, J. Hauck, P. Landschützer, C. Le Quéré, I. T. Luijkx, G. P. Peters, W. Peters, J. Pongratz, C. Schwingshackl, S. Sitch, J. G. Canadell, P. Ciais, R. B. Jackson, S. R. Alin, P. Anthoni, L. Barbero, N. R. Bates, M. Becker, N. Bellouin, B. Decharme, L. Bopp, I. B. M. Brasika, P. Cadule, M. A. Chamberlain, N. Chandra, T. T. T. Chau, F. Chevallier, L. P. Chini, M. Cronin, X. Dou, K. Enyo, W. Evans, S. Falk, R. A. Feely, L. Feng, D. J. Ford, T. Gasser, J. Ghattas, T. Gkritzalis, G. Grassi, L. Gregor, N. Gruber, Ö. Gürses, I. Harris, M. Hefner, J. Heinke, R. A. Houghton, G. C. Hurtt, Y. Iida, T. Ilyina, A. R. Jacobson, A. Jain, T. Jarníková, A. Jersild, F. Jiang, Z. Jin, F. Joos, E. Kato, R. F. Keeling, D. Kennedy, K. Klein Goldewijk, J. Knauer, J. I. Korsbakken, A. Körtzinger, X. Lan, N. Lefèvre, H. Li, J. Liu, Z. Liu, L. Ma, G. Marland, N. Mayot, P. C. McGuire, G. A. McKinley, G. Meyer, E. J. Morgan, D. R. Munro, S. I. Nakaoka, Y. Niwa, K. M. O'Brien, A. Olsen, A. M. Omar, T. Ono, M. Paulsen, D. Pierrot, K. Pocock, B. Poulter, C. M. Powis, G. Rehder, L. Resplandy, E. Robertson, C. Rödenbeck, T. M. Rosan, J. Schwinger, R. Séférian, T. L. Smallman, S. M. Smith, R. Sospedra-Alfonso, Q. Sun, A. J. Sutton, C. Sweeney, S. Takao, P. P. Tans, H. Tian, B. Tilbrook, H. Tsujino, F. Tubiello, G. R. van der Werf, E. van Ooijen, R. Wanninkhof, M. Watanabe, C. Wimart-Rousseau, D. Yang, X. Yang, W. Yuan, X. Yue, S. Zaehle, J. Zeng, and B. Zheng, "Global Carbon Budget 2023," *Earth Syst. Sci. Data,* vol. 15, no. 12, pp. 5301-5369, 2023.

[2] V. Masson-Delmotte, P. Zhai, A. Pirani, S. L. Connors, C. Péan, S. Berger, N. Caud, Y. Chen, L. Goldfarb, M. I. Gomis, M. Huang, K. Leitzell, E. Lonnoy, J. B. R. Matthews, T. K. Maycock, T. Waterfield, O. Yelekçi, R. Yu, and B. Z. (eds.). "IPCC, 2021: Summary for Policymakers. In: Climate Change 2021: The Physical Science Basis. Contribution of Working Group I to the Sixth Assessment Report of the Intergovernmental Panel on Climate Change."

[3] S. Fuss, W. Lamb, M. Callaghan, J. Hilaire, F. Creutzig, T. Amann, T. Beringer, W. de Oliveira Garcia, J. Hartmann, T. Khanna, G. Luderer, G. Nemet, J. Rogelj, P. Smith, J. Vicente Vicente, J. Wilcox, M. Dominguez, and J. Minx, "Negative emissions—Part 2: Costs, potentials and side effects," *Environmental Research Letters,* vol. 13, pp. 063002, 06/01, 2018.

[4] M. Rydén, A. Lyngfelt, Ø. Langørgen, Y. Larring, A. Brink, S. Teir, H. Havåg, and P. Karmhagen, "Negative CO2 Emissions with Chemical-Looping Combustion of Biomass – A Nordic Energy Research Flagship Project," *Energy Procedia,* vol. 114, pp. 6074-6082, 2017/07/01/, 2017.

[5] T. Pröll, and A. Lyngfelt, "Steam Methane Reforming with Chemical-Looping Combustion: Scaling of Fluidized-Bed-Heated Reformer Tubes," *Energy & Fuels,* vol. 36, no. 17, pp. 9502-9512, 2022/09/01, 2022.

[6] A. Lyngfelt, P. Moldenhauer, M. Biermann, K. Johannsen, D. Wimmer, and M. Hanning, "Operational experiences of chemical-looping combustion with 18 manganese ores in a 300W unit," *International Journal of Greenhouse Gas Control,* vol. 127, pp. 103937, 2023/07/01/, 2023.

[7] C. Linderholm, A. Lyngfelt, A. Cuadrat, and E. Jerndal, "Chemical-looping combustion of solid fuels – Operation in a 10 kW unit with two fuels, above-bed and in-bed fuel feed and two oxygen carriers, manganese ore and ilmenite," *Fuel,* vol. 102, pp. 808-822, 2012/12/01/, 2012.

[8] H. Leion, T. Mattisson, and A. Lyngfelt, "Using chemical-looping with oxygen uncoupling (CLOU) for combustion of six different solid fuels," *Energy Procedia,* vol. 1, no. 1, pp. 447-453, 2009/02/01/, 2009.

[9] A. Abad, I. Adánez-Rubio, P. Gayán, F. García-Labiano, L. F. de Diego, and J. Adánez, "Demonstration of chemical-looping with oxygen uncoupling (CLOU) process in a 1.5kWth continuously operating unit using a Cu-based oxygen-carrier," *International Journal of Greenhouse Gas Control,* vol. 6, pp. 189-200, 2012/01/01/, 2012.

[10] T. Mattisson, A. Lyngfelt, and H. Leion, "Chemical-looping with oxygen uncoupling for combustion of solid fuels," *International Journal of Greenhouse Gas Control,* vol. 3, no. 1, pp. 11-19, 2009/01/01/, 2009.

[11] I. Gogolev, C. Linderholm, D. Gall, M. Schmitz, T. Mattisson, J. B. C. Pettersson, and A. Lyngfelt, "Chemical-looping combustion in a 100 kW unit using a mixture of synthetic and natural oxygen carriers – Operational results and fate of biomass fuel alkali," *International Journal of Greenhouse Gas Control,* vol. 88, pp. 371-382, 2019/09/01/, 2019.

[12] T. Mendiara, A. Abad, L. De Diego, F. García-Labiano, P. Gayán, and J. Adánez, "Biomass combustion in a CLC system using an iron ore as an oxygen carrier," *International Journal of Greenhouse Gas Control,* vol. 19, pp. 322-330, 2013.

[13] T. Mendiara, A. Pérez-Astray, M. T. Izquierdo, A. Abad, L. F. de Diego, F. García-Labiano, P. Gayán, and J. Adánez, "Chemical Looping Combustion of different types of biomass in a 0.5kWth unit," *Fuel*, vol. 211, pp. 868-875, 2018/01/01/, 2018.

[14] X. Niu, L. Shen, H. Gu, S. Jiang, and J. Xiao, "Characteristics of hematite and fly ash during chemical looping combustion of sewage sludge," *Chemical Engineering Journal*, vol. 268, pp. 236-244, 2015/05/15/, 2015.

[15] H. Wang, G. Liu, A. Veksha, X. Dou, A. Giannis, T. T. Lim, and G. Lisak, "Iron ore modified with alkaline earth metals for the chemical looping combustion of municipal solid waste derived syngas," *Journal of Cleaner Production*, vol. 282, pp. 124467, 2021/02/01/, 2021.

[16] A. Lyngfelt, and C. Linderholm, "Chemical-Looping Combustion of Solid Fuels – Status and Recent Progress," *Energy Procedia*, vol. 114, pp. 371-386, 2017/07/01/, 2017.

[17] C. Linderholm, M. Schmitz, P. Knutsson, M. Källén, and A. Lyngfelt, "Use of Low-Volatile Solid Fuels in a 100 kW Chemical-Looping Combustor," *Energy & Fuels*, vol. 28, no. 9, pp. 5942-5952, 2014/09/18, 2014.

[18] J. Ströhle, M. Orth, and B. Epple, "Chemical looping combustion of hard coal in a 1MW_{th} pilot plant using ilmenite as oxygen carrier," *Applied Energy*, vol. 157, pp. 288-294, 2015/11/01/, 2015.

[19] T. Berdugo Vilches, F. Lind, M. Rydén, and H. Thunman, "Experience of more than 1000h of operation with oxygen carriers and solid biomass at large scale," *Applied Energy*, vol. 190, pp. 1174-1183, 2017/03/15/, 2017.

[20] I. Petersen, and J. Werther, "Three-dimensional modeling of a circulating fluidized bed gasifier for sewage sludge," *Chemical Engineering Science*, vol. 60, no. 16, pp. 4469-4484, 2005.

[21] D. Mei, C. Linderholm, and A. Lyngfelt, "Performance of an oxy-polishing step in the 100 kWth chemical looping combustion prototype," *Chemical Engineering Journal*, vol. 409, pp. 128202, 2021/04/01/, 2021.

[22] A. Lyngfelt, and B. Leckner, "A 1000 MW_{th} boiler for chemical-looping combustion of solid fuels – Discussion of design and costs," *Applied Energy*, vol. 157, pp. 475-487, 2015/11/01/, 2015.

[23] A. Lyngfelt, D. Pallarès, C. Linderholm, F. Lind, H. Thunman, and B. Leckner, "Achieving Adequate Circulation in Chemical Looping Combustion─Design Proposal for a 200 MW_{th} Chemical Looping Combustion Circulating Fluidized Bed Boiler," *Energy & Fuels*, vol. 36, no. 17, pp. 9588-9615, 2022/09/01, 2022.

[24] J. Yan, L. Shen, S. Jiang, J. Wu, T. Shen, and T. Song, "Combustion Performance of Sewage Sludge in a Novel CLC System with a Two-Stage Fuel Reactor," *Energy & Fuels*, vol. 31, no. 11, pp. 12570-12581, 2017/11/16, 2017.

[25] D. Kunii, and O. Levenspiel, "CHAPTER 9 - Solid Movement: Mixing, Segregation, and Staging," *Fluidization Engineering (Second Edition)*, D. Kunii and O. Levenspiel, eds., pp. 211-235, Boston: Butterworth-Heinemann, 1991.

[26] L. Massimilla, and H. F. Johnstone, "Reaction kinetics in fluidized beds," *Chemical Engineering Science*, vol. 16, no. 1, pp. 105-112, 1961/12/01/, 1961.

[27] D. C. Guío-Pérez, T. Pröll, and H. Hofbauer, "Influence of ring-type internals on the solids residence time distribution in the fuel reactor of a dual circulating fluidized bed system for chemical looping combustion," *Chemical Engineering Research and Design*, vol. 92, no. 6, pp. 1107-1118, 2014/06/01/, 2014.

[28] R. Pérez-Vega, A. Abad, J. A. Bueno, F. García-Labiano, P. Gayán, L. F. de Diego, and J. Adánez, "Improving the efficiency of Chemical Looping Combustion with coal by using ring-type internals in the fuel reactor," *Fuel*, vol. 250, pp. 8-16, 2019/08/15/, 2019.

[29] A. Lyngfelt, D. Pallarés, C. Linderholm, M. Rydén, and T. Mattisson, *Fördelare av gaser i fluidiserad bädd (''Distributor of volatile gasis in the bottom part of a fluidized bed'')*, Sweden, 2014.

[30] I. Gogolev, A. H. Soleimanisalim, C. Linderholm, and A. Lyngfelt, "Commissioning, performance benchmarking, and investigation of alkali emissions in a 10 kWth solid fuel chemical looping combustion pilot," *Fuel*, vol. 287, pp. 119530, 2021/03/01/, 2021.

[31] H. Gu, L. Shen, J. Xiao, S. Zhang, and T. Song, "Chemical Looping Combustion of Biomass/Coal with Natural Iron Ore as Oxygen Carrier in a Continuous Reactor," *Energy & Fuels*, vol. 25, no. 1, pp. 446-455, 2011/01/20, 2011.

[32] T. Mendiara, A. Abad, L. F. de Diego, F. García-Labiano, P. Gayán, and J. Adánez, "Biomass combustion in a CLC system using an iron ore as an oxygen carrier," *International Journal of Greenhouse Gas Control*, vol. 19, pp. 322-330, 2013/11/01/, 2013.

[33] F. Miccio, A. Natali Murri, and E. Landi, "Synthesis and characterization of geopolymer oxygen carriers for chemical looping combustion," *Applied Energy*, vol. 194, pp. 136-147, 2017/05/15/, 2017.

[34] C. Linderholm, M. Schmitz, P. Knutsson, and A. Lyngfelt, "Chemical-looping combustion in a 100-kW unit using a mixture of ilmenite and manganese ore as oxygen carrier," *Fuel,* vol. 166, pp. 533-542, 2016/02/15/, 2016.

[35] J. Wang, and H. Zhao, "Evaluation of CaO-decorated Fe2O3/Al2O3 as an oxygen carrier for in-situ gasification chemical looping combustion of plastic wastes," *Fuel,* vol. 165, pp. 235-243, 2016/02/01/, 2016.

[36] A. Lyngfelt, A. Brink, Ø. Langørgen, T. Mattisson, M. Rydén, and C. Linderholm, "11,000 h of chemical-looping combustion operation—Where are we and where do we want to go?," *International Journal of Greenhouse Gas Control,* vol. 88, pp. 38-56, 2019/09/01/, 2019.

[37] T. Mendiara, L. F. de Diego, F. García-Labiano, P. Gayán, A. Abad, and J. Adánez, "On the use of a highly reactive iron ore in Chemical Looping Combustion of different coals," *Fuel,* vol. 126, pp. 239-249, 2014/06/15/, 2014.

[38] M. Schmitz, and C. Linderholm, "Chemical looping combustion of biomass in 10- and 100-kW pilots – Analysis of conversion and lifetime using a sintered manganese ore," *Fuel,* vol. 231, pp. 73-84, 2018/11/01/, 2018.

[39] T. Mendiara, L. F. de Diego, F. García-Labiano, P. Gayán, A. Abad, and J. Adánez, "Behaviour of a bauxite waste material as oxygen carrier in a 500Wth CLC unit with coal," *International Journal of Greenhouse Gas Control,* vol. 17, pp. 170-182, 2013/09/01/, 2013.

[40] J. Haus, K. Lyu, E.-U. Hartge, S. Heinrich, and J. Werther, "Analysis of a Two-Stage Fuel Reactor System for the Chemical-Looping Combustion of Lignite and Bituminous Coal," *Energy Technology,* vol. 4, no. 10, pp. 1263-1273, 2016.

[41] M. Schmitz, C. J. Linderholm, and A. Lyngfelt, "Chemical looping combustion of four different solid fuels using a manganese-silicon-titanium oxygen carrier," *International Journal of Greenhouse Gas Control,* vol. 70, pp. 88-96, 2018/03/01/, 2018.

[42] R. Pérez-Vega, A. Abad, F. García-Labiano, P. Gayán, L. F. de Diego, M. T. Izquierdo, and J. Adánez, "Chemical Looping Combustion of gaseous and solid fuels with manganese-iron mixed oxide as oxygen carrier," *Energy Conversion and Management,* vol. 159, pp. 221-231, 2018/03/01/, 2018.

[43] P. Moldenhauer, M. Rydén, T. Mattisson, and A. Lyngfelt, "Chemical-looping combustion and chemical-looping with oxygen uncoupling of kerosene with Mn- and Cu-based oxygen carriers in a circulating fluidized-bed 300W laboratory reactor," *Fuel Processing Technology,* vol. 104, pp. 378-389, 2012/12/01/, 2012.

[44] P. Gayán, I. Adánez-Rubio, A. Abad, L. F. de Diego, F. García-Labiano, and J. Adánez, "Development of Cu-based oxygen carriers for Chemical-Looping with Oxygen Uncoupling (CLOU) process," *Fuel,* vol. 96, pp. 226-238, 2012/06/01/, 2012.

[45] I. Adánez-Rubio, P. Gayán, A. Abad, L. F. de Diego, F. García-Labiano, and J. Adánez, "Evaluation of a Spray-Dried CuO/$MgAl_2O_4$ Oxygen Carrier for the Chemical Looping with Oxygen Uncoupling Process," *Energy & Fuels,* vol. 26, no. 5, pp. 3069-3081, 2012/05/17, 2012.

[46] M. Rydén, H. Leion, T. Mattisson, and A. Lyngfelt, "Combined oxides as oxygen-carrier material for chemical-looping with oxygen uncoupling," *Applied Energy,* vol. 113, pp. 1924-1932, 2014/01/01/, 2014.

[47] A. Lambert, C. Delquié, I. Clémeneçon, E. Comte, V. Lefebvre, J. Rousseau, and B. Durand, "Synthesis and characterization of bimetallic Fe/Mn oxides for chemical looping combustion," *Energy Procedia,* vol. 1, no. 1, pp. 375-381, 2009/02/01/, 2009.

[48] D. Jing, E. Hermans, H. Leion, M. Rydèn, T. Mattisson, J. Noyen, and A. Lyngfelt, *Manganese-silica combined oxides as oxygen carrier for chemical-looping combustion*, 2012.

[49] A. Shulman, E. Cleverstam, T. Mattisson, and A. Lyngfelt, "Manganese/iron, manganese/nickel, and manganese/silicon oxides used in chemical-looping with oxygen uncoupling (CLOU) for combustion of methane," *Energy & Fuels,* vol. 23, no. 10, pp. 5269-5275, 2009.

[50] G. Azimi, H. Leion, T. Mattisson, and A. Lyngfelt, "Chemical-looping with oxygen uncoupling using combined Mn-Fe oxides, testing in batch fluidized bed," *Energy Procedia,* vol. 4, pp. 370-377, 2011/01/01/, 2011.

[51] G. Azimi, H. Leion, M. Rydén, T. Mattisson, and A. Lyngfelt, "Investigation of Different Mn–Fe Oxides as Oxygen Carrier for Chemical-Looping with Oxygen Uncoupling (CLOU)," *Energy & Fuels,* vol. 27, no. 1, pp. 367-377, 2013/01/17, 2013.

[52] G. Azimi, M. Rydén, H. Leion, T. Mattisson, and A. Lyngfelt, "(MnzFe1—z)yOx combined oxides as oxygen carrier for chemical-looping with oxygen uncoupling," *AIChE Journal,* vol. 59, no. 2, pp. 582-588, 2013.

[53] M. Arjmand, V. Frick, M. Rydén, H. Leion, T. Mattisson, and A. Lyngfelt, "Screening of Combined Mn-Fe-Si Oxygen Carriers for Chemical Looping with Oxygen Uncoupling (CLOU)," *Energy & Fuels,* vol. 29, no. 3, pp. 1868-1880, 2015/03/19, 2015.

[54] T. Mattisson, D. Jing, A. Lyngfelt, and M. Rydén, "Experimental investigation of binary and ternary combined manganese oxides for chemical-looping with oxygen uncoupling (CLOU)," *Fuel,* vol. 164, pp. 228-236, 2016/01/15/, 2016.
[55] J. V. Crum, B. J. Riley, and J. D. Vienna, "Binary Phase Diagram of the Manganese Oxide–Iron Oxide System," *Journal of the American Ceramic Society,* vol. 92, no. 10, pp. 2378-2384, 2009.
[56] Q. Imtiaz, D. Hosseini, and C. R. Müller, "Review of Oxygen Carriers for Chemical Looping with Oxygen Uncoupling (CLOU): Thermodynamics, Material Development, and Synthesis," *Energy Technology,* vol. 1, no. 11, pp. 633-647, 2013.
[57] M. Rydén, A. Lyngfelt, and T. Mattisson, "Combined manganese/iron oxides as oxygen carrier for chemical looping combustion with oxygen uncoupling (CLOU) in a circulating fluidized bed reactor system," *Energy Procedia,* vol. 4, pp. 341-348, 2011/01/01/, 2011.
[58] A. Muan, "Phase equilibria in the system manganese oxide-SiO 2 in air," *American Journal of Science,* vol. 257, no. 4, pp. 297-315, 1959.
[59] I. Staničić, J. Brorsson, A. Hellman, M. Rydén, and T. Mattisson, "Thermodynamic analysis on the fate of ash elements in chemical looping combustion of solid fuels – Manganese-Based oxygen carriers," *Fuel,* vol. 369, pp. 131676, 2024/08/01/, 2024.
[60] M. Arjmand, A. Hedayati, A.-M. Azad, H. Leion, M. Rydén, and T. Mattisson, "CaxLa1–xMn1–yMyO3−δ (M = Mg, Ti, Fe, or Cu) as Oxygen Carriers for Chemical-Looping with Oxygen Uncoupling (CLOU)," *Energy & Fuels,* vol. 27, no. 8, pp. 4097-4107, 2013/08/15, 2013.
[61] M. Arjmand, M. Keller, H. Leion, T. Mattisson, and A. Lyngfelt, "Oxygen Release and Oxidation Rates of $MgAl_2O_4$-Supported CuO Oxygen Carrier for Chemical-Looping Combustion with Oxygen Uncoupling (CLOU)," *Energy & Fuels,* vol. 26, no. 11, pp. 6528-6539, 2012/11/15, 2012.
[62] M. Källén, M. Rydén, C. Dueso, T. Mattisson, and A. Lyngfelt, "CaMn0.9Mg0.1O3-δ as Oxygen Carrier in a Gas-Fired 10 kWthChemical-Looping Combustion Unit," *Industrial & Engineering Chemistry Research,* vol. 52, no. 21, pp. 6923-6932, 2013/05/29, 2013.
[63] M. Rydén, A. Lyngfelt, and T. Mattisson, "CaMn0.875Ti0.125O3 as oxygen carrier for chemical-looping combustion with oxygen uncoupling (CLOU)—Experiments in a continuously operating fluidized-bed reactor system," *International Journal of Greenhouse Gas Control,* vol. 5, no. 2, pp. 356-366, 2011/03/01/, 2011.
[64] T. Karlsson, X. Liu, D. Pallarès, and F. Johnsson, "Solids circulation in circulating fluidized beds with low riser aspect ratio and varying total solids inventory," *Powder Technology,* vol. 316, pp. 670-676, 2017.
[65] A. Svensson, F. Johnsson, and B. Leckner, "Fluidization regimes in non-slugging fluidized beds: the influence of pressure drop across the air distributor," *Powder Technology,* vol. 86, no. 3, pp. 299-312, 1996/03/01/, 1996.
[66] X. Li, A. Lyngfelt, and T. Mattisson, "An experimental study of a volatiles distributor for solid fuels chemical-looping combustion process," *Fuel Processing Technology,* vol. 220, pp. 106898, 2021/09/01/, 2021.
[67] X. Li, A. Lyngfelt, D. Pallarès, C. Linderholm, and T. Mattisson, "Investigation on the Performance of Volatile Distributors with Different Configurations under Different Fluidization Regimes," *Energy & Fuels,* 2022/01/28, 2022.
[68] X. Li, A. Lyngfelt, C. Linderholm, B. Leckner, and T. Mattisson, "Performance of a volatiles distributor equipped with internal baffles under different fluidization regimes," *Powder Technology,* vol. 409, pp. 117807, 2022/09/01/, 2022.
[69] D. Gidaspow, *Multiphase Flow and Fluidization*, 1994.
[70] A. Sarkar, F. E. Milioli, S. Ozarkar, T. Li, X. Sun, and S. Sundaresan, "Filtered sub-grid constitutive models for fluidized gas-particle flows constructed from 3-D simulations," *Chemical Engineering Science,* vol. 152, pp. 443-456, 2016/10/02/, 2016.
[71] H. Luo, B. Lu, J. Zhang, H. Wu, and W. Wang, "A grid-independent EMMS/bubbling drag model for bubbling and turbulent fluidization," *Chemical Engineering Journal,* vol. 326, pp. 47-57, 2017/10/15/, 2017.
[72] D. Gidaspow, R. Bezburuah, and J. Ding, *Hydrodynamics of circulating fluidized beds: kinetic theory approach*, Illinois Inst. of Tech., Chicago, IL (United States). Dept. of Chemical …, 1991.
[73] S. Benzarti, H. Mhiri, and H. Bournot, "Numerical simulation of baffled circulating fluidized bed with Geldart B particles," *Powder Technology,* vol. 380, pp. 629-637, 2021.
[74] K. Ding, Q. Xiong, Z. Zhong, D. Zhong, and Y. Zhang, "CFD simulation of combustible solid waste pyrolysis in a fluidized bed reactor," *Powder Technology,* vol. 362, pp. 177-187, 2020/02/15/, 2020.
[75] Y. Zhang, Z. Chao, and H. A. Jakobsen, "Modelling and simulation of chemical looping combustion process in a double loop circulating fluidized bed reactor," *Chemical Engineering Journal,* vol. 320, pp. 271-282, 2017/07/15/, 2017.

[76] B. Lu, N. Zhang, W. Wang, J. Li, J. H. Chiu, and S. G. Kang, "3-D full-loop simulation of an industrial-scale circulating fluidized-bed boiler," *AIChE Journal,* vol. 59, no. 4, pp. 1108-1117, 2013.
[77] H. Luo, W. Lin, W. Song, S. Li, K. Dam-Johansen, and H. Wu, "Three dimensional full-loop CFD simulation of hydrodynamics in a pilot-scale dual fluidized bed system for biomass gasification," *Fuel Processing Technology,* vol. 195, pp. 106146, 2019.
[78] T. Li, J.-F. Dietiker, and L. Shadle, "Comparison of full-loop and riser-only simulations for a pilot-scale circulating fluidized bed riser," *Chemical Engineering Science,* vol. 120, pp. 10-21, 2014/12/16/, 2014.
[79] Q. Tu, H. Wang, and R. Ocone, "Application of three-dimensional full-loop CFD simulation in circulating fluidized bed combustion reactors – A review," *Powder Technology,* vol. 399, pp. 117181, 2022/02/01/, 2022.
[80] T. Djerf, "Solids Flow in Large-Scale Circulating Fluidized Bed Furnaces," Chalmers University of Technology, Gothenburg, Sweden, 2021.
[81] J. Xiang, Q. Li, Z. Tan, and Y. Zhang, "Characterization of the flow in a gas-solid bubbling fluidized bed by pressure fluctuation," *Chemical Engineering Science,* vol. 174, pp. 93-103, 2017/12/31/, 2017.
[82] F. Johnsson, R. C. Zijerveld, J. C. Schouten, C. M. van den Bleek, and B. Leckner, "Characterization of fluidization regimes by time-series analysis of pressure fluctuations," *International Journal of Multiphase Flow,* vol. 26, no. 4, pp. 663-715, 2000/04/01/, 2000.
[83] D. Kunii, and O. Levenspiel, "CHAPTER 4 - The Dense Bed: Distributors, Gas Jets, and Pumping Power," *Fluidization Engineering (Second Edition),* D. Kunii and O. Levenspiel, eds., pp. 95-113, Boston: Butterworth-Heinemann, 1991.
[84] X. Li, R. Faust, V. Purnomo, D. Mei, C. Linderholm, A. Lyngfelt, and T. Mattisson, "Performance of a perovskite-structured calcium manganite oxygen carrier produced from natural ores in a batch reactor and in operation of a chemical-looping combustion reactor system," *Submitted to Chemical Engineering Journal,* 2024.
[85] P. Moldenhauer, P. Hallberg, M. Biermann, F. Snijkers, K. Albertsen, T. Mattisson, and A. Lyngfelt, "Oxygen-Carrier Development of Calcium Manganite–Based Materials with Perovskite Structure for Chemical-Looping Combustion of Methane," *Energy Technology,* vol. 8, no. 6, pp. 2000069, 2020.
[86] E. Bakken, T. Norby, and S. Stølen, "Nonstoichiometry and reductive decomposition of CaMnO3− δ," *Solid State Ionics,* vol. 176, no. 1-2, pp. 217-223, 2005.
[87] L. Rørmark, K. Wiik, S. Stølen, and T. Grande, "Oxygen stoichiometry and structural properties of La1 − xAxMnO3 ± δ (A = Ca or Sr and $0 \leq x \leq 1$)," *Journal of Materials Chemistry,* vol. 12, no. 4, pp. 1058-1067, 2002.